ROCK PHYSICS FOR HYDROCARBON RECOVERY MONITORING

A DISSERTATION
SUBMITTED TO THE DEPARTMENT OF GEOPHYSICS
AND THE COMMITTEE ON GRADUATE STUDIES
OF STANFORD UNIVERSITY
IN PARTIAL FULFILLMENT OF THE REQUIREMENTS
FOR THE DEGREE OF
DOCTOR OF PHILOSOPHY

By
James Lee Packwood
December, 1997

Abstract

Monitoring hydrocarbon resources through repeated seismic surveys (4D seismic) is a potentially powerful technique. It often works because variations in fluid saturation, pore pressure, and temperature during oil/gas recovery change the stiffness of the reservoir rock and, in turn, the compressional and shear-wave velocities. These temporal changes can be observed through periodic seismic surveys. In principle, they allow one to detect fluid migration, permeability barriers, and bypassed hydrocarbons, thus leading to improved recovery. Rock physics quantitatively links changes in saturation, temperature, and pressure to velocity changes.

In this thesis, I provide a rock physics methodology for interpreting 4D seismic for fluid location and pressure changes. First, I develop two models for possible fluid distribution in rock, uniform and patchy. By applying these models to reservoir simulation data, I show that fluid distribution can significantly affect the velocity and thus seismic reservoir signatures. Specifically, I find that changes in the seismic signature that accompany small changes in gas saturation in a developing gas cone can often be masked by noise if saturation is patchy. On the other hand, these changes are readily observable if saturation is uniform. Using well log data, I show that patchy saturation exists at the logging frequency scale, and, therefore, is likely at the seismic scale. Thus it is important to consider the distinct saturation patterns introduced here.

Other parameters that can affect the detectability of recovery-associated changes in a reservoir are rock frame stiffness and pore pressure. To explore the effect of frame stiffness, I use reservoir simulation data together with three different realistic models that link rock stiffness to porosity. I find that increasing rock frame stiffness reduces the seismic visibility of a developing gas cone. To illustrate the effect of pore pressure, I model the velocity and

reflectivity at the top of an uncemented gas sand at two pore pressure values. Synthetic CDP gathers show that an increase in the velocity associated with pore pressure reduction results in reduced reflectivity at the top and base and velocity pull-up at the base of the sand.

Acknowledgements

As my time at Stanford comes to a close, I wonder how I can possibly thank everyone who has played a part in encouraging me along the way. I genuinely thank Amos Nur for inviting me to be a part of the SRB project. Amos' ability to look down the road and see what's ahead is quite inspiring. I attribute the theme of this thesis to his insight. When I was trying to find my way around during my first year, we had several discussions about what my research topic would be, and I learned to trust his instincts.

Joel Walls first introduced me to Amos and to the work in the Rock Physics lab back in 1991. When I told Joel I was considering leaving my industry job and going back to school, he made a point of bringing me to Stanford to meet Amos. I had not considered geophysics as a potential field for graduate study, but what I saw here made the decision to change disciplines an easy one. Thanks, Joel, for all your encouragement and support over the past 7 years. (For the record, 2 of those were pre-Stanford years.)

I would also like to thank Gary Mavko for his excellent teaching, both in and out of the classroom. I learned as much as a TA in the Rock Physics course as I did when I took it my first quarter at Stanford. Gary gave me one of the first ideas for a specific research topic, and his input along the way made it a truly fulfilling experience. I also worked closely with Jack Dvorkin on several projects. Our numerous discussions guided me as I made progress on parts of my thesis, whether I was editing a paper or making final plans for wrapping up my thesis. Gary and Jack have provided invaluable support to me.

To Margaret Muir, I convey a million thanks. Our chats during my years here have been quite enjoyable. Thanks for keeping the SRB running so smoothly. Many of us have no idea what you have to do to make sure we have everything we need. Thanks so much, especially for your help these past couple of months.

There are several fellow students whom I must also remember here. Enjoying a guru-like status among his fellow students, Tapan Mukerji has been a tremendous resource that I enjoyed while being here. Our many encounters enlightened my journey, as Tapan could often point me in the right direction when I needed an answer. I also thank Dawn Burgess for her friendship. I really admired her interest in a seemingly endless list of extracurricular activities, which proved that life outside of Stanford could be quite productive. (Those practice wedding cakes sure were tasty!) TAing the Rock Physics course with her was really fun. Among those with whom I shared an office, Frank Liu, Doron Galmudi, and Amy Day-Lewis stand out for various reasons. I learned how valuable friendships are when you work in tight quarters. Doron and I often enjoyed spontaneous discussions about science, geopolitical issues, religion, and at the end, babies. Amy and her husband Fred provided opportunities for me and my wife to socialize off campus. Thanks for the late night raccoon adventure! One thing I truly enjoyed about my stay at Stanford was the opportunity to interact with people from several different cultures. This often made for lively discussion of international events, movies, and life on the Farm over lunch and coffee. I wouldn't trade this experience for anything. Thanks Thomas, Christine, Yizhaq, Tony, and Carl. I should also mention my adventures with Ran Bachrach trying to solve some annoying computer problem. You're on your own now!

My family has been a very important part of my life, and I would like to acknowledge their part in my being here. I dedicate this thesis to my parents, Fred and Allecia Packwood. Although my father is not living, I know he would have been proud to see me complete my Ph.D. I am thankful for parents who let me set my own goals and pursue them as I saw fit. Their loving support helped make me who I am. Thanks, Mom! I also thank my brothers, my sister, and my grandparents for their support and encouragement through the years. I would not be who I am today without you all. The many phone calls to you have been so important to me while I've been at Stanford.

Finally, I would like to thank my wife Rochelle for her loving support and encouragement for the past 4 years. Thanks for all the fun adventures, for helping me to discover more about who I am than I had known before. We have had a wild ride this year, and I thank you for bearing with me. Thanks for saying yes when I asked you to marry me last February. I couldn't have made it without you!

Contents

List of Figures

List of Tables

Chapter 1

Introduction

1.1 Defining the Problem

The demand for oil and gas will undoubtedly continue well into the next century. Improving recovery efficiency in existing fields is an important source of hydrocarbons: several estimates project that more than half of future US oil reserves will come from improved recovery (Fisher, 1991). Often, less than 25% of the oil in place is recovered through primary production. The amount of recoverable oil is much higher than this, and secondary or tertiary processes, such as water or miscible gas flooding, are necessary to produce this additional oil. These processes can bypass significant volumes of oil, and repeated seismic surveys provide a means to detect pore fluid and pore pressure changes during recovery processes. I believe that repeated seismic surveys will become an increasingly important reservoir management tool. The concept of using seismic surveys to monitor hydrocarbon recovery processes was first proposed by Nur (1982). Since that time, people have demonstrated that seismic surveys can be used successfully to monitor and manage recovery processes, such as steam injection and CO_2 flooding. Rock physics provides the tools necessary to predict and interpret changes in seismic data resulting from recovery processes. In a recent article, Pennington (1997) says there is a need to make the application of rock physics principles clear. This thesis attempts to do this by exploring some rock physics aspects that have a bearing on recovery monitoring and presenting them in a way that makes the procedure clear.

1.2 Review of Published Work on Monitoring

The concept of monitoring subsurface fluid flow using seismic reflection surveys was introduced in by Barr (1973). Barr proposed the use of periodic reflection surveys to monitor the injection of waste materials in disposal wells. He indicated that the change in acoustic properties in the formation could be used to monitor the movement and position of injected waste materials. Barr based this proposal on changes in reflection coefficient that would arise as the result of fluid substitution.

In 1982, Nur proposed that seismic surveys could be used to monitor enhanced oil recovery processes, specifically during steam injection to recover heavy oil. Nur proposed the deployment of seismic source and receiver arrays in the region of enhanced recovery to detect travel times and amplitudes and their temporal and spatial changes. Nur suggested that it is possible to determine a distribution of velocities and attenuation (Q^{-1}) within the reservoir. From laboratory measurements of the seismic response of reservoir rock samples, one could then determine the distribution of steam in the reservoir from the distribution of velocities and Q^{-1}.

Tosaya et al. (1984) presented the results of laboratory measurement of V_P and V_S in heavy oil sand samples. They measured V_P and V_S and transmission amplitudes as a function of temperature and pressure for various states of saturation. Results of this study demonstrated the feasibility of detecting thermal EOR fronts and mapping the distribution of heated oil in heavy oil reservoirs.

A field-based case study, reported by Greaves et al. (1984), involved monitoring an in-situ combustion project. They collected a 3-D baseline survey prior to initiating combustion and two monitoring surveys. They reported seismically visible changes in the reservoir, mainly as a result of increasing gas saturation. They investigated amplitude and other wave form changes. Greaves and Fulp (1987) later presented more results from this project. Their technique of investigation was to make stacked sections from each survey and then to calculate travel time and amplitude difference maps to compare the monitoring surveys to the base line survey. They were able to monitor the shape, orientation and volume of the burn zone, and they generated maps of estimated burn thickness from the seismic data. They confirmed their results with post-burn coring and with temperature monitor wells.

The next field-scale case study was reported by Pullin et al. (1987). This study involved collecting two 3-D seismic surveys before and after a steam flood of a tar sand. They compared the time delay and amplitude maps between the two stacked surveys, and they qualitatively mapped the location of the steamed zone. The observed time delays and attenuation through the steamed zone compared favorably with rock physics laboratory studies.

Dunlop et al. (1988) reported the use of seismic surveys to monitor a waterflood. They collected two surveys consisting of a single line of seismic data in a region above three active wells. They were able to detect changing saturations in a 15 foot thick sandstone reservoir at a depth of 1850 feet using amplitude variations between seismic surveys.

Another field example using steam was reported by Eastwood et al. (1994). This reservoir is a tar sand that is produced by means of cyclic steam injection. They collected two 3-D surveys, the first during a production cycle and the second almost two years later during an injection cycle. An analysis of delay time, amplitude changes, and frequency attenuation were used to determine areal and volumetric extent of the steamed zone. The steamed zone as determined with the seismic surveys agreed with the areal and volumetric conformance predicted by reservoir simulation, but the spatial distributions of the anomalies were different. An observation well was used to verify the results of the seismic surveys. In this case, the seismic data could be used to improve reservoir simulation.

1.3 Description of Chapters

The chapters in this thesis present various applications of rock physics principals to study hydrocarbon recovery monitoring.

Chapter 2 explores the role of fluid distribution on the seismic wave velocities. I worked with Gary Mavko to develop conceptual models for fluid distribution. The uniform or effective fluid distribution model is the one most often used by geophysicists to solve the fluid substitution problem. Along with this model, we propose a patchy model that results in higher compressional wave velocities than the uniform fluid model. We give an example of using the models to investigate the range of velocity changes during a steam flood of a heavy oil reservoir.

Chapter 3 began as a study for Norsk Hydro on the feasibility of monitoring oil production in the Troll field. I worked on the initial study with Jack Dvorkin and others to model velocity and impedance in the reservoir during simulated production. I extended this initial study to include both uniform and patchy fluid distribution, and I show the simulated seismic responses.

In Chapter 4, I explore the effects of the rock frame stiffness, pore fluids, and pore pressure on seismic responses. I show how these parameters are important in modeling the rock velocities in Chapter 2, and here I extend the investigation by modeling the seismic response for various rocks, fluids, and pressures.

Chapter 5 investigates the possibility of detecting patchy saturation on well logs. This chapter represents a collaborative effort with Jack Dvorkin, Dan Moos, and Amos Nur. Based on a well log from a Gulf Coast gas well, we invert the saturated log velocities in order to get the dry rock properties. We use Poisson's ratio to discriminate between uniform and patchy fluid distribution.

I present a summary of this thesis in Chapter 6. I discuss the rock physics principles used in this thesis and the data needs for monitoring projects. I include a discussion of using attenuation for recovery monitoring.

1.4 References

Barr, F.J., Jr, 1973, Feasibility study of a seismic reflection monitoring system for underground waste-material injection site: Underground waste management and artificial recharge, **1**, 207-218.

Dunlop, K.N.B., King, G.A., and Breitenbach, E.A., 1988, Monitoring of oil/water fronts by direct measurement: SPE Paper No. 18271, Proceedings - SPE Annual Technical Conference and Exhibition, Epsilon, **63**, 91–99.

Eastwood, J. Lebel, L. Dilay, A. and Blakeslee, S., 1994, Seismic monitoring of steam-based recovery of bitumen: The Leading Edge, **13**, 242-251.

Fisher, W.L., 1991, Future supply potential of US oil and natural gas: The Leading Edge, **10**, No. 12, 15–21.

Greaves, R.J., Fulp, T.J., and Head, P.L., 1984, 3D seismic monitoring of enhanced oil recovery project: Am. Assoc. of Petr. Geol. Bull.; **68**, 481.

Greaves, R.J., and Fulp, T.J., 1987, Three-dimensional seismic monitoring of an enhanced oil recovery process: Geophysics, **52**, 1175-1187.

Nur, A., 1982, Seismic imaging in enhanced recovery: Proceedings - Joint SPE/DOE Symposium on Enhanced Oil Recovery, **3**, 99–109.

Pennington, W., 1997, Seismic petrophysics: An applied science for reservoir geophysics: The Leading Edge, **16**, 241–244.

Pullin, N.E., Jackson, R.K., Matthews, L.W., Thorburn, R.F., Hirsche, W.K., and den Boer, L.D., 1987, 3-D seismic imaging of heated zones at an Athabasca tar sands thermal pilot: SEG Annual Meeting Expanded Technical Program Abstracts with Biographies, **57**, 391–394.

Tosaya, C.A., Nur, A.M., and Da Prat, G., 1984, Monitoring of thermal EOR fronts by seismic methods: SPE Paper No. 12744 presented at SPE California Regional Meeting, Long Beach, CA.

Chapter 2

Pore Fluid Distribution and Seismic Velocities

2.1 Introduction

Seismic monitoring is the process of using repeated seismic surveys (4D seismic) to observe changes in a hydrocarbon reservoir during recovery processes. Since the early 1980's, both surface and cross-well seismic surveys have been used to monitor processes such as steam floods, carbon dioxide floods, and movement of the water-hydrocarbon contact. The rock physics aspect of monitoring is both to predict changes in the seismic signature of a reservoir during production and to interpret the observed changes. A critical part of quantifying the seismic signatures associated with the injection and withdrawal of fluids in a hydrocarbon reservoir is understanding how the fluids are distributed in the pore space of the rock. Typical reservoir simulators predict spatial distributions of temperature, pressure, and fluid saturations, but the values are averages over large simulator cells - often tens of meters in size. Seismic velocity and impedance can depend strongly on the fluid distribution at scales much finer than a seismic wavelength and much finer than described by the simulator.

In this chapter, I explore the range of velocity signatures that can result from variations in fluid distribution at scales smaller than a seismic wavelength or simulator cell. I investigate three models of fluid distribution: 1) Uniform effective fluid, 2) Fluid in patches, and

3) Laminated fluid. The effective fluid model assumes that each of the phases is uniformly distributed at the finest scale in the pore space. The patchy model assumes that distinct fluid phases (or mixtures of fluids) exist in isolated patches in the reservoir - the saturations are spatially heterogeneous. The lamination model assumes that the patches exist in distinct layers in the reservoir, as might result from fingering or layered geology.

I find that the patchy multi-phase fluid distributions have consistently higher compressional wave velocity and impedance than the uniform distribution of fluids at the same partial liquid saturations ($0.0 < S_l < 1.0$).

I also investigate the effect of oil distillation during steam flooding of a heavy oil reservoir. The presence of different oil phases in the reservoir may give significantly different seismic responses. The effect is minimal if the fluids are distributed uniformly, but the possibility of different oil phases must be considered if the fluids are distributed in patches.

2.2 Heterogeneous Saturation

The concept of heterogeneous saturations is not a new one. Several authors report observations of heterogeneous fluid distribution using methods such as visual observations and CT scans. Domenico (1976) suggested that such heterogeneities could result in differences in wave velocities. There is some evidence that heterogeneities in fluid saturation cause *P*-wave velocities measured in the laboratory to be higher than expected. In this section, I review some papers which document the existence of heterogeneous saturation, and I offer a brief explanation of how such saturations might form in nature.

2.2.1 Experimental Observations

There is ample experimental evidence of heterogeneous saturation. Chatenever and Calhoun (1952) report the results of flow experiments designed to image flow patterns in porous media. Their experimental setup included a single layer of uniform spheres packed between transparent plates. Using both water-wet glass spheres and oil-wet lucite spheres between the plates, they flowed oil (density = 0.9 g/cm^3, viscosity = 14 cp) and water in varying percentages through the media. They also altered the injection rates to see how that affected fluid distribution on the pore scale. They observed two flow regimes: channel

flow at lower injection rates and slug flow at higher injection rates. In channel flow, both oil and water were transported in interconnecting channels which varied in size from one to many grain diameters. The tortuous channels were bounded by liquid-liquid interfaces. During steady flow conditions, the geometries and positions of the channels remained fixed. However, changes in saturation altered the geometries of the channels. For example, the diameters of the oil channels grew when the relative volume of injected oil (and the oil saturation) increased. At the higher flow rates, slug flow became evident. In this flow regime, some of the flow through the media took place in isolated globules. In the water-wet glass system, the water phase remained continuous and the oil phased formed slugs. The opposite was observed in the oil-wet lucite apparatus. These flow regimes were observed during simultaneous injection of oil and water.

Different phenomena were observed while flooding the system with a single fluid displacing the other. Injected water fingered through the oil-bearing glass sphere pack, bypassing significant volumes of oil. In contrast, oil injected into water-saturated glass spheres did not develop fingers, and the displacement of water was more uniform. The authors observed similar patterns in flooding the oil-filled Lucite flow cell with water and the water-filled Lucite cell with oil, so wettability did not appear to be a factor in the displacement mechanism. In these flooding experiments, fluid flow took place in continuous phases with no slug flow.

In most of these cases, even with a nearly ideal system of uniform grains and pores, it would be difficult to classify the fluid distribution as uniform. The possible exception to this is the piston-like displacement of water by injected oil. Even more revealing than the flow regime was the residual saturation geometries observed. Chatenever and Calhoun observed residual oil in patches as large as several grain diameters after injecting water into an oil-bearing packing of glass spheres. Some of these patches extended over the length of the flow cell. In some cases, the by-passed oil occupied a large percentage of the pore space. In contrast, the residual water from an oil flood appeared as pendular rings between spheres and between the horizontal plate and spheres.

In another set of experiments designed to visualize flow processes, van Meurs (1957) reported the development of viscous fingers when injecting water into a relatively homogeneous, oil-saturated medium. He injected water into glass bead packs that were saturated

with oil. When the oil viscosity and water viscosity were equal, water seemed to displace the oil uniformly. However, when the oil viscosity was 80 times larger than the water viscosity, the injected water formed fingers as it displaced the oil. The same results were observed under radial flow conditions. In this experiment, water was injected in the center of a square apparatus, and oil was produced from the four corners. This simulated a five-spot well pattern, common in secondary oil recovery projects. Again, when the viscosities were equal, the water displaced the oil uniformly in a radial pattern around the injection well. With a viscosity ratio of 80, van Meurs again observed viscous fingers. This time, the fingers aligned themselves along stream lines between the injection well and the production wells.

One additional experiment reported by van Meurs involved solution gas drive, a mechanism where the release of dissolved gas displaces oil. The dissolved gas is released as a result of decreasing pore pressure. In this case, van Meurs started with a glass bead pack in a tube, and then he filled the tube with a live oil (i.e. an oil containing dissolved gas). By lowering the pressure at both ends of the tube below the bubble point of the oil, gas was liberated from the oil, displacing oil out the ends of the tube. After production began, fluids were distributed non-uniformly, with free gas near the outlets and no free gas in the center of the tube. Small gas fingers formed in the direction opposite flow from the tube. Free gas did not appear throughout the tube until 17 percent of the oil was produced. This same experiment was repeated while vibrating the tube at the beginning. Initially, isolated gas bubbles appeared throughout the tube, and gas fingers grew in the direction opposite to the flow direction. After 22 percent of the oil was produced, free gas was present in all regions. In both cases, then, there were either isolated patches of oil and gas until a significant amount of the oil has been produced. It appears that even a process like evolution of dissolved gas in a relatively uniform medium can result in non-uniform fluid distribution.

In a more recent experiments, Demiral et al. (1992) observed heterogeneous saturations in CT-scan images of steam, steam foam, and nitrogen foam injected into relatively homogeneous lab samples. They monitored the injected fluids with temperature, pressure, and multiple CT scans. The experimental apparatus consisted of a box with embedded pressure and temperature sensors. They filled the box with unconsolidated Ottawa sand with an average porosity of 39 percent and a permeability of 25 Darcies. They saturated

the medium with distilled water and then injected steam, steam foam, and nitrogen foam. During injection, they collected CT scans at 6 locations in the box. The CT scans revealed information that temperature and pressure alone could not: the actual profile of the flood front. In several cases, the pore fluids were not distributed uniformly.

2.2.2 Partial Saturation and Velocity

In a series of laboratory experiments using unconsolidated quartz sand and glass beads, Domenico (1976) observed the effect of non-uniform distribution of a gas-brine mixture on compressional wave velocities. In these experiments, Domenico introduced partial saturation by flowing a gas-brine mixture through the samples while maintaining a 200 psi pore pressure and a 15 psi differential pressure across the sample. At each saturation point, he measured V_P at 200 kHz. He then compared these measurements with the zero-frequency V_P for a fluid-filled porous solid as given by Geertsma (1961):

$$V_p = \sqrt{\left[\left(K_b + \frac{4}{3}\mu_b\right) + \frac{(1-\beta)^2}{(1-\phi-\beta)/K_o + \phi/K_f}\right]\frac{1}{\rho_b}}, \tag{2.1}$$

where K_b is the dry rock bulk modulus, K_f is the fluid bulk modulus, K_o is the rock mineral bulk modulus, β is the ratio of K_b to K_o, μ_b is the shear modulus, ϕ is the rock porosity, and ρ_b is the bulk density. Note that Equation 2.1 is equivalent to the low-frequency Gassmann theory discussed in Section 2.3.

Domenico observed that the measured V_P was higher than the calculated V_P at each point of partial saturation. This effect was most evident at brine saturation (S_w) exceeding 85 percent: the measured velocities were as much as twice the calculated values. Domenico explained this difference at large values of S_w as a result of non-uniform fluid distribution.

To provide evidence that non-uniform microscopic fluid distribution was the cause of measured V_P exceeding the computed values, Domenico altered his experiment. He used spherical glass beads in an attempt to achieve uniform pore size. His measurements of V_P in this "ideal" sphere pack still exceeded the computed values by a factor of two at high values of S_w. In an attempt to achieve uniform distribution of fluids, Domenico flowed brine through a partially saturated sample at 45 psi pore pressure. This technique, an imbibition process, resulted in measured V_P values much closer to the calculated values. Domenico

concluded that gas was trapped in essentially all pores. The imbibition process was more successful at achieving uniform saturation than the two-phase flow process.

Another notable experimental observation of saturation heterogeneities was reported by Cadoret et al. (1992). The authors conducted a series of resonant bar (1 kHz) experiments on limestone samples. They varied the water saturation by drying (drainage) and depressurization (imbibition). The depressurization process involved spontaneous imbibition, followed by immersion of the sample in water and lowering the pressure to evacuate air from the sample. Resonant bar velocities were measured at incremental steps of saturation varying from 0 to 100 percent S_w. They observered heterogeneities in saturation using X-ray tomography, and they found a marked correlation of resonant bar sonic velocities with the scale of the saturation. The drainage process left isolated patches of air on the scale of a few centimeters, while the imbibition process resulted in a more uniform distribution of fluids. The measured velocities for the imbibition process compared favorably with the Gassmann predictions of velocity versus saturation discussed in Section 2.3. With the drying process, measured velocities exceeded the Gassmann predictions for S_w greater than 80 percent. These results agree with those of Domenico discussed above. One main observation from these results is that saturation heterogeneity can impact measured velocities in the frequency range of well logging tools.

2.2.3 Capillary Pressure, Permeability, and Saturation

It seems clear that if uniform fluid distribution is difficult to obtain in an ideal media such as uniform glass beads, then it would be nearly impossible to expect pore fluids in a hydrocarbon reservoir to be uniformly distributed. For example, in a gas reservoir, variations in pore and pore throat size in the rock would result in spatial variations in capillary pressure behavior: gas and brine distribution would vary spatially. If you assume that capillary pressure is constant in a large volume of rock, spatial variation in the capillary pressure function would cause pore fluid ratios to vary. Capillary pressure can be defined as the difference in pressure between two fluid phases. In a gas reservoir, for example, the capillary pressure, P_c, caused by capillary rise of the water can be calculated from the height above the free water level, h, acceleration of gravity, g, and the difference between the densities of the

fluids, $\Delta\rho$:

$$P_c = \Delta\rho g h \,. \tag{2.2}$$

Knight et al. (1997) use the assumption of uniform capillary pressure to show how variations in clay content might lead to heterogeneous saturations. Clay content would affect the capillary function and the mechanical properties of the rock. The authors calculate V_P for different composite rocks containing varying amounts of clay. They use the capillary functions of the constituent materials to calculate the water saturation in each region, and then they use Gassmann to calculate the saturated elastic moduli for each region. They use the Hashin-Shtrikman bounds to obtain the effective elastic moduli of the composite. They demonstrate how variations in capillary pressure function on a macroscopic scale could affect the global effective elastic moduli at seismic frequencies.

A question that arises here is whether or not rock with similar mechanical properties could exhibit the behavior hypothesized by Knight et al. To illustrate this possibility, I show two core samples from the Staged Field Experiment #2 (Peterson, 1989), a Travis Peak Formation tight gas well in Nacogdoches County, Texas. Table 2.1 gives the properties of these two samples. Note that the elastic moduli were measured on companion samples taken from the core within six inches of the sample depths reported. Elastic moduli are calculated from measurements of *P*- and *S*-wave velocities of 100 percent brine-saturated samples at 31.9 MPa effective stress. The two samples are similar in porosity and in elastic properties. However, the difference in permeability is one indication that the capillary pressure functions, and therefore the saturation histories, of the two samples may vary significantly.

Table 2.1: Travis Peak sandstone properties.

Depth feet	Porosity %	Air Permeability md	Density g/cm^3	K GPa	μ GPa
8270.1	8.2	0.03080	2.538	29.5	24.4
8274.3	7.5	0.00072	2.541	30.1	24.1

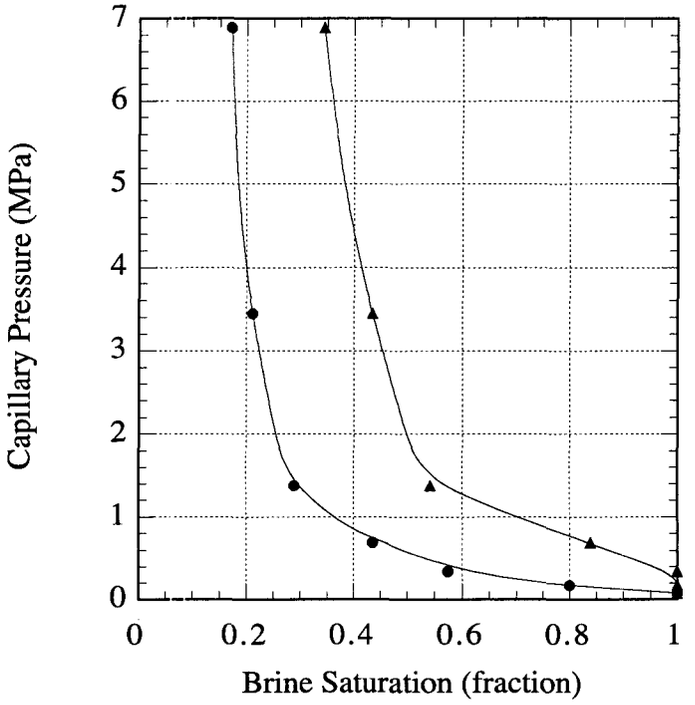

Figure 2.1: Capillary pressure curves for two tight gas sand samples.

2.3 Saturation Effect on Velocity

An important problem faced by the geophysicist interested in seismic monitoring is to quantify the effects of pore fluids and pore pressure on seismic velocities. During hydrocarbon recovery processes, changes in pore fluids and pore pressure can alter the bulk density and the elastic moduli of the saturated rock. The effect on density is the easier of these two characteristics to quantify, provided that the pore fluids do not alter the rock frame, for example, through dissolution. The more complex part of this problem is to quantify the effect of pore fluids on compressional and shear wave velocities. There are two major pore fluid effects that I discuss briefly here: 1) pore fluid substitution and 2) velocity dispersion. Additionally, changes in pore pressure can affect the elastic properties of the reservoir. I will discuss this issue in Chapter 4.

2.3.1 Fluid Substitution Effect

The question of how fluid saturation impacts the compressional and shear wave velocities is one the geophysicist must answer when considering seismic monitoring. On a first order pass, one may want to compare the velocities in rock fully saturated with one fluid to the velocities of the same rock fully saturated with a different fluid. Recall that velocity is related to elastic moduli and density in the following manner:

$$V_P = \sqrt{\frac{K + \frac{4}{3}\mu}{\rho}}, \tag{2.3}$$

$$V_S = \sqrt{\frac{\mu}{\rho}}, \tag{2.4}$$

where V_P is the compressional wave velocity, V_S is the shear wave velocity, ρ is the bulk density, K is the bulk modulus, and μ is the shear modulus. Rock bulk density is a function of the rock mineral density, ρ_{min}, porosity, ϕ, and fluid density, ρ_f, as follows:

$$\rho = (1-\phi)\rho_{min} + \phi\rho_f \,. \tag{2.5}$$

If there is a significant difference in the densities of two saturating fluids, the change in rock bulk density alone could result in detectable changes in both V_P and V_S. However, because of variations in fluid compressibilities, the effective elastic moduli of the rock also change with saturating fluid. To get the full impact of fluid substitution on seismic velocities, we must also consider how the fluids change the elastic moduli.

The primary method used to account for the effect of pore fluid substitution on elastic moduli is given by Gassmann (1951). Gassmann provides the following relationships between the rock mineral bulk modulus, K_o, dry rock bulk modulus, K_{Dry}, saturated bulk modulus, K_{Sat}, fluid bulk modulus, K_f, and rock porosity, ϕ, and between the saturated shear modulus, μ_{Sat}, and the dry shear modulus, μ_{Dry}:

$$\frac{K_{Sat}}{K_o - K_{Sat}} = \frac{K_{Dry}}{K_o - K_{Dry}} + \frac{K_f}{\phi\left(K_o - K_f\right)}, \tag{2.6}$$

$$\mu_{Sat} = \mu_{Dry} \,. \tag{2.7}$$

It is important to note that Gassmann's equations were derived for an incremental load, or a static case (zero frequency), and are considered valid only at low frequencies. For example,

a propagating seismic wave loads the rock with an incremental compression which induces increments of pore pressure. At low frequencies, we often assume there is sufficient time for the fluid to flow within the pore space, eliminating any pore pressure gradients. This is generally considered to be a good assumption for seismic frequencies, but it may not be valid for logging frequencies, depending on the rock type and fluid viscosity.

Other assumptions of Gassmann include isotropic rock, constant bulk and shear moduli for all mineral constituents, and full saturation with a single fluid. Since the reservoir rocks rarely meet these assumptions, we must extend the Gassmann relationships to "real" rocks. We might convince ourselves that the isotropic assumption is applicable in a given case, but rocks in the real world are composed of several minerals which most likely do not have uniform elastic moduli. Fortunately, there are several ways to average the mineral properties to get effective elastic moduli, such as the Voigt (1928) upper bound, the Reuss (1929) lower bound, and the Hashin-Shtrikman (1963) bounds. An accepted way to compute the effective mineral moduli is to use the arithmetic average of the Voigt and Reuss bounds, proposed by Hill (1952), which is called the Voigt-Reuss-Hill average. For a rock with N constituent minerals, the expression for computing the effective mineral bulk modulus, K_o, using the Voigt-Reuss-Hill average is:

$$K_o = \frac{1}{2}\left(\sum_{i=1}^{N} f_i K_i + \left(\sum_{i=1}^{N} \frac{f_i}{K_i}\right)^{-1}\right) , \tag{2.8}$$

where f_i is the volume fraction and K_i is the bulk modulus of each mineral constituent. This value for K_o can then be used in Equation 2.6 to calculate the effective saturated bulk modulus of the rock.

The most abundant elastic property data for hydrocarbon reservoir rocks is derived from well logs. In the best case, we have measurements of V_P, V_S, density, and fluid saturations. With this information, the saturated bulk and shear moduli are known for the saturation conditions that exist in the reservoir near the well bore. A typical virgin oil reservoir might contain 70 to 80 percent oil, with the remaining pore space containing brine. In this case, the well log measurement of K_{Sat} is for rock containing a mixture of fluids, not a pure fluid, as assumed by Gassmann. I will discuss this issue further in Section 2.4. Someone interested in reservoir monitoring of a water flood of this typical oil reservoir would want

to predict the observable changes as water sweeps oil from regions of the reservoir. In order to do so, comparing oil-saturated rock velocities to brine-saturated rock velocities would give an indication of the seismic observables. The following formulation of Equation 2.6 is a way to directly compare the bulk moduli of the reservoir rock saturated with two fluids, annotated with subscripts 1 and 2:

$$\frac{K_{Sat_1}}{K_o - K_{Sat_1}} - \frac{K_{f_1}}{\phi\left(K_o - K_{f_1}\right)} = \frac{K_{Sat_2}}{K_o - K_{Sat_2}} - \frac{K_{f_2}}{\phi\left(K_o - K_{f_2}\right)}, \tag{2.9}$$

$$\mu_{Sat_1} = \mu_{Sat_2}\,. \tag{2.10}$$

To predict the observable changes, the next step would be comparing the P- and S-wave velocities of the rock saturated with the two fluids using Equations 2.3 and 2.4. Notice the implication of the Gassmann assumption of constant shear modulus μ: variations in V_S are caused only by changes in rock bulk density. Also, with some algebraic manipulation of Equation 2.9, it is apparent that if $K_{f_1} > K_{f_2}$, then $K_{Sat_1} > K_{Sat_2}$. The change in V_P is dependent, however, on both changes in bulk density and bulk modulus of the saturated rock. It is possible for the P-wave velocity of the stiffer rock to be the smaller of the two (i.e. $V_{P_1} < V_{P_2}$) if the change in bulk density is large enough compared to the change in K_{Sat}. Recall from Equation 2.3 that an increase in bulk modulus will increase the P-wave velocity, while an increase in density will lower it. This could happen for a rock saturated with a compressible gas compared to the same rock saturated with relatively incompressible brine. An example of this will be given in Section 2.4.3.

2.3.2 Dispersion Effects

Another manner in which fluid saturation can affect seismic wave propagation is through velocity dispersion. Spatially varying fluid saturation can cause variations in seismic wave velocities. Unlike the case described above where fluid pressures equilibrate as the wave propagates, here there can be fluid flow caused by pore pressure gradients between patches in the rock saturated with different fluids.

The amount of velocity dispersion and attenuation in a medium with inhomogeneous saturation distribution depends on fluid properties, rock properties, and the geometry of

heterogeneities. White (1975) presented a model for seismic velocity dispersion in brine-saturated rock containing gas-filled spherical patches. White extends the Gassmann relationships to include coupling of fluid flow waves and seismic body waves. In his analysis, he shows that pressure gradients at the boundary between the gas-filled patches and the brine-saturated rock cause fluid flow, resulting in a local energy loss. For an unconsolidated sand saturated with brine, White shows that the presence of spherical gas patches causes a *P*-wave velocity increase of 18 percent. However, at low frequencies, the velocities from this model are higher than the Gassmann low-frequency limit. Dutta and Seriff (1979) report a correction to White's model which brings the low frequency velocities in line with the Gassmann theory.

Dutta and Odé (1979) improved on the White model by incorporating Biot's poroelasticity equations. Their approach accounted for coupling between the rock frame and the pore fluid. In agreement with the corrected White model, the results shown by Dutta and Odé approach the low-frequency Gassmann velocities for partially saturated rock.

More recent works by Mavko and Nolen-Hoeksema (1994) and Le Ravalec et al. (1996) found that a combination of heterogeneous or "patchy" saturation and grain-scale squirt flow was necessary to explain published sonic and ultrasonic lab data.

2.4 Fluid Distribution and Seismic Response

In this section, I investigate the effect fluid distribution might have on the seismic velocity of rock at various states of saturation with three fluids - oil, water, and gas. First, I describe the models used in this study, then I compare the results for different rock types.

2.4.1 Fluid Distribution Models

I present three models for the way multiple fluid phases might be distributed in the pore space of a given rock. For all three saturation models, I assume that the rock is an effective medium with the variation in saturations occurring on scales much smaller than a seismic wavelength. The seismic frequencies are low enough that Biot (1956) and Squirt (O'Connell and Budiansky, 1977; Mavko and Jizba, 1991) dispersion mechanisms can be ignored. I also assume that the dry rock is isotropic and homogeneous in all three models,

even though the fluids are distributed heterogeneously in the patchy and lamination models. Although heterogeneity in the rock is one of the primary reasons fluids might be distributed heterogeneously, our purpose is to demonstrate how the fluid distribution alone can affect seismic velocities.

Uniform Effective Fluid Model

The uniform effective fluid model assumes that the oil, gas, and water phases are uniformly intermingled at the smallest scale within the pore space. The micropatches that exist are small enough (less than a few cm) that wave-induced pore pressure increments are the same throughout all phases. This fluid iso-stress allows us to replace the three phases with an equivalent or "effective" fluid (Domenico, 1976). Figure 2.2 shows a representation of this model, where an injected fluid disperses uniformly through the pore space, resulting in an effective fluid behind the flood front that is different than the in-situ fluid. The bulk modulus of the effective fluid, K_f, is described by the Reuss (1929) average of the individual constituents' bulk moduli, K_{f_i}, as follows:

$$K_f = \left(\sum_i \frac{f_i}{K_{f_i}} \right)^{-1} . \tag{2.11}$$

I then estimate the bulk modulus of the rock saturated with the effective fluid, K_{Sat}, from Gassmann's relationship (Equation 2.6), using the rock mineral bulk modulus, K_o, dry rock bulk modulus, K_{Dry}, rock porosity, ϕ, and the fluid bulk modulus from Equation 2.11.

Patchy Model

In the patchy model, patches of rock exist that contain distinct fluid phases or fluid mixtures. The dry rock is considered to be homogeneous, and the heterogeneity exists only in the distribution of fluids . This model could represent, for example, regions in the reservoir that are bypassed in a secondary recovery process. The patches are assumed to be small compared to the seismic wavelength but large enough that wave-induced increments of pore pressure do not have time to equalize from patch to patch during a seismic period. Within each patch there is a single fluid or a multi-phase mix of pore fluids which acts locally as

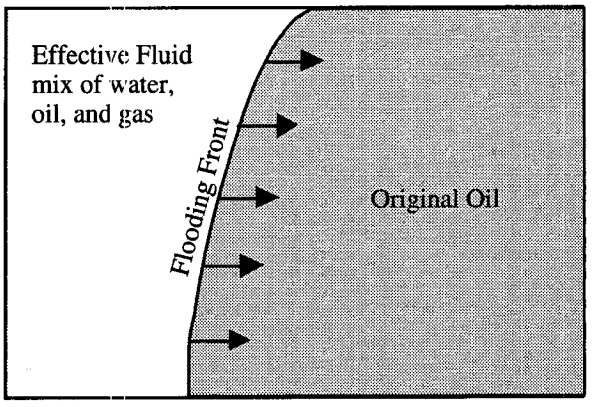

Figure 2.2: Uniform fluid distribution model. The gas-oil-water phases behind the front are at a different ratio than ahead of the front.

an effective fluid. A representation of this model is shown in Figure 2.3. The flood front has invaded distinct regions in the reservoir to different degrees, bypassing some regions, and leaving isolated patches that have different saturations than the swept region. The effective medium is, then, a mixture of the reservoir rock with different states of saturation. The bulk modulus of the effective fluid in each patch is calculated using Equation 2.11. The bulk modulus of the saturated rock in each patch is calculated using Equation 2.6. In keeping with the low frequency Gassmann theory, I assume that the rock shear modulus is uniform, independent of the saturation condition. The limiting effective modulus of the medium containing many unrelaxed ("undrained") patches is found by applying the relationship given by Hill (1963) for a composite with a uniform shear modulus:

$$\frac{1}{K_{eff} + \frac{4}{3}\mu} = \sum_{i=1}^{N} \left(\frac{f_i}{K_{Sat_i} + \frac{4}{3}\mu} \right) . \tag{2.12}$$

The effective bulk modulus, K_{eff}, depends only on the volume fraction, f_i, and bulk modulus, K_{Sat_i}, of each patch and is independent of the patch shape.

In general, the effective modulus will be frequency dependent (White, 1975; Dutta and Odé, 1979), even at low (seismic) frequencies. The patchy model, with modulus given by Equation 2.12, represents the high frequency limit; the uniform fluid model represents the low frequency limit. The frequency dependence between these limits depends on the details of patch shapes. However, a simple estimate of the characteristic frequency, f_c, separating the high and low frequency behavior is given by $f_c \approx D/l^2$, where D is the

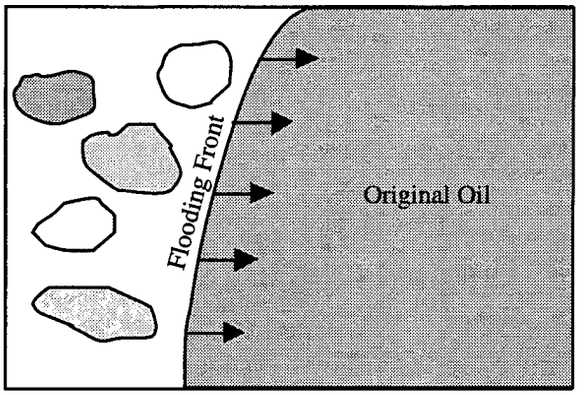

Figure 2.3: Fluid distribution in patchy model. An injected fluid invades regions of reservoir rock to different degrees, leaving patches with varying saturations behind the front.

hydraulic diffusivity, and l is the typical patch size. The characteristic time for diffusive relaxation over scales $\sim l$ is $\tau \approx 1/f_c$. The hydraulic diffusivity is related to permeability, κ, fluid viscosity, η, and fluid bulk modulus, K_f, in the following manner:

$$D = \frac{\kappa K_f}{\eta} . \tag{2.13}$$

So, the patchy model is valid when the combination of fluid and rock properties result in a characteristic frequency less than the seismic frequency. For example, given a patch length of 1 meter in a rock with 3 Darcy permeability, and the patch is saturated with a 1 cp viscosity fluid having a bulk modulus of 2.2 GPa, the characteristic frequency is approximately 7 Hz. So, for seismic frequencies exceeding 7 Hz, this medium would exhibit patchy behavior.

Laminated Fluid Model

The laminated fluid model assumes that distinct fluid saturation patches exist as layers. As before, we consider the underlying dry rock to be homogeneous. An example of this type of distribution could be fingering of an injected fluid or gravitational segregation of phases into layers of rock. Within each layer there is a single or multi-phase mix of fluids which acts locally as an effective fluid. Figure 2.4 shows a representation of this model with horizontal layers. The effective medium in this model is a mixture of layers of the reservoir rock with different states of saturation.

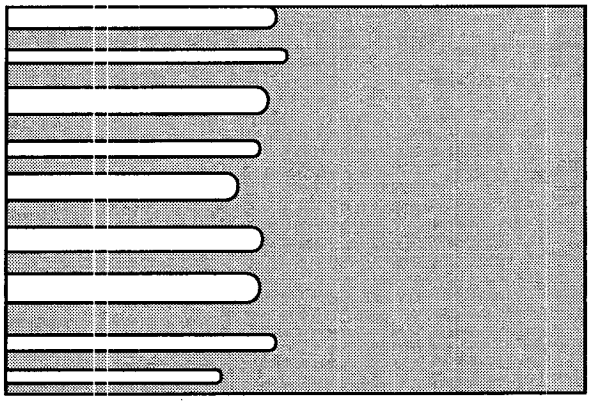

Figure 2.4: Laminated fluid model. An injected fluid invades layers of reservoir rock to different degrees, resulting in a layered saturation profile behind the front.

One might expect the layering to result in different seismic velocities perpendicular to and parallel to the layers. Again, the bulk modulus of the effective fluid within each layer is calculated using Equation 2.11, and the saturated rock bulk modulus of each layer is calculated using Equation 2.6. Using the Backus (1962) average, the P-wave moduli, M_V and M_H, in the directions perpendicular and parallel to the layers are calculated as:

$$M_V = \left\langle 4\rho V_S^2 \left(1 - \frac{V_S^2}{V_P^2}\right)\right\rangle + \left\langle 1 - 2\left(\frac{V_S^2}{V_P^2}\right)\right\rangle^2 \left\langle \left(\rho V_P^2\right)^{-1}\right\rangle^{-1}, \tag{2.14}$$

$$M_H = \left\langle \left(\rho V_P^2\right)^{-1}\right\rangle^{-1}, \tag{2.15}$$

where the $\langle\ \rangle$ operator refers to a volume average, and V_P, V_S, and ρ are the spatially varying P- and S-wave velocities and density. Since I assume a uniform shear modulus, Equation 2.14 reduces to Equation 2.15, or $M_V = M_H$. This laminated medium, then, behaves isotropically with respect to velocity. Equation 2.15 is equivalent to Equation 2.12 (since $M = K + 4\mu/3$). Hence, the patchy and lamination models are expected to have identical velocity signatures, assuming that the patches and layers are smaller than the wavelength. Looking at only the seismic velocities, we do not expect to distinguish between saturation in patches and saturation in layers. However, these models might have a different frequency dependence of seismic velocities, depending on the geometries of the patches.

From this result, we see the simplicity of the patchy model: the modulus of the saturated rock is independent of patch shape. Mavko and Mukerji (1997) show that the modulus

given by Equation 2.12 represents an upper bound, and the modulus given by Gassmann (Equation 2.6) represents a lower bound at seismic frequencies.

2.4.2 Comparison of Models

I compared the calculated compressional wave velocities using dry rock properties based on ultrasonic velocities in Beaver sandstone ($\phi = 0.064$) at 5 MPa effective pressure (Han, 1986) with water, oil, and gas as the saturating fluids. The oil was 15°API with no dissolved gas, and the gas had a specific gravity of 1.0 compared to air at 15.6°C and atmospheric pressure. The fluid properties as a function of temperature and pressure were calculated using the relationships provided by Batzle and Wang (1992). Since the lamination model has the same seismic velocity signature as the patchy model, I compared only the uniform fluid and patchy models. We show only the calculated compressional wave velocities (V_P). Because I assume a uniform shear modulus, the shear wave velocity changes only as a result of changes in bulk density. Also, for the patchy model, I consider only the case where each patch is saturated with a single fluid phase. This is the upper-limiting case. There could be many other realizations of the patchy model, such as mixing fluids within patches.

Figure 2.5 shows V_P in Beaver sandstone calculated for mixtures of water and gas. The water-saturated rock has a higher velocity than the gas-saturated rock. An increase in gas saturation (S_g) from 0 to 0.01 results in a large decrease in V_P using the uniform fluid model. For the patchy model, the large drop in velocity is not seen: V_P decreases almost linearly with increasing S_g. The characteristics observed in the water-gas system are also exhibited by the oil-gas system (Figure 2.6). For other realizations of patchy fluid distribution, such as mixing water and gas in some patches, the resulting curve for the patchy model would fall between the two curves shown in Figure 2.5. One can easily imagine a series of curves which result from varying the saturations within the patches.

Velocity Dispersion and Scale

The velocity dispersion evident in Figure 2.5 is caused by the scale of the fluid distribution. As mentioned previously, in the uniform fluid model, wave-induced pore pressure increments diffuse during a seismic period. In contrast, in patchy fluid model, the pore fluids

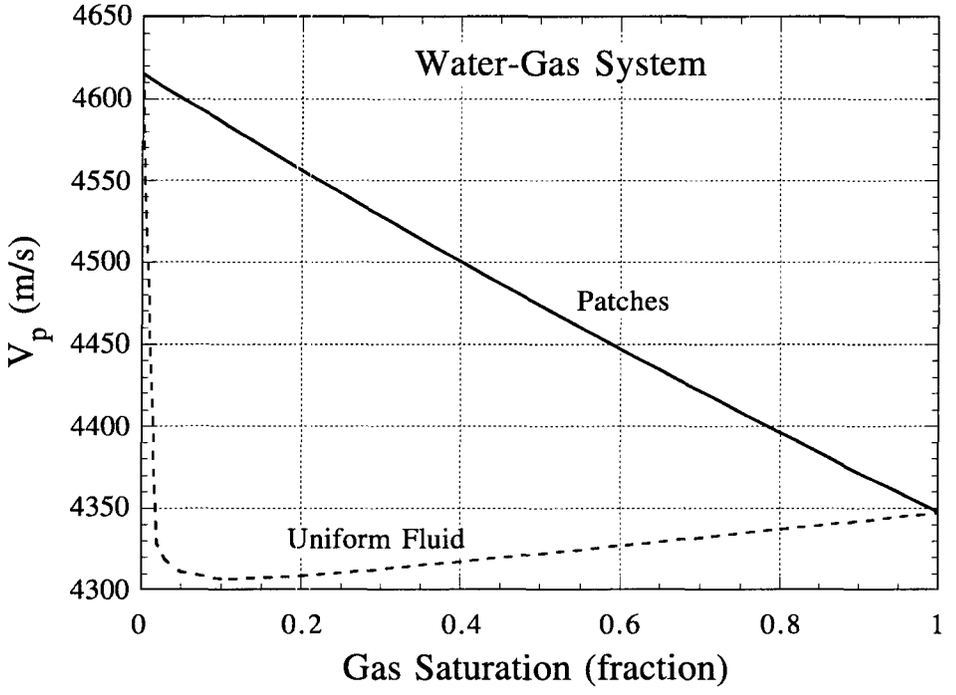

Figure 2.5: Comparison of models in Beaver sandstone for water-gas fluid system at 20°C, 3 MPa pore pressure, and 5 MPa effective pressure.

are distributed in such a way that the pore pressure increments do not equilibrate during a seismic period. This results in higher velocities for the patchy fluid distribution. As long as the patch length exceeds the characteristic diffusion length (and is less than the seismic resolution), the patchy model yields the correct velocity. This length depends on the frequency, as discussed in Section 2.4.1.

Effect of Temperature

Figure 2.6 shows the effect of temperature the *P*-wave velocity calculated using the uniform fluid model and an oil-gas pore fluid system for Beaver sandstone at 3 MPa pore pressure and temperatures of 20°C and 150°C. The liquid-saturated rock the highest velocity. The largest change in velocity (4.6 percent decrease) with the increase in temperature is seen in the rock with 100 percent oil saturation. The entire region of $S_g > 0.02$ shows a variation in *P*-wave velocity of less than 50 m/s, (less than one percent), making it difficult to determine the fluid saturation from only the velocity.

The velocities calculated with the patchy model are also shown in Figure 2.6. Again, the largest change in velocity with temperature is seen in the oil-saturated rock, and there is a fairly linear drop in velocity with gas saturation. At these pressure and temperature conditions, there was little change in the *P*-wave velocity of the water-saturated rock. The largest percentage change in velocity for a three-phase fluid system was in the region of high oil saturation.

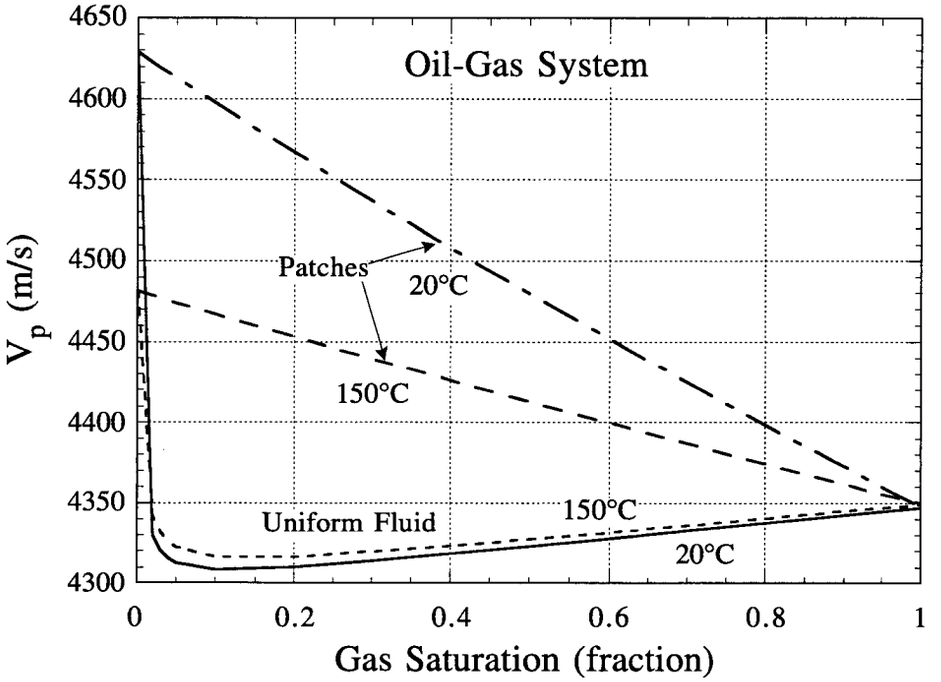

Figure 2.6: Comparison of models using Beaver sandstone for oil-gas fluid system at 20°C and 150°C, 3 MPa pore pressure, and 5 MPa effective pressure.

Effect of Pressure

I next consider the effect of pore pressure, with the effective pressure kept constant. Figure 2.7 shows the *P*-wave velocity computed using the uniform fluid model at a temperature of 20°C and at pore pressures of 3 MPa and 15 MPa. The higher pressure results in a smaller decrease in velocity with the addition of small amounts of gas. The maximum velocity change caused by the increase in pressure is in the region where gas saturation is

less than 11 percent. The 100 percent liquid-saturated rock shows an increase in P-wave velocity of less than 20 m/s (less than 0.5 percent). At $0 < S_g < 0.11$, the increase in P-wave velocity resulting from the increase in pressure is greater than 100 m/s, ranging from 2.3 to 5.3 percent increase in V_P.

The results for a patchy distribution of oil and gas are also shown in Figure 2.7. With the increase in pressure, the maximum velocity increase is 20 m/s (less than 0.5 percent), making it difficult to detect any velocity change as a result of increasing pore pressure to 15 MPa.

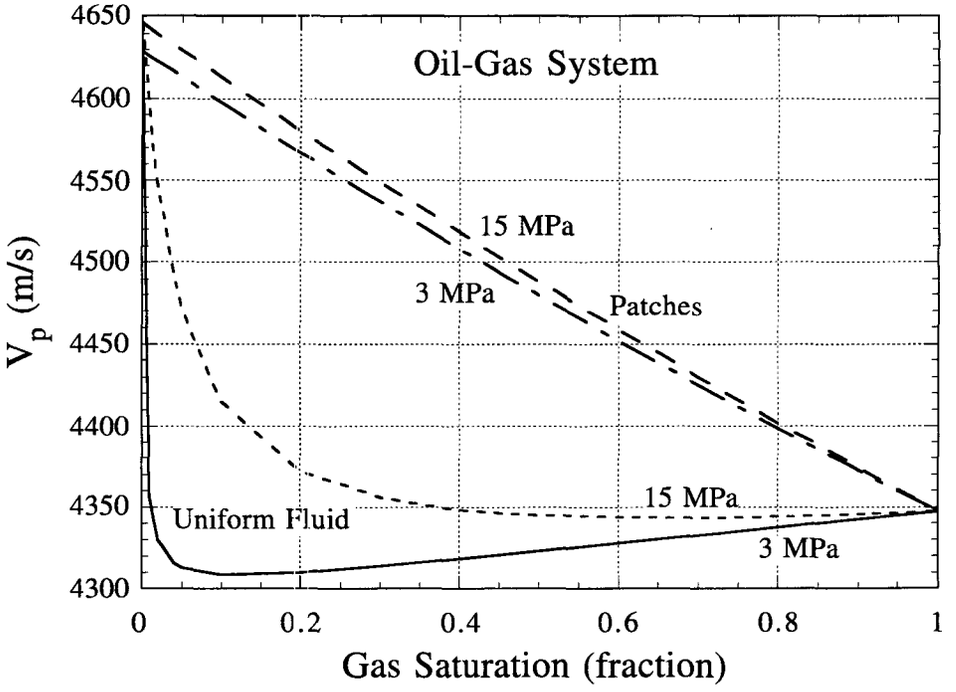

Figure 2.7: Comparison of models using Beaver sandstone for oil-gas fluid system at 3 MPa and 15 MPa pore pressure, 20°C, and 5 MPa effective pressure.

2.4.3 Other Rock Types

I apply the fluid distribution models to two clean sands with larger porosity than the Beaver sandstone - Ottawa sand (Domenico, 1977), and Fontainebleau sandstone (Han, 1986). Properties of all three samples at 5 MPa effective pressure are shown in Table 2.2. Ternary diagrams shown in Figures 2.8-2.9 display V_P and I_P in the rocks over the full range of

Table 2.2: Ottawa sand, Fontainebleau and Beaver sandstone properties at 5 MPa effective pressure.

Sample	Porosity %	Density g/cm^3	K_{Dry} GPa	μ_{Dry} GPa
Ottawa sand	37.9	1.645	0.663	0.761
Fontainebleau	15.4	2.236	18.07	19.07
Beaver	6.36	2.466	16.08	22.94

saturation for both the uniform fluid and patchy models. Each corner of the ternary diagram represents rock that is fully saturated with one fluid, either oil, water, or gas. Each edge of the diagram represents a two-phase fluid system.

For each rock type, there are 6 ternary diagrams. The top two rows in Figure 2.8- 2.9 show the modeling results for Ottawa sand, and the bottom two rows show the results for Fontainebleau. For each rock type, the first row shows the results for the uniform fluid model, and the second row show the results for the patchy model. Each row shows how V_P (or I_P) varies for a given model with changes in temperature and pressure. The diagrams in the left column compare V_P (or I_P) between the uniform fluid and patchy models at 3 MPa pore pressure and 20°C. The other columns show the effect of an increase of pore pressure to 15 MPa at constant temperature (middle) and with an increase of temperature to 150°C at constant pressure (right). The color scales are the same in all 6 diagrams for Ottawa sand. A different scale is used for the Fontainebleau diagrams.

For the high porosity Ottawa sand, the patterns of velocity distribution are similar to what was seen for the low porosity Beaver sandstone. The patchy model shows a monotonic decrease in V_P with increasing gas saturation (S_g), and the uniform fluid model shows a small sensitivity to S_g. The uniform fluid model is relatively sensitive to an increase in pressure, with a maximum increase of 61 percent in V_P and I_P. This model shows poor sensitivity to changes in temperature, except for the region with only oil and water pore fluids, where the maximum decrease in V_P is 30 percent, and the maximum decrease in I_P is 33 percent. When gas is present in the pore space, there is actually an increase in V_P as a result of the increased temperature, with a maximum increase of 5 percent. I_P drops slightly over most of the range of S_g. The patchy model is relatively insensitive to increases in pressure, with a maximum increase of 3.4 percent in V_P. For S_g >0.25, changes in I_P

range from 4 to 8.6 percent. This model is relatively sensitive to an increase in temperature in the region of high oil saturation, with a maximum decrease of 30 percent in V_P and a maximum decrease of 33 percent in I_P. Again, I assume a constant effective stress in order to isolate the pore fluid effect on V_P and I_P. Unconsolidated sand is quite sensitive to effective stress, and incorporating this into the modeling could have a significant impact on the results.

For Fontainebleau sandstone, the patchy model shows poor sensitivity to saturation, with less than 0.7 percent variation in V_P over the range of three-phase saturation. Although the uniform fluid model shows a large decrease in V_P at low values of S_g, there is much better sensitivity to saturation than in the Beaver sandstone. As seen in the Beaver sandstone, the uniform fluid model was relatively sensitive to an increase of pore pressure, with maximum increases in V_P and I_P of 2.6 percent, while it is relatively insensitive to an increase in temperature, with a maximum decrease of 2 percent in V_P and 3 percent in I_P. The results for the patchy model are similar to those obtained using the Beaver sandstone. The model is relatively insensitive to changes in pore pressure, with maximum changes in V_P and I_P of less than 1 percent. The effect of increasing temperature using the patchy model is again strongest at high oil saturation, with maximum decreases of 2 percent in V_P and 3 percent in I_P. The most striking result here is that the 100 percent oil-saturated rock now has a lower velocity than the 100 percent gas-saturated rock (true for both models) at the higher temperature. The increase in temperature results in a 58 percent decrease in the oil bulk modulus and an 8.3 percent decrease in K_{Sat}. Though K_{Sat} for the oil-saturated rock is still larger than for gas-saturated rock, the higher density of the oil-saturated rock results in a lower V_P. However, the gas-saturated rock has a lower I_P than the oil-saturated rock.

2.4.4 Velocity Changes During Steam Flooding

In a steam flood, changes in seismic velocity will result from changes in temperature, pressure, and pore fluid saturation. The properties of oil, gas, and water change as a result of temperature and pore pressure changes. The changes in the pore fluids will result in variations in the seismic properties of the reservoir. Another possible source of changes in seismic properties of rock is distillation of the reservoir oil. Injection of high temperature

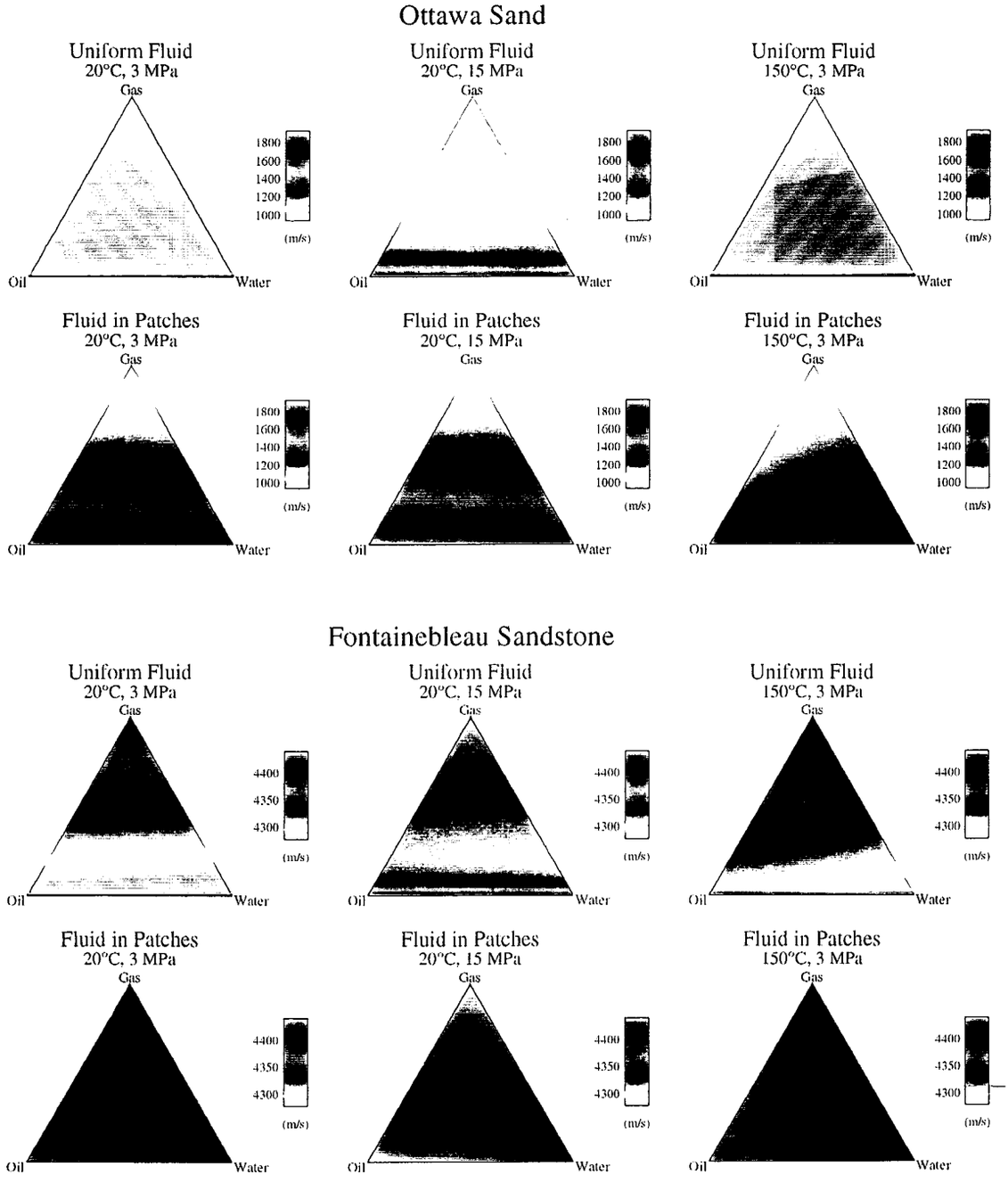

Figure 2.8: Ternary diagrams showing the variation in V_P with fluid saturation in Ottawa sand (top 2 rows) and Fontainebleau sandstone (bottom 2 rows). The corners of each diagram are labeled to indicate the saturating fluid. Effective pressure is 5 MPa in all diagrams.

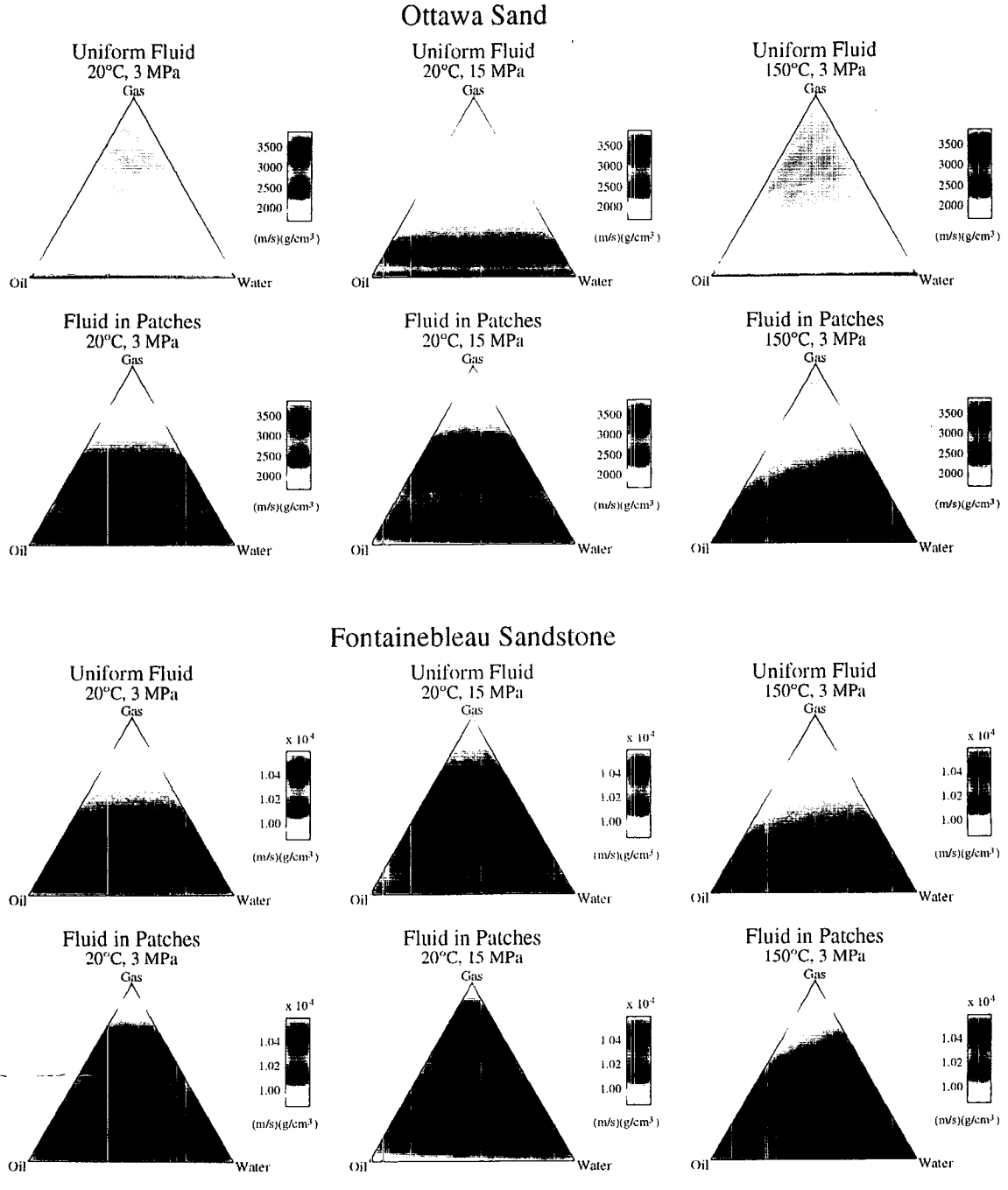

Figure 2.9: Ternary diagrams showing the variation in I_P with fluid saturation in Ottawa sand (top 2 rows) and Fontainebleau sandstone (bottom 2 rows). The corners of each diagram are labeled to indicate the saturating fluid. Effective pressure is 5 MPa in all diagrams.

steam causes the oil to distill into its lighter fractions, which also leaves a heavier residuum than the initial oil. For example, the distillation of an oil with an initial API gravity of 15° might result in a 34°API distillate and an 8°API residuum (Lim et al., 1992). After distillation, the lighter components condense as the steam condenses, and this distillate blends with the reservoir oil ahead of the steam front, resulting in an oil lighter than the initial reservoir oil (Prats, 1982). Production of oil lighter than the initial reservoir oil has been observed in steam-flooded fields, according to Prats (1982) and Lim et al. (1992). The produced oil can be from 2° to 4°API lighter than the initial reservoir oil. The question that arises here is whether the choice of the gravity of oil will make a significant difference in the rock physics modeling of the seismic response of a steam flood or for inversion of seismic data for fluid identification. To answer this question, I calculated the velocities expected for an initial oil of 15°API, a distillate of 34°API, and a residuum of 8°API using both the uniform fluid and patchy models. Figure 2.10 shows the results at a temperature of 20°C and 3 MPa pore pressure. Using the uniform fluid model, there is no significant difference in the velocities for the oil-gas system using either of the oils. However, using the patchy model, at high values of oil saturation, there are significant differences in the calculated velocities. Figure 2.11 shows the same oils at 150°C and 3 MPa pore pressure. Comparing the uniform fluid models at both temperatures shows that the difference in velocity calculated for the different oils is not significant except in the region where $S_g < 0.02$.

Comparing the velocities from the patchy model for all three oils at 20°C and 150°C reveals which regions are critical for knowing what oil to use in the calculations. In a steam flood, oil saturations in the swept zone can be less than 10 percent. In the region of oil saturation less than 10 percent, there is less than a 20 meter/second difference in the velocities calculated at the two temperatures. However, in the regions of high oil saturation, the choice of which oil to use is more important. For example, at 80 percent oil saturation ($S_g = 0.2$), an increase in temperature from 20°C to 150°C would result in a velocity decrease of approximately 200 m/s (13.2 percent) if we assume the initial oil has only been heated up. If we assume the initial oil has been distilled, the region where the lighter fractions condense might see a velocity decrease of 270 m/s (18.3 percent) compared with the initial oil at 20°C and a saturation of 80 percent.

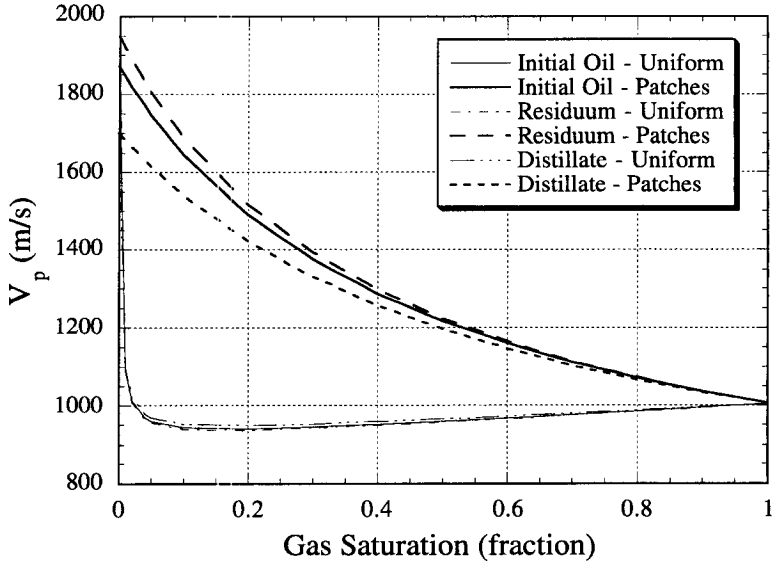

Figure 2.10: Comparison of models in Ottawa sand for oil-gas fluid system for 3 oils at 20°C, 3 MPa pore pressure, and 5 MPa effective pressure.

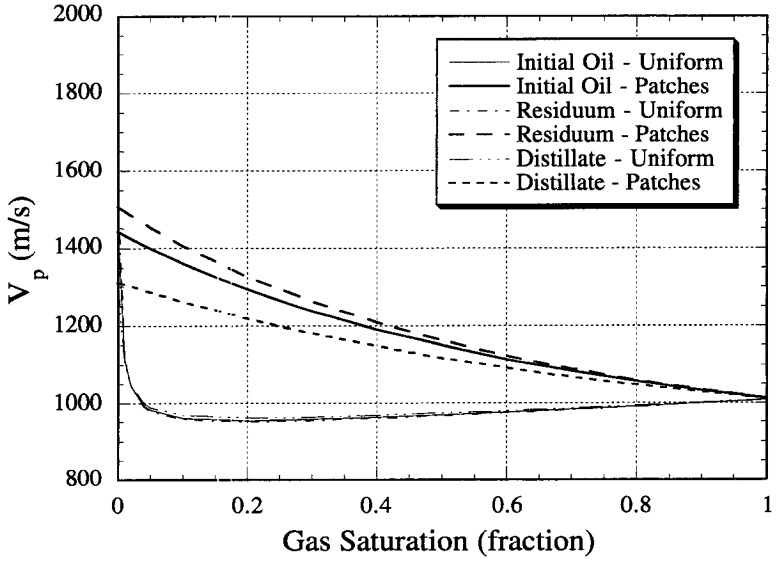

Figure 2.11: Comparison of models in Ottawa sand for oil-gas fluid system for 3 oils at 150°C, 3 MPa pore pressure, and 5 MPa effective pressure.

2.5 Conclusions

Based on the fluid distribution models presented here and considering the particular rock-fluid systems (at 5 MPa constant effective pressure) studied here, I make the following conclusions:

1. In an effective medium with uniform shear modulus where the fluid is distributed in layers, the *P*-wave velocity is the same in directions parallel and perpendicular to these layers.

2. The uniform fluid model shows relative insensitivity to gas saturation in both low and high porosity rocks.

3. The uniform fluid model is relatively sensitive to increases in pore pressure but relatively insensitive to increases in temperature for all three rocks.

4. The patchy model is relatively sensitive to increases in temperature but relatively insensitive to increases in pore pressure for all three rocks.

5. In an intermediate porosity rock, such as the Fontainebleau sandstone, V_P can be lower in oil-saturated rock than in gas-saturated rock. The implication here in recovery monitoring is that low velocity does not necessarily indicate the presence of gas.

6. In modeling the seismic response of a steam flood, it is important to consider how the fluid is distributed. Further, it is important to consider the distillation of steam in the regions of high oil saturation.

2.6 References

Backus, G., 1962, Long-wave elastic anisotropy produced by horizontal layering: Journal of Geophysical Research, **67**, 4427–4440.

Batzle, M. and Wang, Z., 1992, Seismic properties of pore fluids: Geophysics, **57**, 1396–1408.

Biot, M. A.,1956, Theory of propagation of elastic waves in fluid saturated porous solid. I. Low frequency range: J. Acoust. Soc. Am., **28**,168–191.

Cadoret, T., Marion, D., and Zinszner, B., 1992, 1 kHz elastic wave velocities in partially saturated limestones; evidence of fluid distribution effect: SEG Annual Meeting Expanded Technical Program Abstracts with Biographies, **62**, 658–661.

Chatenever, A., and Calhoun, J. C., 1952, Visual examinations of fluid behaviour in porous media - Part I: Petroleum Transactions, AIME, **195**, 149–156.

Demiral, B.M.R., Pettit, P.A., Castanier, L.M., and Brigham, W.E., 1992: A three-dimensional steam injection model allowing in situ saturation measurements: Report to U.S. Department of Energy, DOE/BC/14600-33.

Domenico, S. N., 1976, Effect of brine-gas mixture on velocity in an unconsolidated sand reservoir: Geophysics, **41**, 882–894.

Domenico, S. N., 1977, Elastic properties of unconsolidated porous sand reservoirs: Geophysics, **42**, 1339–1368.

Dutta, N.C., and Odé, H., 1979, Attenuation and dispersion of compressional waves in fluid-filled porous rocks with partial gas saturation (White model)–Part I:Biot theory, Part II: Results: Geophysics, **44**, 1777–1805.

Dutta, N.C., and Seriff, A.J., 1979, On White's model of attenuation in rocks with partial gas saturation: Geophysics, **44**, 1806–1812.

Gassmann, F., 1951, Elastic waves through a packing of spheres: Geophysics, **16**, 673–685.

Han, D.-H., 1986, Effects of porosity and clay content on acoustic properties of sandstones and unconsolidated sediments: Ph.D. thesis, Stanford University.

Hashin, Z., and Shtrikman, S., 1963, A variational approach to the elastic behavior of multiphase materials, Journal of the Mechanics and Physics of Solids, **11**, 127–140.

Hill, R., 1952, The elastic behavior of crystalline aggregate: Proc. Phys. Soc. London, **A65**, 349–354.

Hill, R., 1963, Elastic properties of reinforced solids: Some theoretical principles: Journal of the Mechanics and Physics of Solids, **11**, 357–372.

Knight, R., Dvorkin, J., and Nur, A., 1997, Seismic signatures of partial saturation: Geophysics, in press.

Le Ravalec, M., Guéguen, Y., and Chelidze, T., 1996, Elastic wave velocities in partially saturated rocks: Saturation hysteresis: J. Geophys. Res., **101**, 837–844.

Lim, K.T., Ramey, H.J., Jr., and Brigham, W.E., 1992, Steam distillation effect and oil quality change during steam injection: Report to U.S. Depar tment of Energy, DOE/BC/14600-18.

Mavko, G., and Jizba, D., 1991, Estimating grain-scale fluid effects on velocity dispersion in rocks: Geophysics, **56**, 1940–1949.

Mavko, G., and Nolen-Hoeksema, R., 1994, Estimating seismic velocities at ultrasonic frequencies in partially saturated rocks: Geophysics, **59**, 252–258.

Mavko, G., and Mukerji, T., 1997, Bounds on low frequency seismic velocities in partially saturated rocks: Submitted to Geophysics.

O'Connell, R. J., and Budiansky, B., 1977, Viscoelastic properties of fluid-saturated cracked solids: J. Geophys. Res., **82**, 5719–5735.

Peterson, R., Staged field experiment #2: Application of advanced geological, petrophysical and engineering technologies to evaluate and improve gas recovery from low permeability sandstone reservoirs - Volume 1: Technical report, Gas Research Institute, 1989.

Prats, M., 1982, Thermal Recovery: Monograph Series, **7**, Society of Petroleum Engineers.

Reuss, A., 1929, Berechnung der fleissgrense von mischkristallen auf grund der plastizitatsbedinggung fur einkristalle: Zeitschrift fur Angewandte Mathematik und Mechanik, **9**, 49–58.

van Meurs, P., 1957, The use of transparent three-dimensional mode ls for studying the mechanism of flow processes in oil reservoirs: Transactions, AIME, **210**, 295–301.

Voigt, 1928, Lehrbuck der Kristallphysik: Teubner, Leipzig.

White, J.E. 1975, Computed seismic speeds and attenuation in rocks with partial gas saturation: Geophysics, **40**, 224–232.

Chapter 3

Seismic Detection of Oil Production

3.1 Abstract

In this chapter, I present a feasibility study on monitoring primary oil production in the Troll field by means of repeated seismic surveys (4D seismic). Reservoir flow simulation provided by Norsk Hydro revealed the potential for gas coning in the oil zone, which could significantly reduce the life of a production well. By using these flow simulation results, I calculate compressional wave velocities and impedances within the reservoir for 4 level of gas saturation in the gas cone: 20, 40, 60, and 80 percent. For each case, I considered both uniform fluid and patchy fluid distributions, and I model the seismic response for each. I show that for a uniform fluid distribution, differences in seismic signatures provide a basis for identifying areas of gas coning. For patchy fluid distribution, seismic differences may be obscured by noise levels in the data, especially when the gas saturation is low. I also investigated the issue of lateral resolution by averaging the reservoir properties over a 50 m radius. The net effect of this smoothing was to reduce the amplitude and to increase the length of the seismic anomaly.

3.2 Introduction

Obtaining a better description of the internal structure and fluid flow in a producing reservoir through seismic surveys provides a direct way to significantly improve the recovery of

hydrocarbons. The central idea of seismic recovery monitoring is to determine in situ temperature, saturation, and fluid type from temporal changes of seismic signatures (reflections and velocities). Rock physics provides the necessary tools to predict and interpret seismic changes associated with recovery processes.

The following factors control the change of seismic signatures on a static geological background: pore pressure, fluid compressibility and density, and temperature. Fluid compressibility and density in turn depend on water, oil and gas saturation, water salinity, oil gravity, gas gravity, temperature, pore pressure, and gas-oil ratio.

We can estimate the impedance of fluid-saturated rock from dry rock elastic moduli and density, and pore fluid compressibility and density. Therefore, recovery monitoring requires two types of rock physics data: (1) elastic properties of the dry rock versus confining pressure, and its density, and (2) effective compressibility and density of the pore fluid. These data should be obtained from laboratory measurements on rock samples and reservoir fluids.

The following example demonstrates typical relations among rock seismic properties and pore pressure and pore fluid type for a poorly-consolidated reservoir rock. The measured dry compressional and shear wave velocities versus confining hydrostatic stress are given in Figure 3.1 for a sample from the Troll Field (ϕ =0.34). This sample exhibits an increase in V_P and V_S of approximately 20 percent when the confining pressure is increased from 5 MPa to 30 MPa.

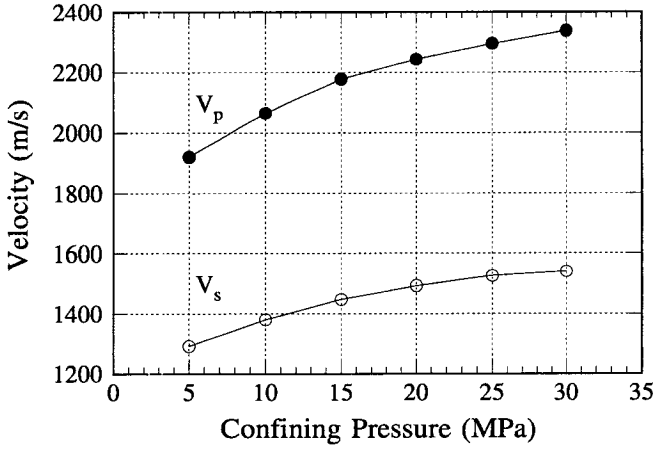

Figure 3.1: Compressional and shear wave velocities in dry Troll sands (measurements by Blangy, 1992).

Consider now the same sand buried at some constant overburden pressure. Experimental observations indicate that in many rocks, elastic properties depend on the effective, or differential, pressure, that is the difference between the overburden and pore pressure:

$$P_{effective} = P_{overburden} - P_{pore} \,, \tag{3.1}$$

and

$$\begin{aligned} V_P &= V_P(P_{effective}) \,, \\ V_S &= V_S(P_{effective}) \,. \end{aligned} \tag{3.2}$$

Therefore, we can transform the previous graph to approximate seismic velocities versus pore pressure in gas-saturated sand (Figure 3.2). Note that this is an approximation because "dry" measurements are not necessarily equivalent to gas-saturated. Many laboratory measurements of dry rock velocities, like the ones shown in Figure 3.1, are made at pore pressure equal to atmospheric pressure. The confining pressure, then, is the variable that is changed between velocity measurements. The pore fluid for these dry measurements is air at the laboratory temperature and pressure. At reservoir conditions, the compressibility of hydrocarbon gas can vary appreciably from that of air at laboratory conditions.

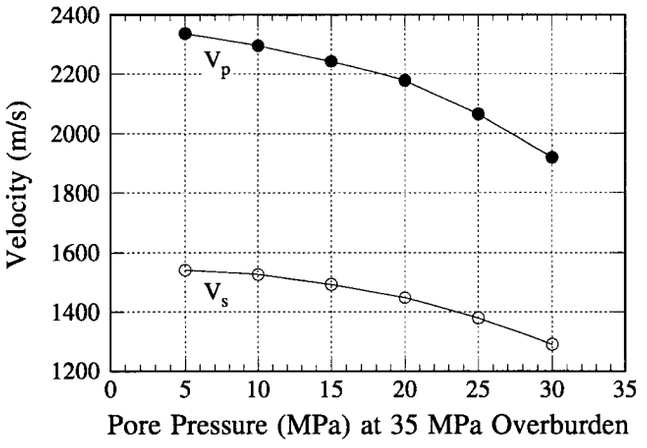

Figure 3.2: Compressional and shear wave velocities in dry Troll sands versus pore pressure at 35 MPa overburden.

The next step, then, will be to use Gassmann's formula (see Section 3.5.1) to transform the dry velocities into the velocities expected in saturated sand. The principle of fluid substitution, illustrated in Figure 3.3, can be used to predict the expected compressional

wave velocity changes associated with various recovery processes. These predictions can then be used as the basis for seismic forward modeling. In many cases, forward seismic modeling of recovery processes can be used to study the feasibility of recovery monitoring in a given setting and to optimize the acquisition geometry for recovery monitoring.

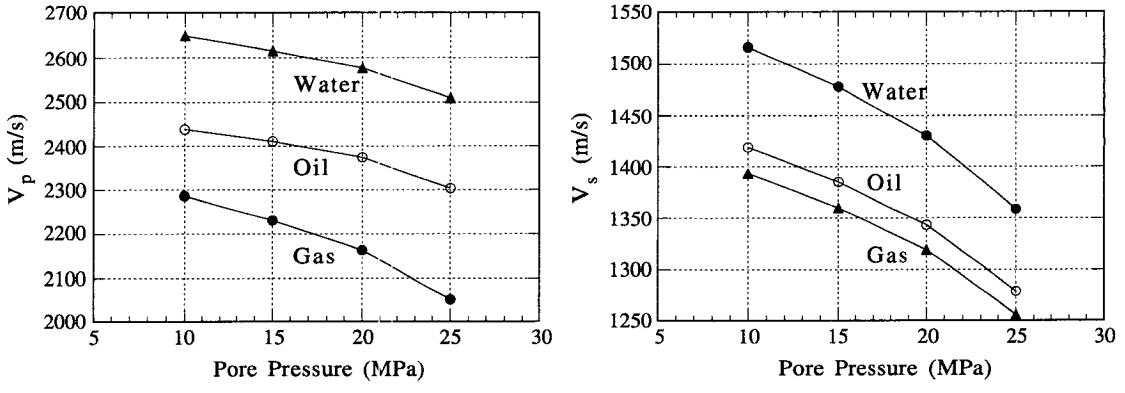

Figure 3.3: Compressional and shear wave velocities in Ottawa sand with gas, oil, and water. Calculated from the dry data by using Gassmann's formula.

Surveying a reservoir repeatedly during hydrocarbon recovery is the key to monitoring the production. The principal advantage of repeated surveys is that differences of fluid location, saturation, and temperature can be separated from a noisy geological background. In other words, monitoring a reservoir may be easier than its characterization.

Here I report a feasibility study concerned with oil recovery monitoring in the Troll field. As a starting point I used a flow simulation provided by Norsk Hydro. Results from flow simulation showed a prominent gas cone developing during oil production. I used the geometry of this gas cone after 113 days of simulated production, and I calculated rock properties and mapped their seismic signatures and their differences before production (Base Survey) for 4 levels of gas saturation (S_g) in the gas cone (S_g =0.2, 0.4, 0.6, and 0.8). Rock properties were obtained from earlier Troll field studies performed at Stanford.

I consider two cases for fluid distribution: uniform and patchy. I used Gassmann's formula to transform the flow simulation maps of fluid saturation into velocity and impedance maps for the uniform fluid distribution case. I used Gassmann's formula along with Hill's relationship for a composite with uniform shear modulus to calculate velocities for patchy fluid distribution. Then I conducted normal-incidence (zero offset) seismic forward modeling to obtain the seismic signatures of the recovery process for each case. I also investigated

the horizontal resolution by laterally averaging the reservoir properties over a 50 m radius.

I demonstrate that it is possible to seismically see the recovery-associated changes in fluid location in the Troll reservoir. For uniform fluid distribution, the differences in seismic signatures were clear at all levels of gas saturation in the gas cone. In contrast to this, the seismic anomaly associated with $S_g = 0.2$ was obscured by noise in the data for patchy fluid distribution. The results after laterally averaging the reservoir properties were similar, but they were lower in amplitude and longer in lateral extent than the corresponding cases with non-smoothed reservoir properties.

3.3 Problem Description

The goal of this project is to demonstrate the feasibility of using repeated seismic surveys to detect oil production in the Troll field. Here, I describe the reservoir and its associated rock and fluid properties.

3.3.1 Description of the Field

The Troll field is a large oil and gas field located off the western coast of Norway. The field is divided up into several provinces, most of which are gas-producing. Commercial oil reserves were discovered in the Troll West Oil Province.

The oil column is located at a depth of approximately 1500 meters, and it varies in thickness from a few meters to more than 20 meters. Horizontal drilling technology makes it possible to commercially produce oil from this thin oil zone. The temperature in the reservoir is approximately uniform and constant at 60°C. The overburden pressure is approximately 34 MPa.

3.3.2 Rock Properties

Estimates of dry rock properties in the reservoir under investigation are based on the results reported by Blangy and Strandenes (1991) and Blangy (1992) – laboratory experiments on 38 core samples from the Troll field. The samples came from the productive Sognefjord sands that are loosely consolidated with porosities ranging from 0.23 to about 0.35. In

the samples, quartz is the dominant constituent, with volumetric content between 50% and 80%, feldspar content is almost constant at 20%, and mica volumetric content varies between 0% and 25%.

Ultrasonic compressional and shear wave velocities (V_P and V_S) were measured at varying differential hydrostatic stress – from 5 to 30 MPa. In the reservoir under investigation, overburden is approximately 34 MPa and pore pressure varies close to 16 MPa with differential pressure around 18 MPa. Thus I have chosen to rely on the data set obtained at differential pressure 20 MPa. The measured ultrasonic V_P and V_S versus porosity are given in Figure 3.4.

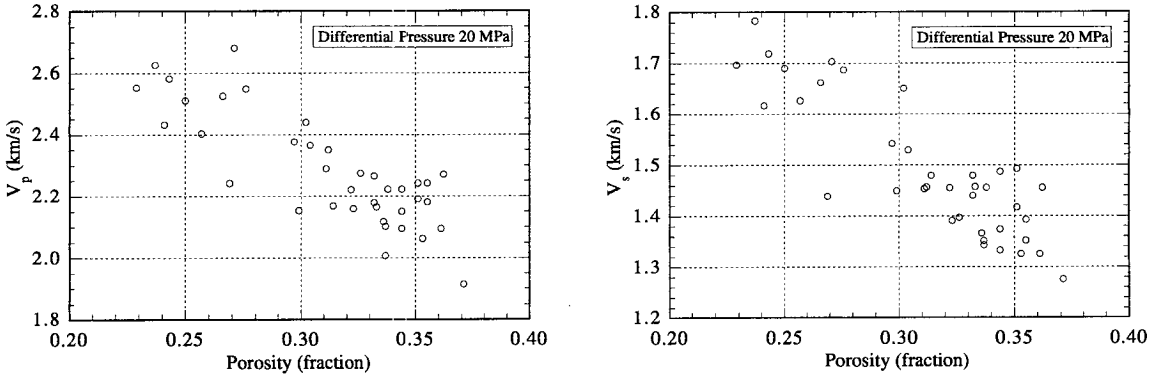

Figure 3.4: V_P (left) and V_S (right) versus porosity at 20 MPa differential pressure.

Based on the velocity data, along with densities calculated from mineralogy and porosity, the dry bulk (K_{Dry}) and shear (μ_{Dry}) moduli of the samples can be computed as:

$$K_{Dry} = \rho\left(V_P^2 - \frac{4}{3}V_S^2\right), \tag{3.3}$$

$$\mu_{Dry} = \rho V_S^2, \tag{3.4}$$

where ρ is dry density. The results of these calculations are given in Figure 3.5.

Linear least-squares fits obtained from these data are:

$$\begin{aligned} K_{Dry} &= 9.3 - 16.5\phi, \\ \mu_{Dry} &= 11.1 - 22.5\phi, \end{aligned} \tag{3.5}$$

where ϕ is porosity.

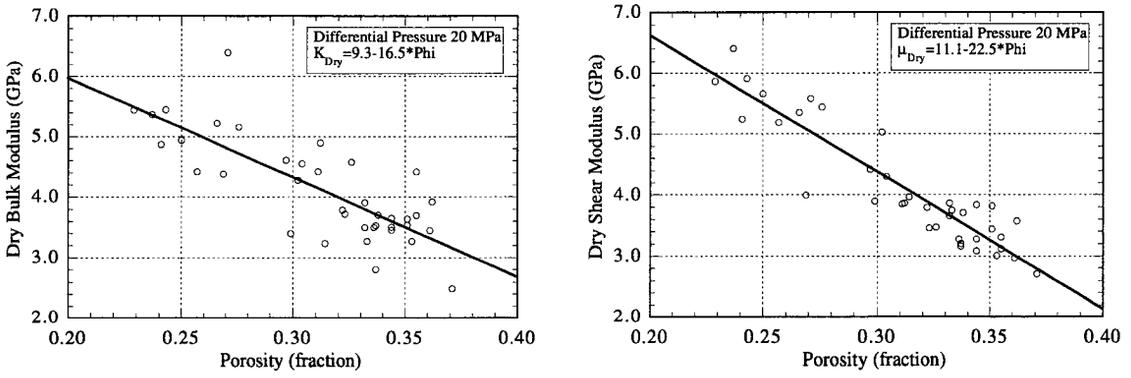

Figure 3.5: Dry bulk modulus (left) and shear modulus (right) versus porosity in the Troll samples. Straight lines give the linear least-squares fit.

3.3.3 Fluid Properties

Three fluid phases are simultaneously present in the reservoir under investigation: oil, water, and gas. The Troll West oil has a low gas-to-oil ratios (about 60). Typical values for the oil at reservoir conditions are: density 800 g/cm^3, bulk modulus 1020 MPa, viscosity 1.5 - 2.0 cp. I assume the following typical values for the reservoir water: density 1000 g/cm^3 and bulk modulus 2250 MPa.

I calculated gas properties by using the following formulas given by Batzle and Wang (1992), and assuming that the reservoir gas is methane with specific gravity 0.55 (the ratio of the gas density to air density at 15.6°C and atmospheric pressure). Pseudoreduced pressure and temperature are related to reservoir pore pressure and temperature as:

$$\begin{aligned} P_{pr} &= \frac{P}{4.892-0.4048G}, \\ T_{pr} &= \frac{T_a}{94.72+170.75G}, \end{aligned} \tag{3.6}$$

where G is gas specific gravity, and T_a is absolute temperature – ($T_a = t^\circ$ C $+273$), and pressure is in MPa. Gas density is

$$\rho_{gas} \cong \frac{28.8GP}{ZRT_a}, \tag{3.7}$$

where

$$\begin{aligned} Z &= [0.03+0.00527(3.5-T_{pr})^3]P_{pr} \\ &\quad +(0.642T_{pr}-0.007T_{pr}^4-0.52)+E, \end{aligned} \tag{3.8}$$

and

$$E = 0.109(3.85 - T_{pr})^2 \exp\{-[0.45 + 8(0.56 - 1/T_{pr})^2]P_{pr}^{1.2}/T_{pr}\}\,, \tag{3.9}$$

and R =8.31 is the universal gas constant.

The adiabatic gas bulk modulus K_s is:

$$K_s \cong \frac{P}{(1 - \frac{P_{pr}}{Z}\frac{\partial Z}{\partial P_{pr}})_{T=const}}\gamma_0\,, \tag{3.10}$$

where

$$\gamma_0 = 0.85 + \frac{5.6}{(P_{pr}+2)} + \frac{27.1}{(P_{pr}+3.5)^2} - 8.7\exp[-0.65(P_{pr}+1)]\,, \tag{3.11}$$

and $(\partial Z/\partial P_{pr})_{T=const}$ can be calculated from Equation 3.9.

3.3.4 Recovery Process and Simulation

A production well has been drilled in the region of this study. This well is horizontal within the oil zone. Norsk Hydro provided a simulation of primary oil production from this well. The duration of the simulation was 113 days, and results showed gas coning at the top and water coning at the base of the oil zone. Given the data from the simulation, the task was to determine if the changes in the reservoir during this period of production could be seen through seismic monitoring. Using both uniform and patchy fluid distribution models, I consider initial reservoir conditions and 4 levels of gas saturation in the gas cone. For each case, I create maps of seismic properties of the reservoir and their seismic images.

3.4 Recovery Monitoring: Input Data

The approach to hydrocarbon recovery monitoring developed by the Stanford Rock Physics Laboratory for this project includes three main parts: (1) reservoir flow simulation, (2) transforming the simulation results into seismic velocity and impedance maps using rock physics, and (3) conducting seismic forward modeling and imaging. In this section I describe the flow simulation data that was used to create velocity and impedance maps. Other

input parameters needed to transform the flow simulation data into velocity and impedance maps are: (1) porosity, (2) pore pressure, (3) saturation, and (4) mineral properties.

The properties of the solid phase (mineral properties) were calculated as average values from the data presented by Blangy (1992). The average bulk modulus and density of 38 samples are: $K_o = 47.1$ GPa, $\rho_{solid} = 2.642$ g/cm^3.

In this project, I calculated rock properties and mapped their seismic signatures before the production (base survey) and for 4 levels of gas saturation in the gas cone (monitor surveys), including both uniform and patchy gas distribution. Accordingly I provide all the appropriate data for these cases, plus the calculated differences between the monitor surveys and base survey. Porosity, pore pressure, and saturation mapped from the modified simulation data are given below.

3.4.1 Transforming the Original Grid into Reservoir Geometry

The portion of the reservoir simulation grid used in this study consisted of 312 individual blocks, each with a value of porosity, pore pressure, gas saturation, oil saturation, and water saturation. The simulation grid had 24 rows, corresponding to vertical position, and 13 columns, corresponding to horizontal position. The coordinates of the corners of each grid block were provided, and this information was used to construct Figures 3.6 and 3.7. Figure 3.7 is an expanded view of the densely-gridded section (labeled A) of Figure 3.6. The top of the reservoir is first encountered at a depth of 1510 m. It rises to 1507 m from horizontal positions of 750 m to 1350 m, then plunges to 1557.2 m at a horizontal position of 2600 m. The grid blocks vary in length from 25 to 500 m and in thickness from 1 m to more than 300 m.

The input porosity, pore pressure and saturation data at the beginning and end of simulation were extracted from the files provided by Norsk Hydro. I then extracted the geometry of the gas cone from these original data by selecting the region where gas saturation changed by more than 40 percent of the pore space between the beginning and end of simulated production. To illustrate the changes in the reservoir during the simulation and to reveal the gas cone geometry in grid space, Figure 3.8 shows the difference in oil saturation between 113 days and the start production. This image reveals gas coning at the top of the

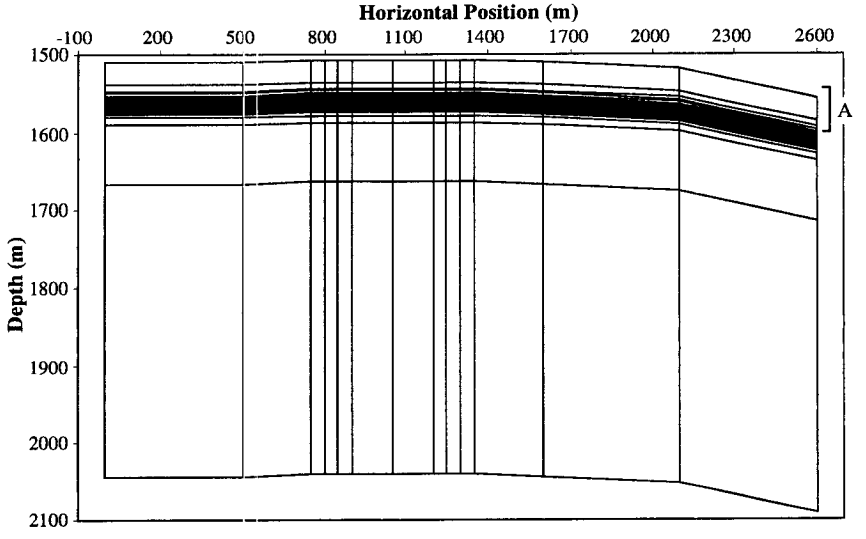

Figure 3.6: Reservoir grid in physical space.

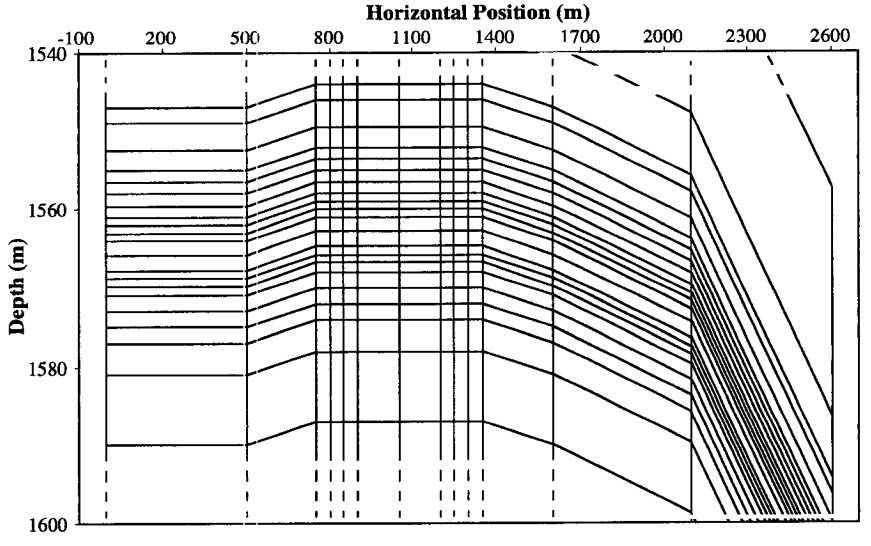

Figure 3.7: Expanded section A of reservoir grid.

oil zone and water coning at the base of the oil zone. Note that there are lateral discontinuities seen in adjacent grid blocks, especially in columns 12 and 13 of the grid. I consider this to be an artifact of simulation. These original discontinuities explain those present in the figures representing the characteristics of the recovery process in physical space shown in following sections.

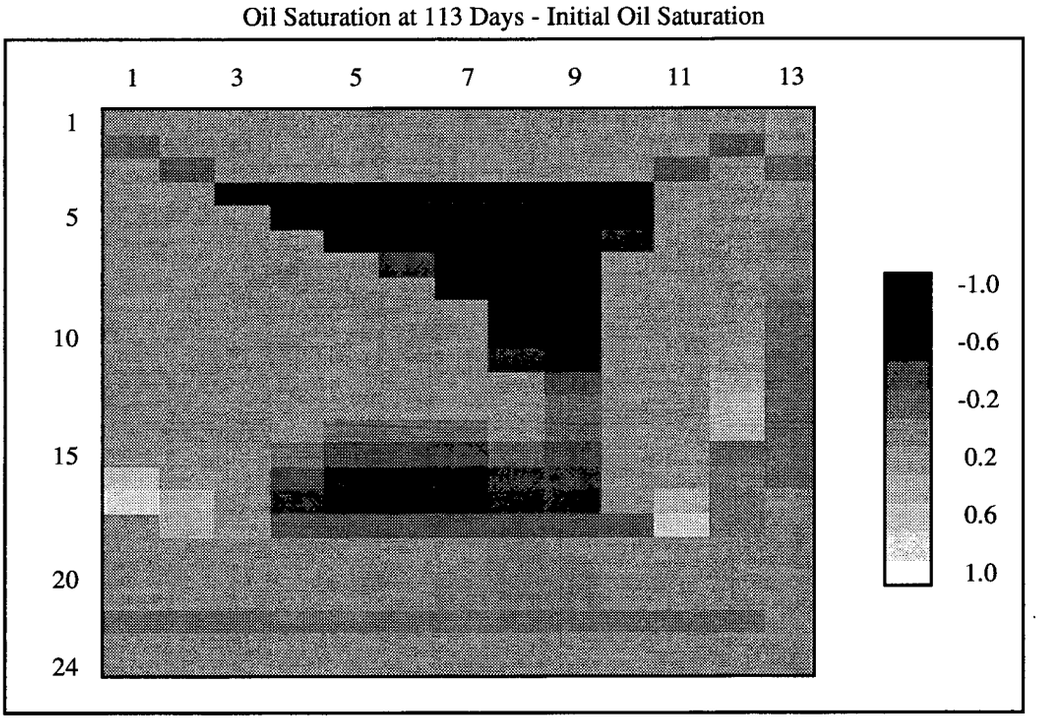

Figure 3.8: Change in oil saturation in the original grid space.

3.4.2 Distribution of Porosity

The map of porosity in the reservoir between depths 1500 m and 1700 m, and horizontal coordinates 0 m and 2600 m is given in Figure 3.9. Note that the well is located between 800 m and 1300 m (horizontal coordinate). Values of porosity were set equal in each row of the simulation grid, so each layer in the reservoir (simulation) has a constant porosity.

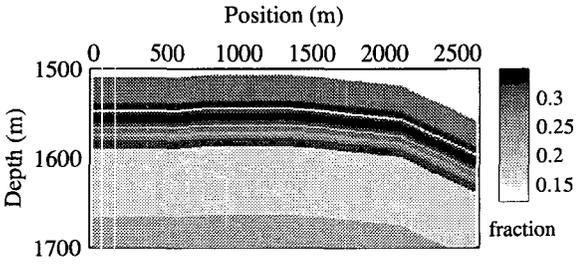

Figure 3.9: Porosity distribution in the reservoir.

3.4.3 Distribution of Pore Pressure

For this project, I assume the pore pressure for each level of gas saturation is equal to the pore pressure at the end of the simulation. The maximum decrease in pore pressure was 0.22 MPa. Maps of pore pressure in the reservoir (between depths 1500 m and 1700 m, and horizontal coordinates 0 m and 2600 m) for the Base Survey, and Monitor Surveys, as well as the difference, are given in Figures 3.10-3.11.

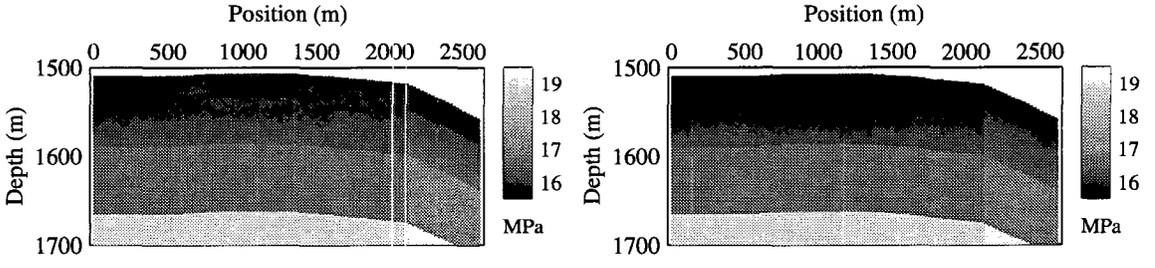

Figure 3.10: Pore pressure (MPa), Base Survey (left) and Monitor Surveys (right).

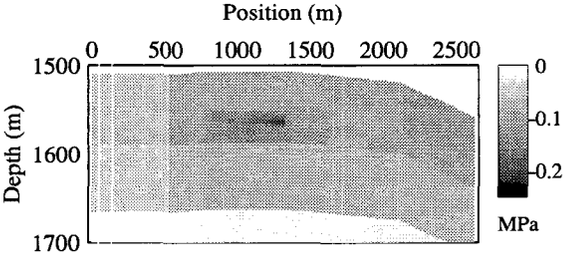

Figure 3.11: Change in pore pressure (MPa), Monitor - Base Survey.

3.4.4 Distribution of Saturation

Oil, gas, and water saturations and the differences are given in Figures 3.12- 3.20. For the monitor surveys, I extracted the geometry of the gas cone from the reservoir simulation, and I set the gas saturation in the gas cone to 4 values: S_g =0.2, 0.4, 0.6, and 0.8. I used the water saturation at the end of simulation in all cases of the monitor surveys.

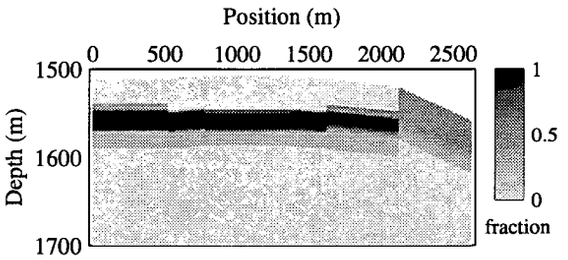

Figure 3.12: Oil saturation, Base Survey.

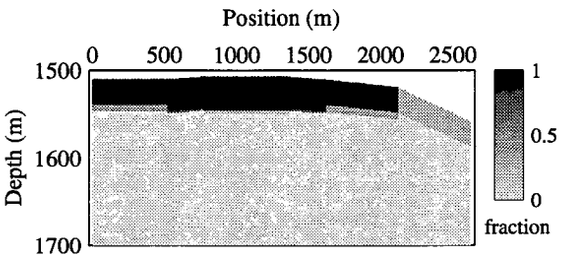

Figure 3.13: Gas saturation, Base Survey.

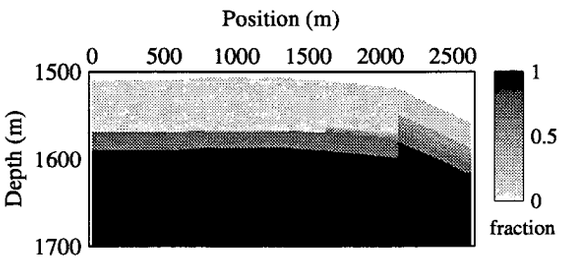

Figure 3.14: Water saturation, Base Survey.

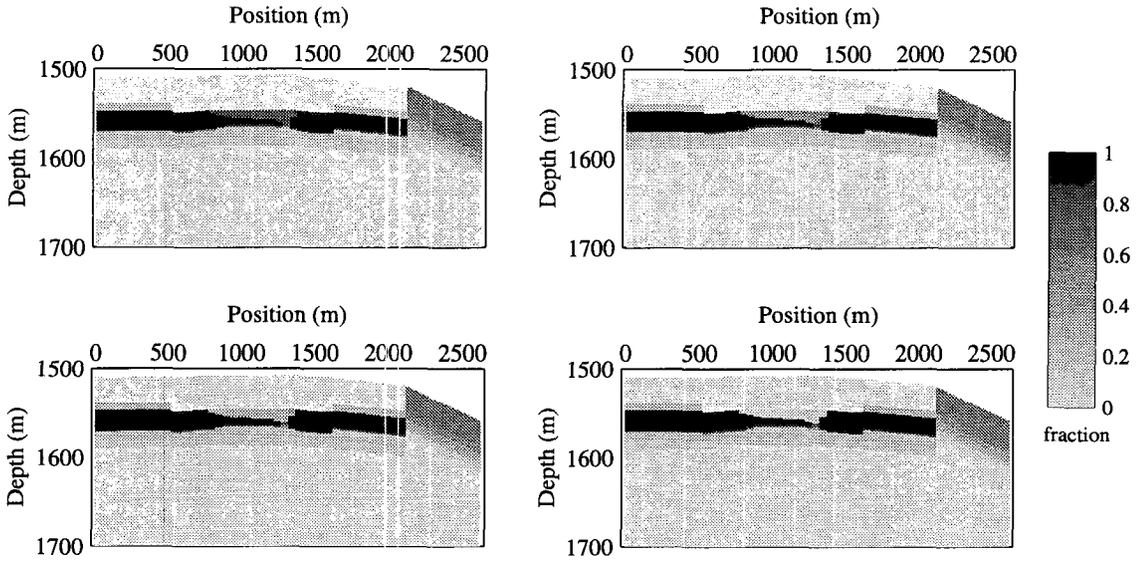

Figure 3.15: Oil saturation, Monitor Surveys. Each plot show the oil saturation for each level of S_g in the gas cone. S_g in the gas cone for these plots are 0.2 (upper left), 0.4 (upper right), 0.6 (lower left), and 0.8 (lower right).

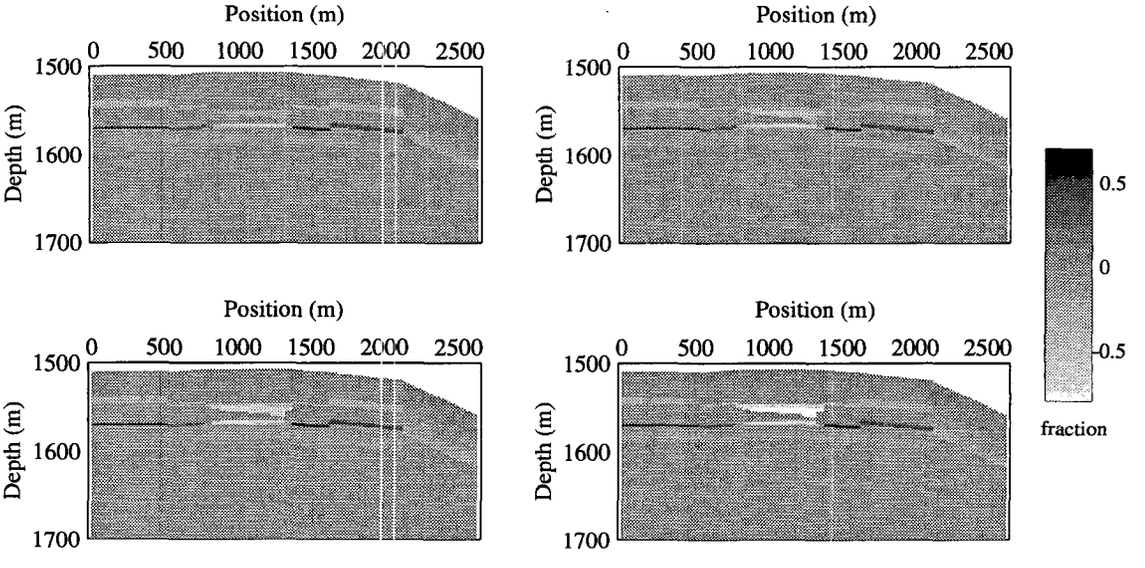

Figure 3.16: Changes in oil saturation for 4 cases. Each plot show the base oil saturation subtracted from the oil saturation for each level of S_g in the gas cone. S_g in the gas cone for these plots are 0.2 (upper left), 0.4 (upper right), 0.6 (lower left), and 0.8 (lower right).

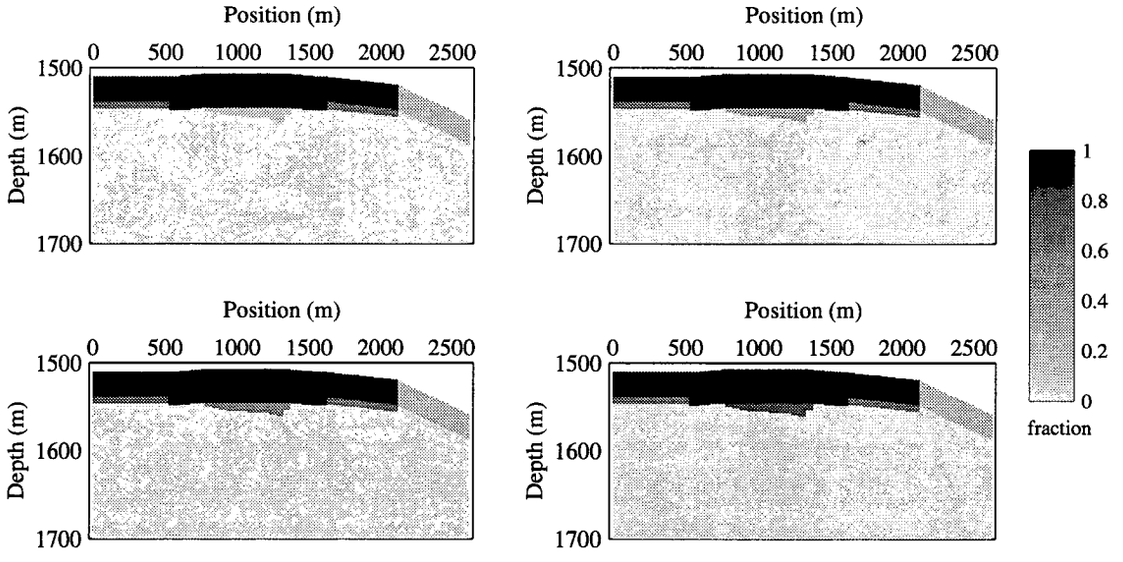

Figure 3.17: Gas saturation, Monitor Surveys. S_g in the gas cone for these plots are 0.2 (upper left), 0.4 (upper right), 0.6 (lower left), and 0.8 (lower right).

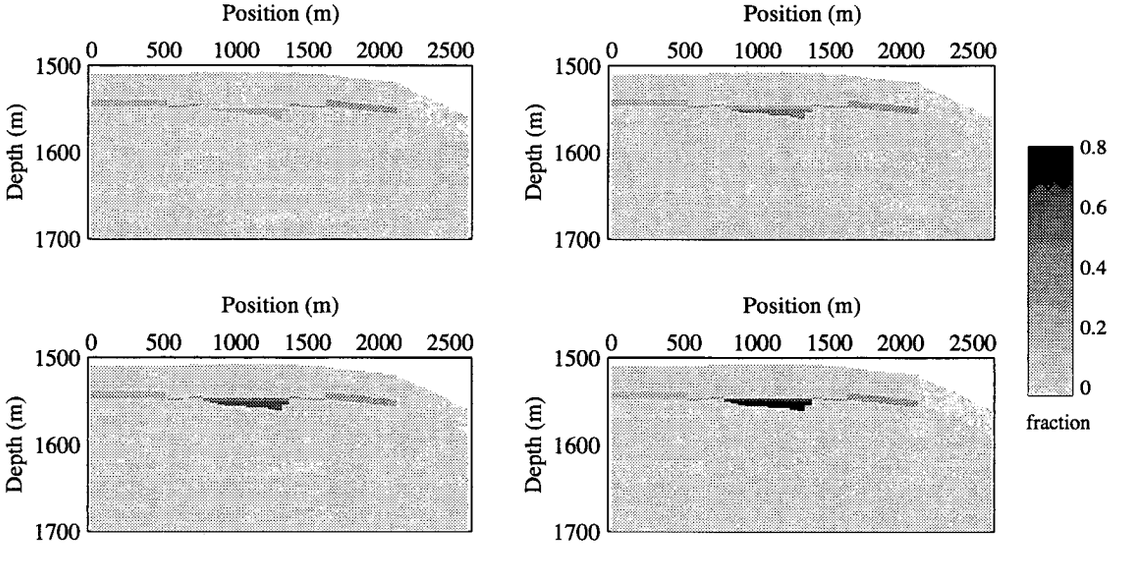

Figure 3.18: Changes in gas saturation for 4 cases. Each plot show the base gas saturation subtracted from the gas saturation for each level of S_g in the gas cone. S_g in the gas cone for these plots are 0.2 (upper left), 0.4 (upper right), 0.6 (lower left), and 0.8 (lower right).

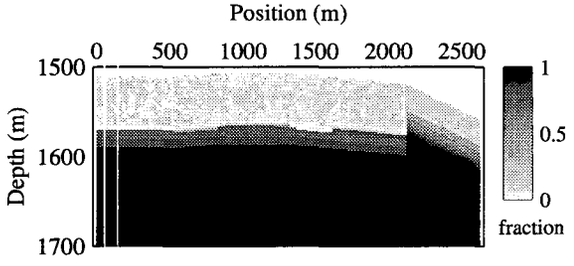

Figure 3.19: Water saturation, Monitor Surveys. The water saturation was kept the same in each monitor survey.

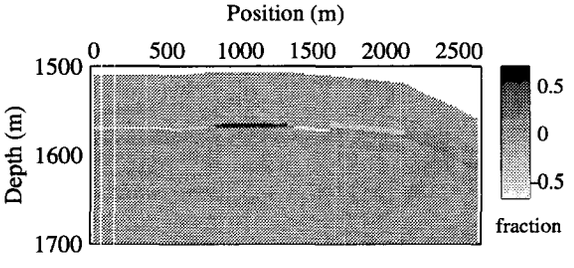

Figure 3.20: Change in water saturation.

3.5 Recovery Monitoring: Rock Physics Transformations

I consider two types of fluid distribution for recovery monitoring: uniform and patchy. This section briefly describes the rock physics transformations associated with each. For a more detailed description of the models, see Section 2.4.

3.5.1 Uniform Fluid Distribution: Gassmann's Formula

For the case of uniform fluid distribution, increments in pore pressure induced by seismic wave propagation diffuse so that pore pressure equilibrates during a seismic period. The effect of saturation, then, can be calculated by using Gassmann's (1951) formula. This formula relates the effective elastic moduli of a dry rock to the effective moduli of the same rock containing fluid:

$$\frac{K_{Sat}}{K_o - K_{Sat}} = \frac{K_{Dry}}{K_o - K_{Dry}} + \frac{K_{fluid}}{\phi(K_o - K_{fluid})}, \tag{3.12}$$

$$\mu_{Sat} = \mu_{Dry}, \tag{3.13}$$

where K_{Dry} is effective bulk modulus of dry rock, K_{Sat} is effective bulk modulus of the rock with pore fluid, K_o is bulk modulus of mineral material making up rock, K_{fluid} is effective bulk modulus of pore fluid, ϕ is porosity, μ_{Dry} is effective shear modulus of dry rock, and μ_{Sat} is effective shear modulus of rock with pore fluid.

We can derive from Gassmann's formula:

$$K_{Sat} = K_{Dry}\frac{\phi K_o - (1+\phi)K_{fluid} + K_{fluid}K_o/K_{Dry}}{\phi K_o + (1-\phi)K_{fluid} - K_{fluid}K_{Dry}/K_o}, \tag{3.14}$$

and use this last expression to compute the bulk modulus of saturated rock from dry data.

For partially saturated rocks at sufficiently low frequencies, one can use an effective modulus for the pore fluid that is an isostress average of the moduli of the fluid phases, as given by Reuss (1929). In general, if pore fluid includes more than two phases, the following formula can be used to calculate the mixture's effective bulk modulus:

$$\frac{1}{K_{fluid}} = \sum_{i=1}^{n} \frac{f_i}{K_i}, \tag{3.15}$$

where n is the number of components, f_i is the volumetric fraction of the i^{th} component, and K_i is its bulk modulus.

Finally, I use the following formulas to find seismic velocities in saturated rock:

$$V_{P_{sat}} = \sqrt{\frac{\left(K_{Sat} + \frac{4}{3}\mu_{Sat}\right)}{\rho_{Sat}}}, \tag{3.16}$$

$$V_{S_{sat}} = \sqrt{\frac{\mu_{Sat}}{\rho_{Sat}}}, \tag{3.17}$$

where ρ_{sat} is the density of saturated rock, given by:

$$\rho_{Sat} = (1-\phi)\rho_{solid} + \phi\rho_{fluid}, \tag{3.18}$$

and ϕ is porosity, ρ_{solid} is the density of the solid phase, and ρ_{fluid} is the density of the fluid. The latter can be found from the densities of its components ρ_i as:

$$\rho_{fluid} = \sum_{i=1}^{n} f_i\rho_i . \tag{3.19}$$

The above formulas allow us to calculate the needed fluid properties that will depend on saturation. These properties will depend on pressure and temperature as well because the bulk modulus and density of the reservoir fluids are affected by these two parameters. In this study, reservoir temperature was assumed constant, and changes in pore pressure were used to calculate gas properties only, as described in Section 3.3.3.

3.5.2 Patchy Fluid Distribution

Another model that could describe the pore fluid distribution is a patchy fluid model. In this case, pore fluids are not distributed uniformly, and increments pore pressure induced by seismic waves do not equilibrate. Within a single reservoir simulation block, it is reasonable to assume that heterogeneities in the rock could lead to heterogeneities in pore fluid distribution. How these heterogeneities affect seismic wave propagation depend on the dimensions of the patches, the pore fluid bulk modulus and viscosity, the permeability of the rock, and the seismic frequency. As discussed in the last chapter, the characteristic

length for patchy behavior can be calculated as:

$$l \approx \sqrt{\frac{\kappa K_f}{\eta f}} . \tag{3.20}$$

In the region of the gas cone, horizontal reservoir permeability ranges from 3.6-13.7 D, vertical permeability ranges from 0.5-2.1 D, the oil bulk modulus is 1020 MPa, and its viscosity is 2 cp. For a seismic frequency of 25 Hz, the characteristic patch length would range from 25-60 cm. Since the gas cone ranges in thickness from 1-15 m, the patchy fluid distribution model could be applicable here.

For this study, I have chosen to look at one realization of the patchy fluid model. Since the ratio of oil viscosity to water viscosity is small ($\leq$2), I assume that water displacing oil is uniform (van Meurs, 1957). However, for the case of gas displacing oil in the gas cone, I assume the result is patchy saturation. The water saturation in the gas cap and gas cone does not change during simulated production. It remains around 6 percent, which I consider to be irreducible water saturation. For the patchy model, I assume this water is in both oil and gas patches. Any amount of water above the irreducible saturation is divided between oil and gas patches in proportion to the amount of oil and gas in each reservoir simulation cell. I use Gassmann's relationships to calculate the bulk and shear moduli of the saturated rock in each patch (Equations 3.13-3.14). Also, I use Equation 3.15 to compute the bulk modulus of the pore fluid in the oil and gas patches. Then, I use the relationship given by Hill (1963) for a composite with a uniform shear modulus to compute the saturated bulk modulus of the simulation blocks with oil and gas patches:

$$\frac{1}{K_{eff} + \frac{4}{3}\mu_{Sat}} = \sum_{i=1}^{n} \frac{f_i}{K_{Sat_i} + \frac{4}{3}\mu_{Sat}} . \tag{3.21}$$

In the realization used here, there were only two types of patches: oil with water and gas with water. There are many other possible realizations to consider, such as including some gas in the oil patches.

3.5.3 Transformation Results

Having described the data inputs and the rock physics transformations, I now show the resulting velocity and impedance maps along with the changes in velocity and impedance.

Velocity and Impedance

The calculated initial P-wave velocity for the uniform and patchy fluid distribution cases are shown in Figure 3.21. Both cases exhibit layered velocities as expected. Figure 3.22 shows the calculated V_P for all 4 monitor surveys. Again, the difference in each case is the gas saturation in the gas cone, with values of S_g =0.2, 0.4, 0.6, and 0.8. Figure 3.23 shows the same 4 plots for patchy fluid distribution in the gas cone. The changes in velocity are significantly smaller for the patchy case compared to the uniform fluid case at $S_g = 0.2$ and $S_g = 0.4$. Figures 3.24-3.26 show the calculated compressional impedance ($I_P = \rho V_P$) for the uniform and patchy fluid cases.

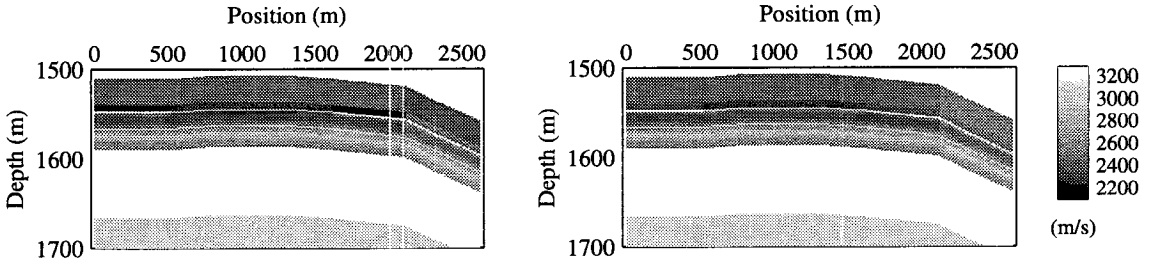

Figure 3.21: Initial V_P for uniform fluid distribution (left) and patchy fluid distribution (right).

Velocity and Impedance Differences

A convenient technique for displaying the changes in the reservoir during simulated production is to show the difference between the reservoir property at a given time and the initial values of that property. For example, to highlight areas of velocity change, I subtract the initial velocity field from the velocities calculated for each case of uniform saturation in the gas cone, shown in Figure 3.27. Likewise, Figure 3.28 shows the changes in V_P for each case of patchy saturation in the gas cone. The largest change in V_P in the gas cone occurs where $S_g = 0.2$ for the uniform fluid distribution, while the largest change in the patchy distribution is at $S_g = 0.8$.

Similarly, I show the differences in I_P for both the uniform and patchy fluid distribution. Here, the largest change in impedance occurs at $S_g = 0.8$ in the gas cone.

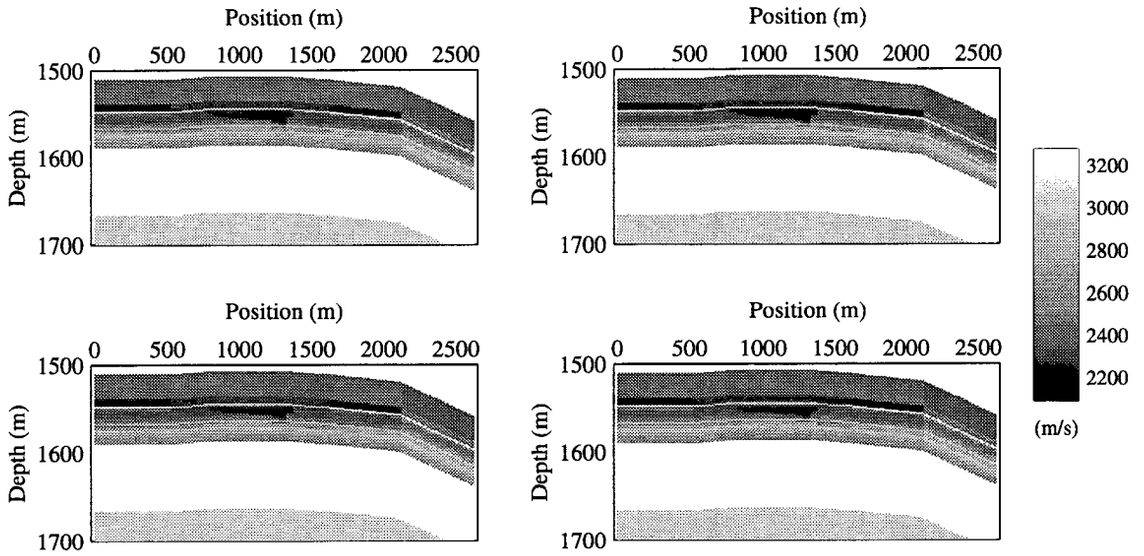

Figure 3.22: Calculated V_P for the uniform fluid distribution cases. Each plot show the velocity for each level of S_g in the gas cone. S_g in the gas cone for these plots are 0.2 (upper left), 0.4 (upper right), 0.6 (lower left), and 0.8 (lower right).

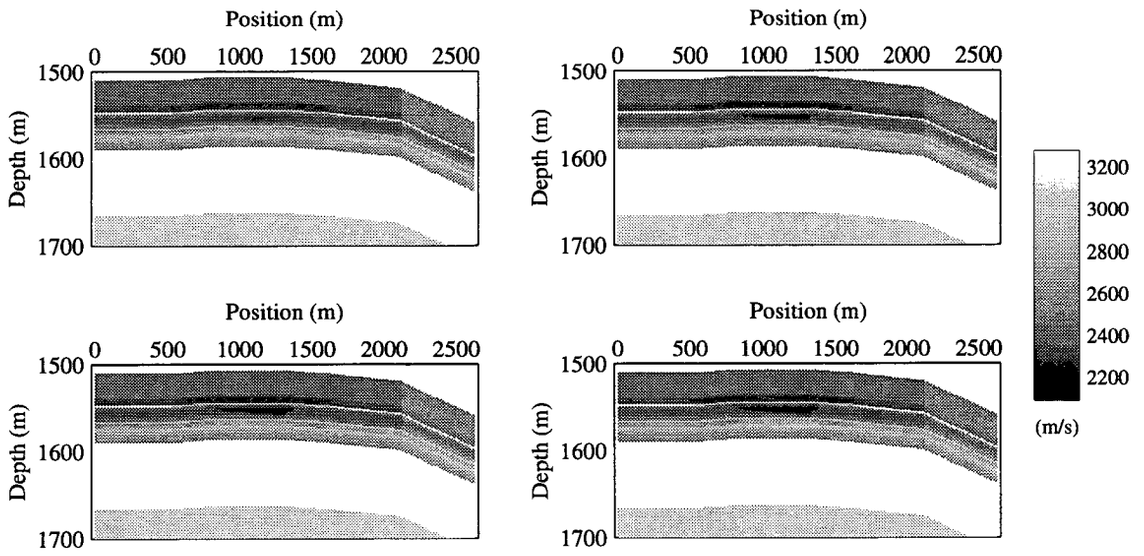

Figure 3.23: Calculated V_P for the patchy fluid distribution cases. Each plot show the velocity for each level of S_g in the gas cone. S_g in the gas cone for these plots are 0.2 (upper left), 0.4 (upper right), 0.6 (lower left), and 0.8 (lower right).

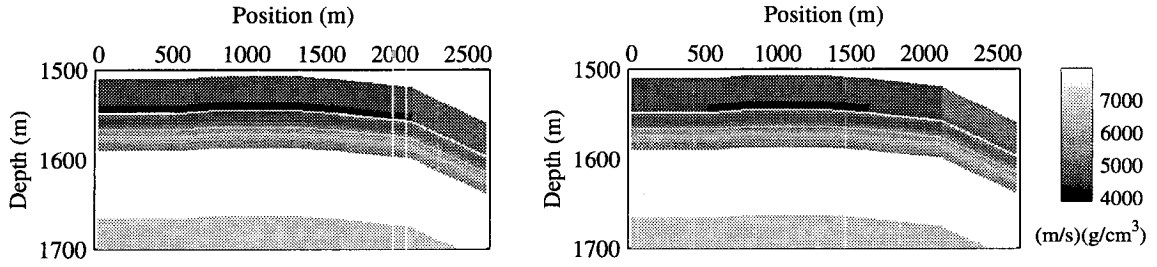

Figure 3.24: Initial I_P for uniform fluid distribution (left) and patchy fluid distribution (right).

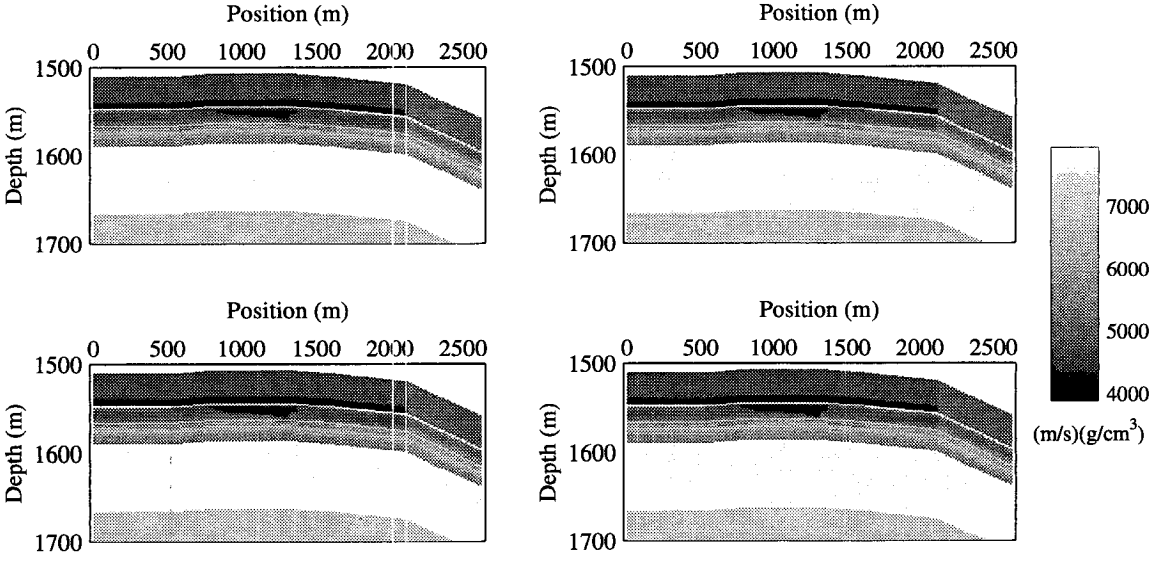

Figure 3.25: Calculated I_P for the uniform fluid distribution cases. Each plot show the impedance for each level of S_g in the gas cone. S_g in the gas cone for these plots are 0.2 (upper left), 0.4 (upper right), 0.6 (lower left), and 0.8 (lower right).

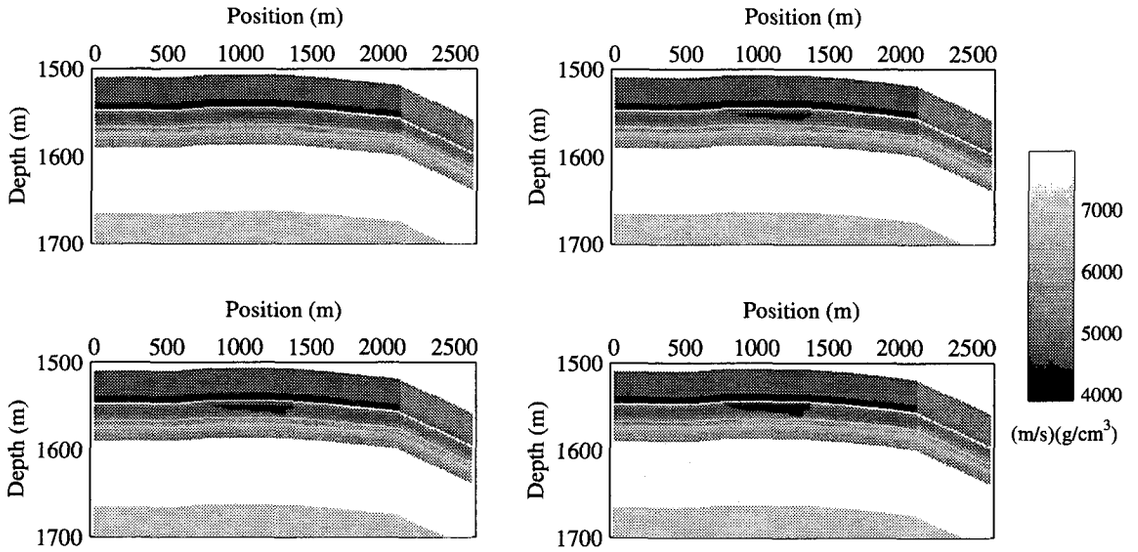

Figure 3.26: Calculated I_P for the patchy fluid distribution cases. Each plot show the impedance for each level of S_g in the gas cone. S_g in the gas cone for these plots are 0.2 (upper left), 0.4 (upper right), 0.6 (lower left), and 0.8 (lower right).

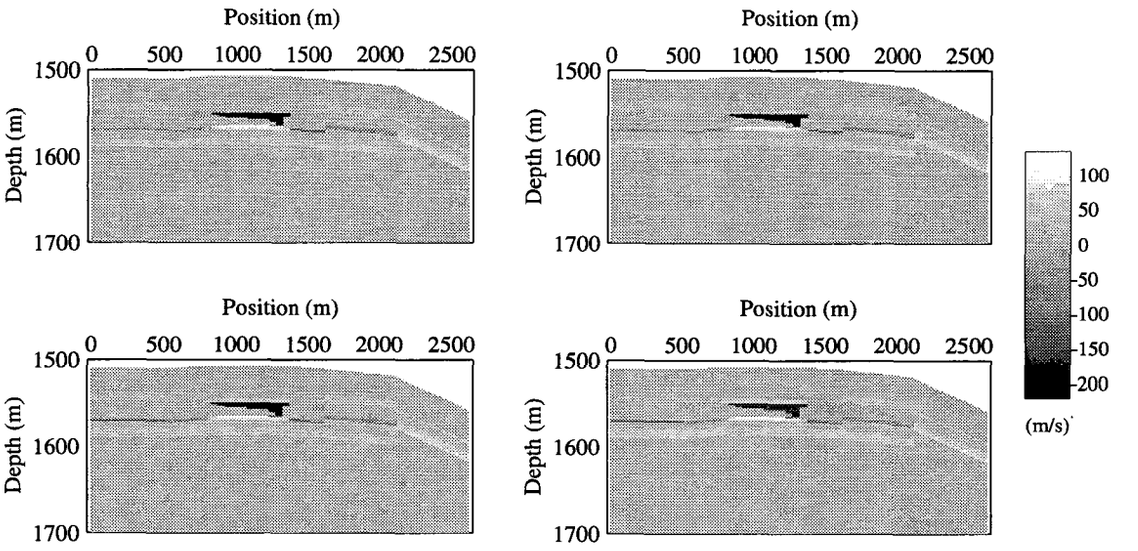

Figure 3.27: Difference in V_P for the uniform fluid distribution cases. Each plot show the base velocity subtracted from the velocity calculated for each level of S_g in the gas cone. S_g in the gas cone for these plots are 0.2 (upper left), 0.4 (upper right), 0.6 (lower left), and 0.8 (lower right).

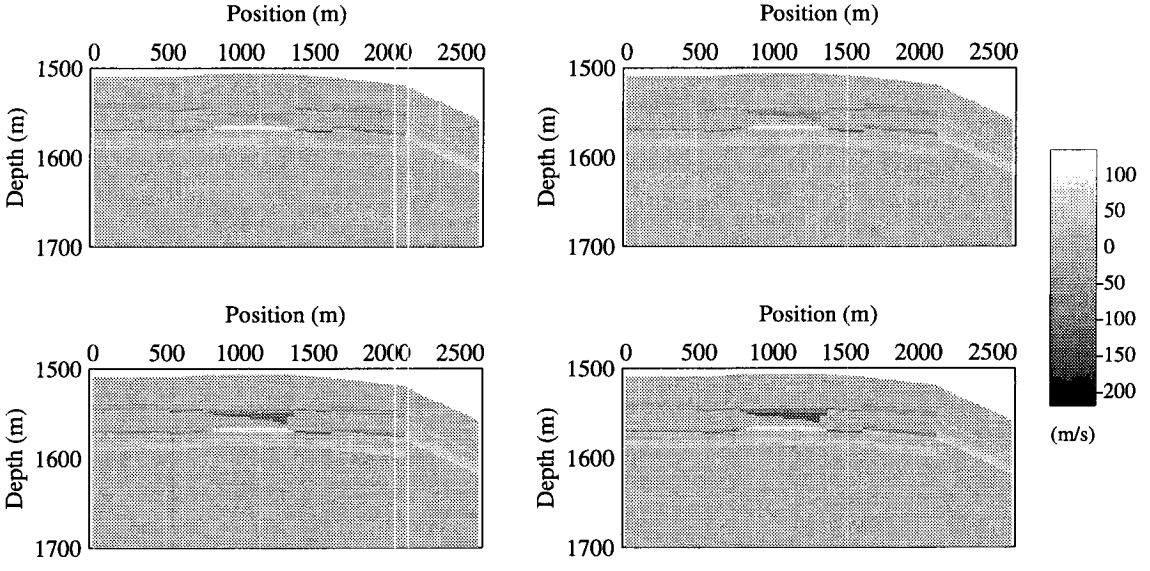

Figure 3.28: Difference in V_P for the patchy fluid distribution cases. Each plot show the base velocity subtracted from the velocity calculated for each level of S_g in the gas cone. S_g in the gas cone for these plots are 0.2 (upper left), 0.4 (upper right), 0.6 (lower left), and 0.8 (lower right).

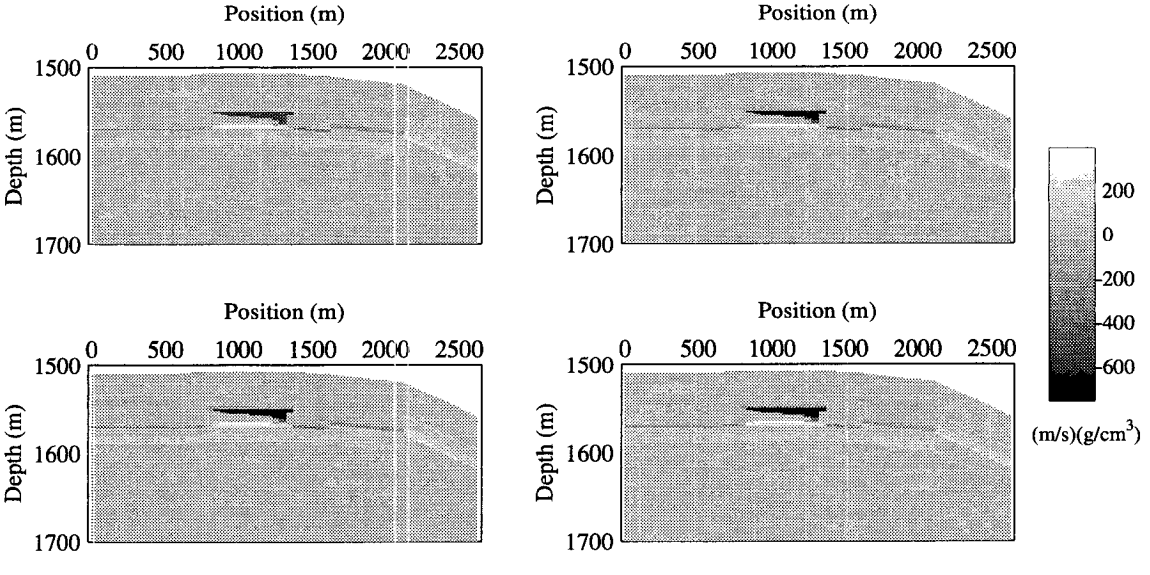

Figure 3.29: Difference in I_P for the uniform fluid distribution cases. Each plot show the base impedance subtracted from the impedance calculated for each level of S_g in the gas cone. S_g in the gas cone for these plots are 0.2 (upper left), 0.4 (upper right), 0.6 (lower left), and 0.8 (lower right).

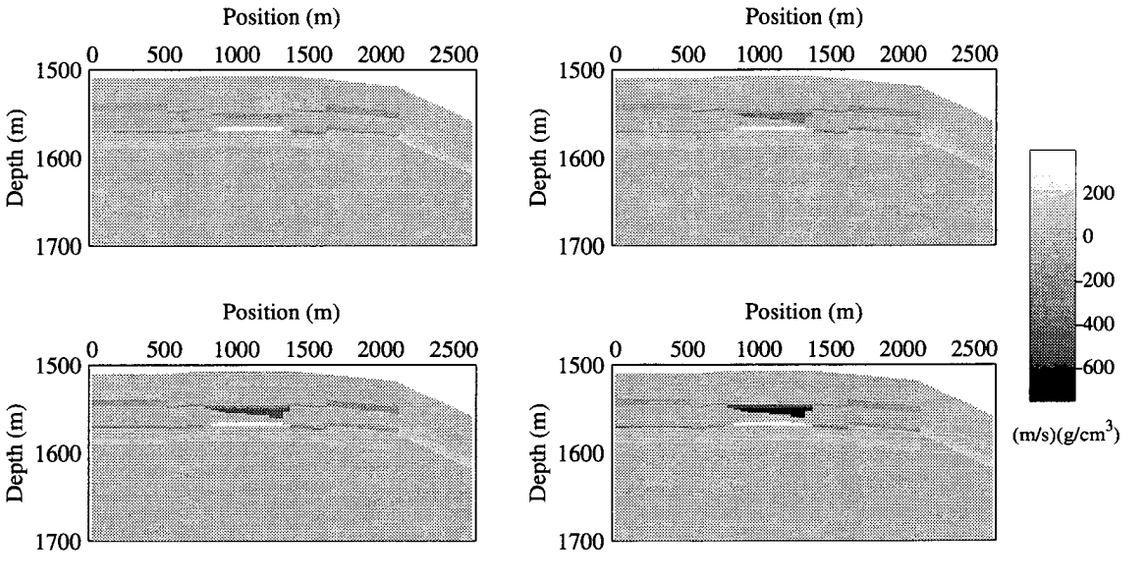

Figure 3.30: Difference in I_P for the patchy fluid distribution cases. Each plot show the base impedance subtracted from the impedance calculated for each level of S_g in the gas cone. S_g in the gas cone for these plots are 0.2 (upper left), 0.4 (upper right), 0.6 (lower left), and 0.8 (lower right).

3.6 Modeling Seismic Response

In this section, I describe the normal incidence method used to model the seismic response, and I show the changes in seismic response for variations in gas saturation for the uniform and patchy fluid distribution models.

3.6.1 The Seismic Model

I model the seismic response of the reservoir using normal incidence (zero offset) plane wave propagation. After calculating the velocities within the reservoir simulation grid, I took the vertical velocity and density profile at 50 m intervals across the reservoir. I assumed the velocity profile at each location represented the velocities of a horizontal, 1D layered medium at that location. I then used the velocity and density profiles as inputs for a Kennett (1983) algorithm for plane wave propagation at normal incidence. The main advantages to this technique are simplicity and speed. I modeled the seismic response at 50 m intervals across the reservoir to simulate a CDP stacked section. The Kennett algorithm

required an input wavelet, and I chose to use a 25 Hz minimum phase wavelet. After generating the seismic traces, I added random noise at a signal to noise ratio of 10:1. I chose this noise level to be similar to the noise level reported by Lumley et al. (1994).

3.6.2 Modeling Results

The resulting seismic images are shown in Figures 3.31-3.33. The base surveys for the uniform fluid and patchy fluid distribution cases are quite similar. However, the effect of the patchiness in the gas cone is quite evident when the gas saturation (S_g) is low. While the seismic anomaly is clearly seen for all cases of gas saturation for uniform fluid (Figure 3.32), the anomaly in the patchy fluid cases is comparatively weak (Figure 3.33), especially at $S_g = 0.2$ and 0.4 in the gas cone. To highlight the anomalies, I subtracted the base survey seismic images (Figures 3.31) from each seismic image representing the different level of S_g in the gas cone. These differences are shown in Figures 3.34-3.35.

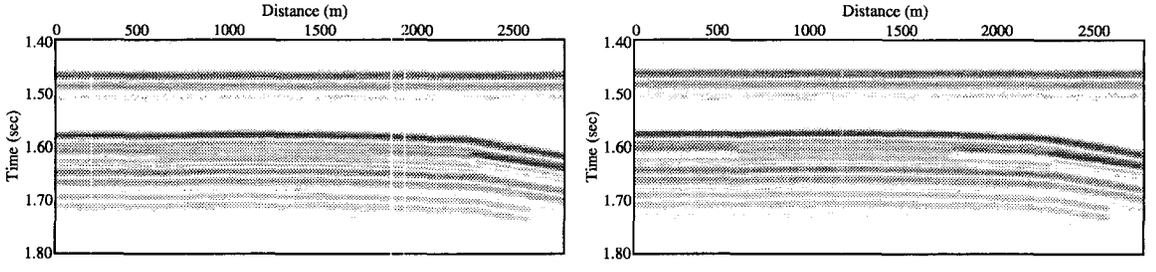

Figure 3.31: Baseline seismic images for uniform (left) and patchy (right) fluid distribution.

There are some notable differences in the seismic images for the uniform and patchy fluid distribution cases. For the uniform fluid case, the gas cone causes a strong anomaly at every level of gas saturation, and the amplitude of the anomaly grows with increasing S_g. For the patchy fluid case, there is a hint of an anomaly at S_g =0.2 on the seismic image (Figure 3.33), but noise obscures the anomaly in the seismic difference image (Figure 3.35). The amplitude of the anomaly also increases with increasing S_g, but it is never as large as the anomaly in the uniform fluid cases.

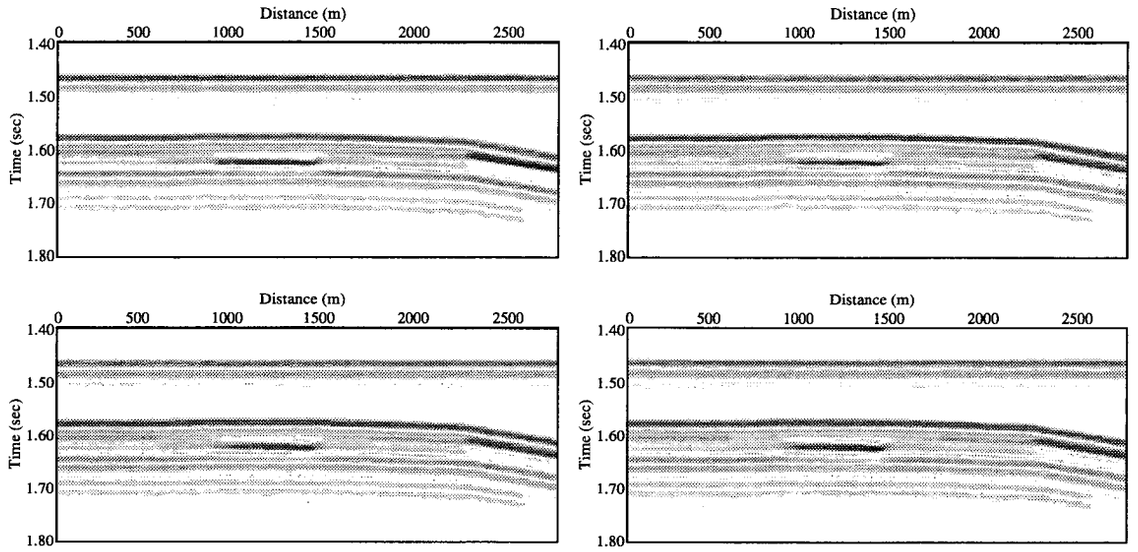

Figure 3.32: Seismic images for monitor surveys, each representing uniform fluid with different amounts of S_g in the gas cone. S_g in the gas cone for these plots are 0.2 (upper left), 0.4 (upper right), 0.6 (lower left), and 0.8 (lower right).

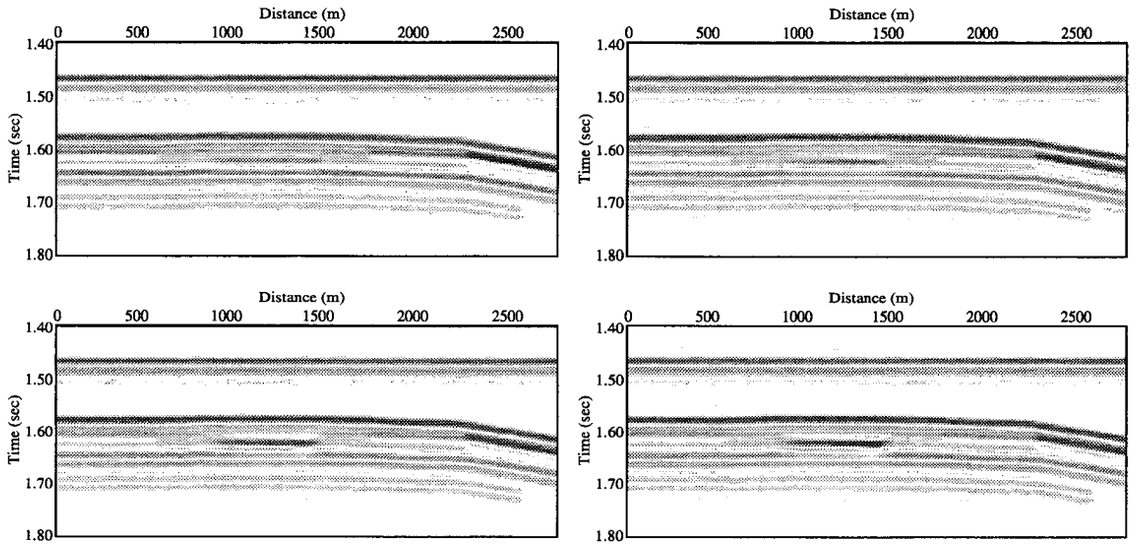

Figure 3.33: Seismic images for monitor surveys, each representing patchy fluid with different amounts of S_g in the gas cone. S_g in the gas cone for these plots are 0.2 (upper left), 0.4 (upper right), 0.6 (lower left), and 0.8 (lower right).

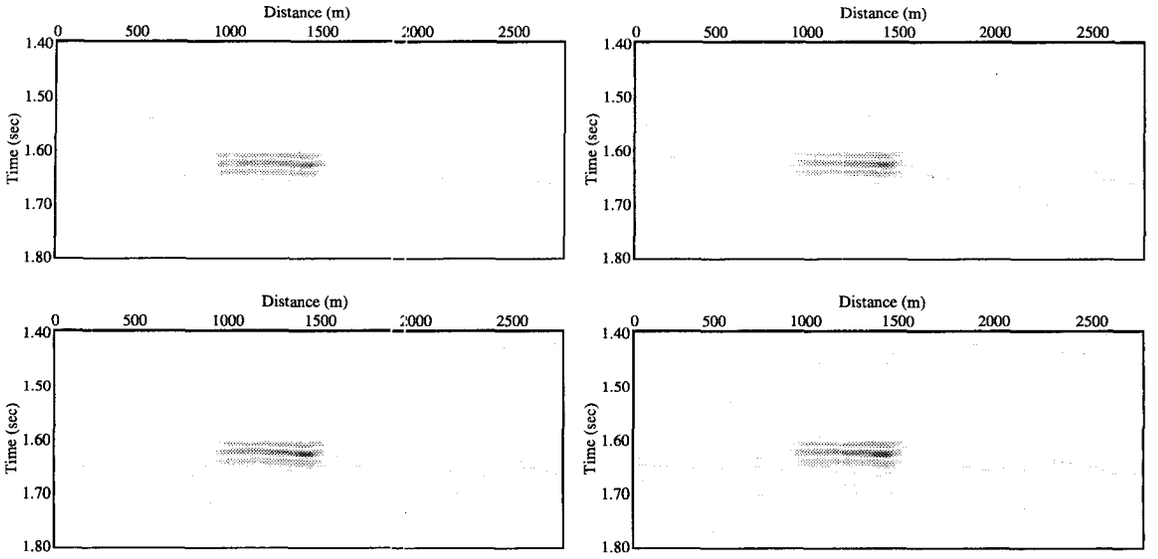

Figure 3.34: Difference in seismic images for uniform fluid distribution cases. Each plot show the base survey subtracted from the survey for each level of S_g in the gas cone. S_g in the gas cone for these plots are 0.2 (upper left), 0.4 (upper right), 0.6 (lower left), and 0.8 (lower right).

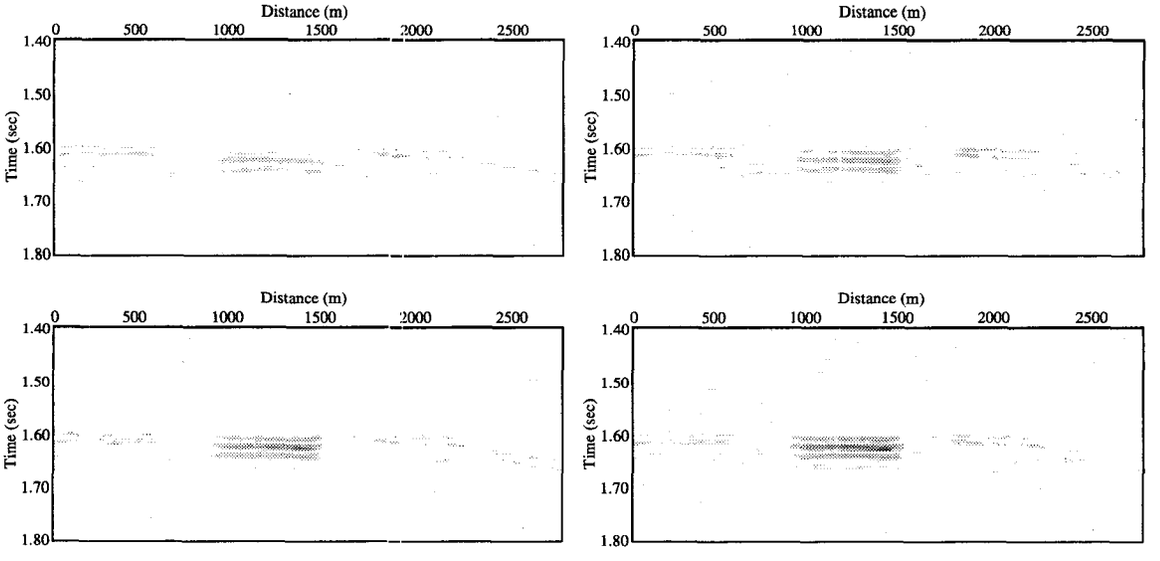

Figure 3.35: Difference in seismic images for patchy fluid distribution cases. Each plot show the base survey subtracted from the survey for each level of S_g in the gas cone. S_g in the gas cone for these plots are 0.2 (upper left), 0.4 (upper right), 0.6 (lower left), and 0.8 (lower right).

3.7 Effects of Lateral Resolution

The seismic model used for this study had perfect lateral resolution. However, there were lateral variations in the reservoir velocity model which would affect a propagating seismic wave. The seismic wave sees an average property at any one location. In the best case scenario, one might expect to reduce the lateral resolution to a radius of one quarter of a seismic wavelength (Lumley, 1995). With this in mind, I computed an arithmetic average of the velocity and density at a radius of 25 m at each depth. I chose to do the averaging and seismic modeling for uniform fluid and patchy fluid models in the case of 80 percent gas saturation in the gas cone.

3.7.1 Averaged Velocity and Impedance Fields

The velocity and impedance maps resulting from the lateral averaging are shown in Figures 3.36-3.38. Each plots compares the velocity field without lateral averaging to the field with averaging. As expected, this averaging smooths the velocity boundaries, effectively increasing the size and decreasing the amplitude of the velocity and impedance anomalies, as shown in the difference plots in Figures 3.39-3.42.

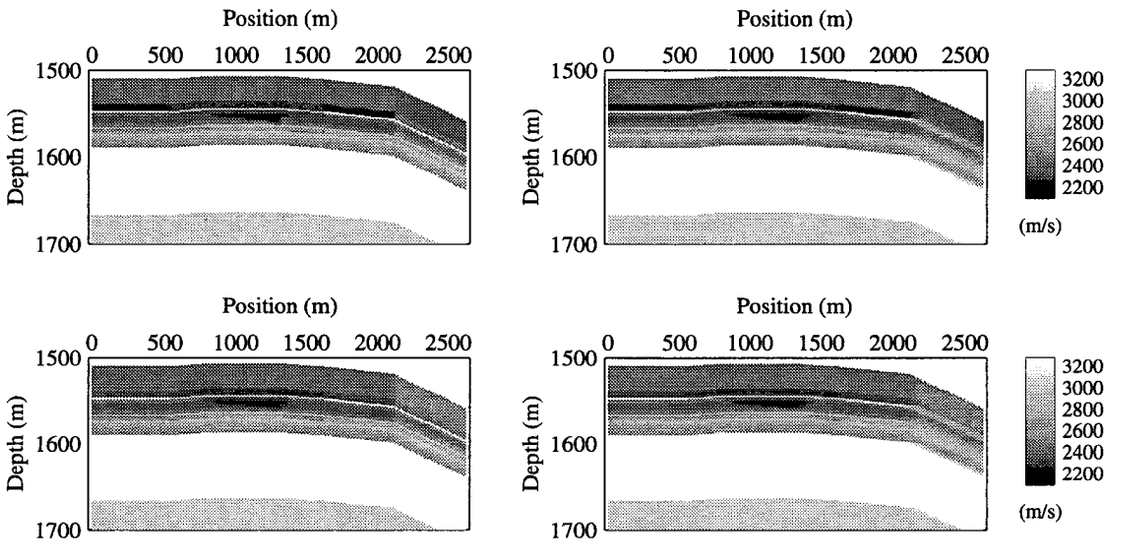

Figure 3.36: Comparison of original V_P (left) and laterally-averaged V_P (right) fields for $S_g = 0.8$ in the gas cone. The top two images are for uniform fluid distribution and the bottom two images are for patchy distribution.

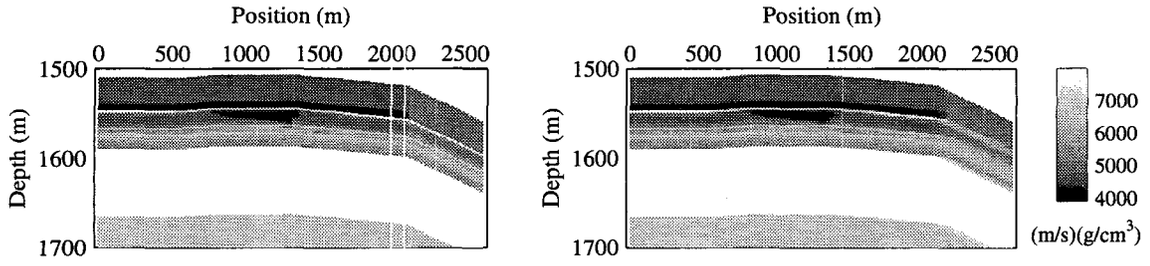

Figure 3.37: Original I_P (left) and laterally-averaged I_P (right) for uniform fluid distribution and $S_g = 0.8$ in the gas cone.

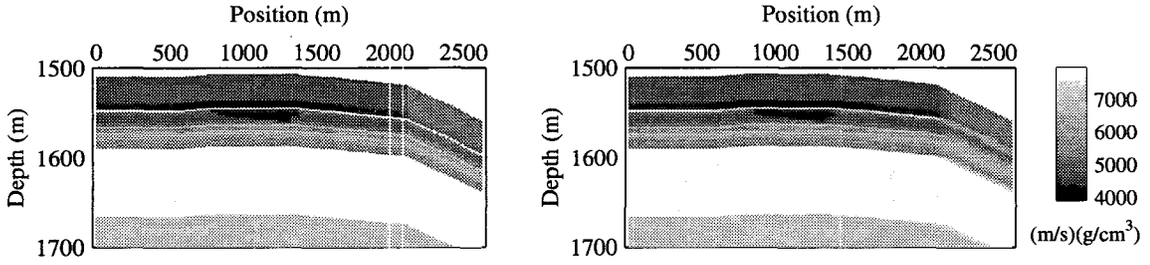

Figure 3.38: Original I_P (left) and laterally-averaged I_P (right) for patchy fluid distribution and $S_g = 0.8$ in the gas cone.

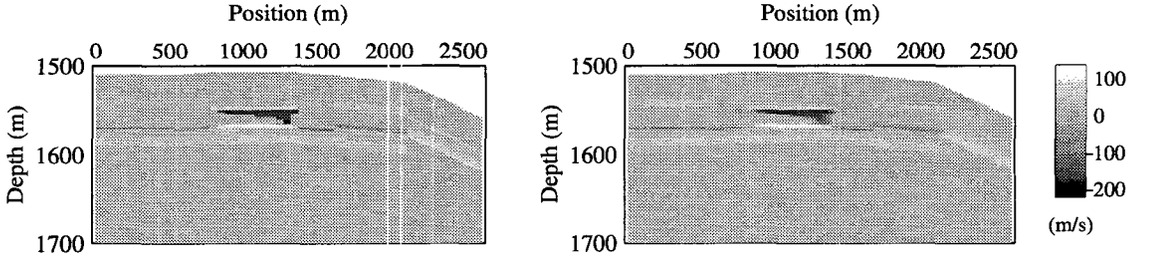

Figure 3.39: Change in V_P showing the base V_P subtracted from the unsmoothed V_P (left) and laterally-averaged V_P (right) for uniform fluid distribution and $S_g = 0.8$ in the gas cone.

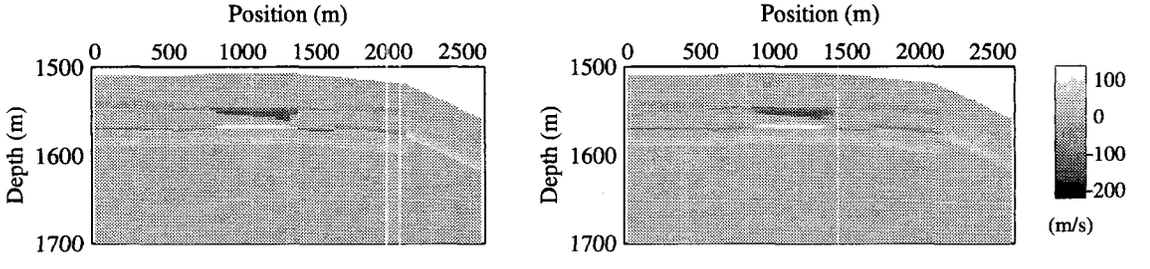

Figure 3.40: Change in V_P showing the base V_P subtracted from the unsmoothed V_P (left) and laterally-averaged V_P (right) for patchy fluid distribution and $S_g = 0.8$ in the gas cone.

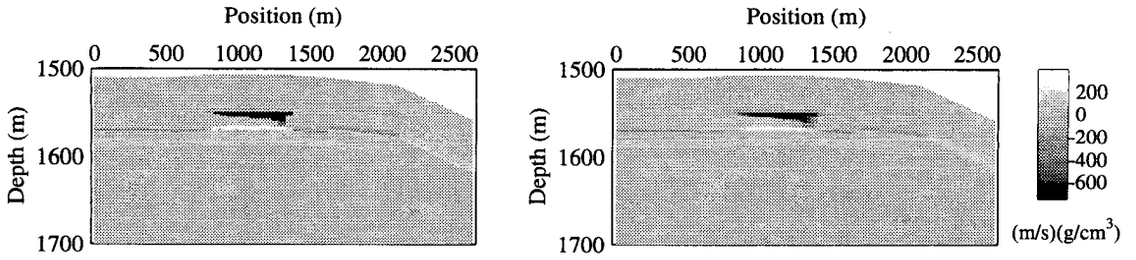

Figure 3.41: Change in I_P showing the base I_P subtracted from the unsmoothed I_P (left) and laterally-averaged I_P (right) for uniform fluid distribution and $S_g = 0.8$ in the gas cone.

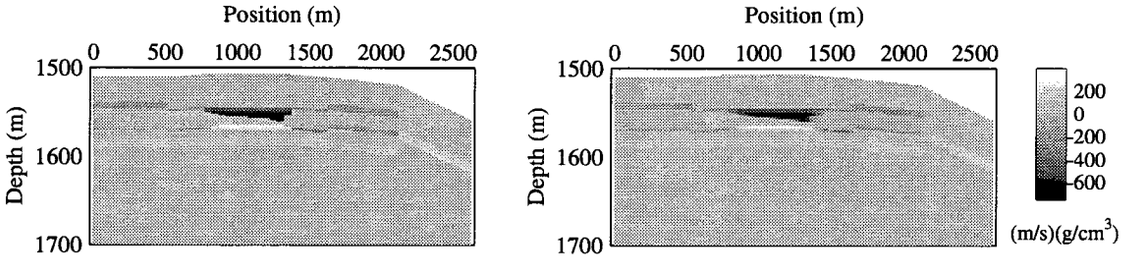

Figure 3.42: Change in I_P showing the base I_P subtracted from the unsmoothed I_P (left) and laterally-averaged I_P (right) for patchy fluid distribution and $S_g = 0.8$ in the gas cone.

3.7.2 Seismic Response

Since the velocity and impedance fields no longer have sharp transitions at grid block boundaries, we might anticipate that the seismic response will be different. I repeated the seismic modeling using the smoothed velocity and impedance fields. The resulting seismic images are shown in Figures 3.43-3.44. Each figure shows the seismic response of the original velocity field with $S_g = 0.8$, the seismic image of the corresponding smoothed velocity field, and the difference between the two. For the uniform fluid case, the amplitude of the seismic anomaly for the smoothed medium is 89% of the amplitude for the unsmoothed medium. The amplitude reduction for the patchy fluid cases is smaller: it is 97% as strong as the amplitude in the unsmoothed medium. However, the amplitude of the anomaly in the patchy case is still 11% smaller than in the uniform fluid case (compared to 19% smaller in the unsmoothed medium). Notice also the dimensions of the seismic anomaly change when the medium is smoothed. In both cases, the anomaly is approximately 50 m wider for the smoothed medium compared to the unsmoothed medium.

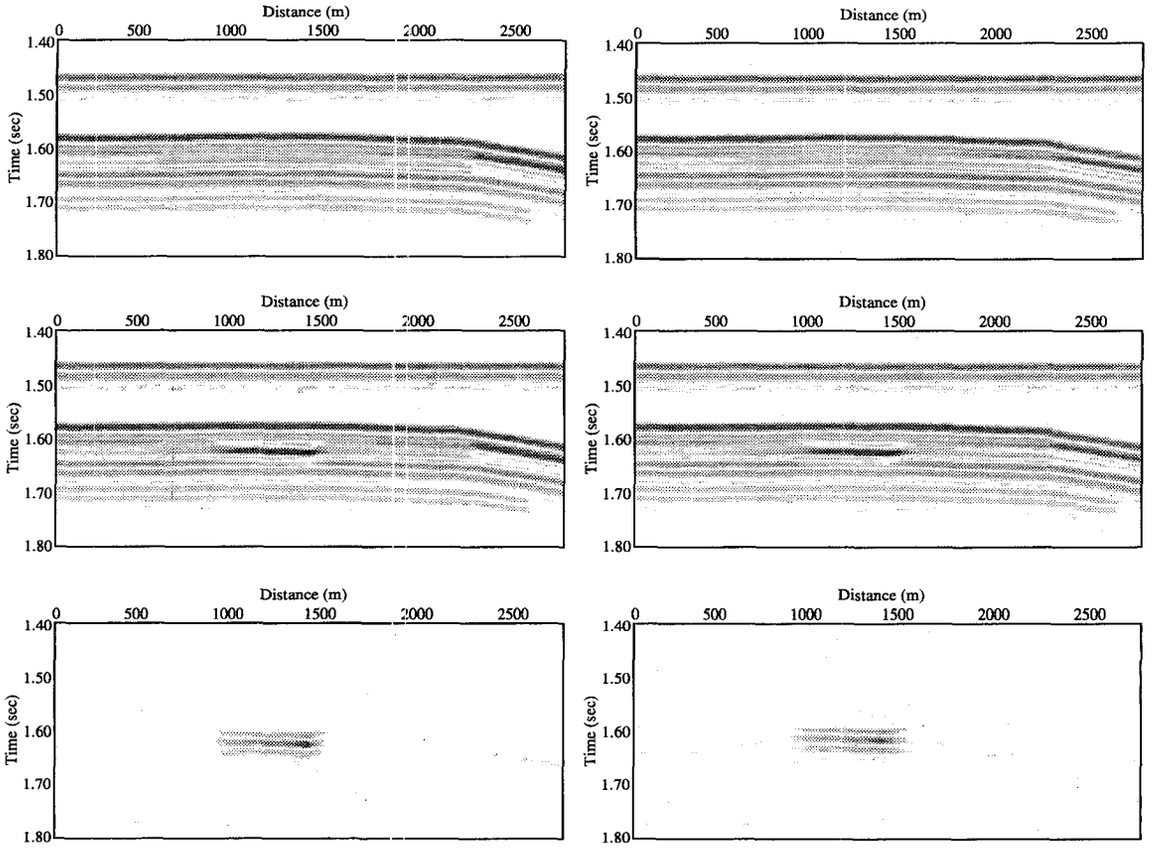

Figure 3.43: Comparison of seismic images for smoothed and unsmoothed velocity fields with uniform fluid distribution. Images in the left column show the seismic response to the unsmoothed field for the base survey (top), the monitor survey with $S_g = 0.8$ (middle), and the difference between the images (bottom). The corresponding images for the smoothed fields are in the right column.

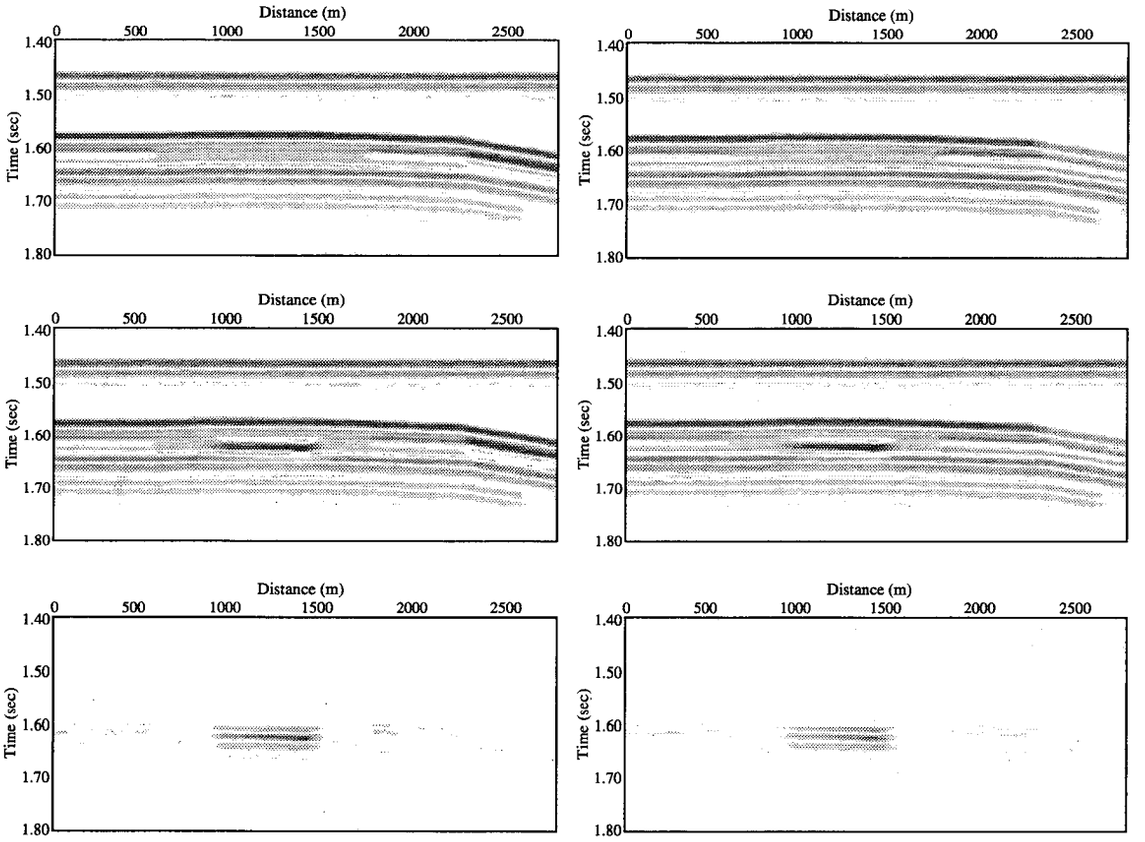

Figure 3.44: Comparison of seismic images for smoothed and unsmoothed velocity fields with patchy fluid distribution. Images in the left column show the seismic response to the unsmoothed field for the base survey (top), the monitor survey with $S_g = 0.8$ (middle), and the difference between the images (bottom). The corresponding images for the smoothed fields are in the right column.

3.8 Summary and Conclusions

I have presented here a procedure for studying the feasibility of monitoring primary oil production in a poorly-consolidated reservoir. I began with results from reservoir simulation, which showed evidence of gas coning in the oil zone. I used the geometry of the gas cone from the simulation results, and I modeled the compressional wave velocities in the reservoir for 4 levels of gas saturation in the gas cone: $S_g = 0.2$, 0.4, 0.6, and 0.8. I used laboratory measurements of V_P and V_S on 38 dry core samples from the Troll field as a basis for modeling the dry elastic moduli of the reservoir. Then, using both uniform and patchy fluid distribution models, I computed the saturated velocities in the reservoir. The distribution of V_P and density were inputs to a vertical incidence seismic model.

I show that for a uniform distribution of fluid, changes in the seismic signature of the reservoir show evidence of the gas coning for all levels of gas saturation. The amplitude of the seismic anomaly grows as gas saturation increases: for $S_g = 0.2$, the amplitude of the anomaly is 79% as strong as when $S_g = 0.8$. For patchy fluid distribution, the seismic anomaly is somewhat obscured by noise in the data when $S_g = 0.2$, but the anomaly grows as S_g increases. In all cases, the anomaly associated with patchy fluid distribution has a lower amplitude than the corresponding uniform fluid case. For $S_g = 0.8$, the seismic anomaly amplitude for the patchy case is only 81% as strong as in the uniform fluid case.

Laterally averaging the reservoir properties over a 25 m radius resulted in slightly different seismic results. For $S_g = 0.8$ in the gas cone, the amplitude of the seismic anomaly was 89% as strong for uniform fluid distribution and 97% as strong for patchy fluid. In both cases, the seismic anomaly was 50 m longer when the reservoir properties were smoothed.

One important implication from these results is that if patchy saturation persists on a seismic scale, it may lead to misinterpretation of seismic data. Small changes in gas saturation might not be distinguishable above the noise level, and repeated seismic surveys might not detect any changes. However, the range of seismic response seen here indicates that large increases in gas saturation (e.g. from 0% to >40%) should result in seismically detectable changes.

3.9 References

Blangy, J.P. and Strandenes, S., 1991, Stanford Rock Physics and Borehole Geophysics Project, **47**, Stanford University.

Blangy, J.P., 1992, Integrated seismic lithologic interpretation: the petrophysical basis: Ph. D. Thesis, Stanford University.

Gassmann, F., 1951, Elastic waves through a packing of spheres: Geophysics, **16**, 673–685.

Hill, R., 1963, Elastic properties of reinforced solids: Some theoretical principles: J. Mech. Phys. Solids, **11**, 357-372.

Kennett, B.L.N., 1983, Seismic wave propagation in stratified media, Cambridge University Press.

Lumley, D., Nur, A., Strandenes, S., Dvorkin, J., and Packwood, J., 1994, Seismic monitoring of oil production: A feasibility study: SEG Annual Meeting Expanded Technical Program Abstracts with Biographies, **64**, 319–322.

Lumley, D. E., 1995, Seismic time-lapse monitoring of subsurface fluid flow: Ph. D. Thesis, Stanford University.

Reuss, A., 1929, Berechnung der fleissgrense von mischkristallen auf grund der plastizitatsbedinggung fur einkristalle: Zeitschrift fur Angewandte Mathematik und Mechanik, **9**, 49–58.

van Meurs, P., 1957, The use of transparent three-dimensional mode ls for studying the mechanism of flow processes in oil reservoirs: Transactions, AIME, **210**, 295–301.

Chapter 4

Rock, Fluid, and Pore Pressure Effects on Seismic Monitoring

4.1 Abstract

The effectiveness of hydrocarbon recovery monitoring depends on the seismic visibility of the variations in reservoir elastic properties caused by changes in pore pressure and pore fluid replacement. In this chapter, I consider separately how rock frame stiffness, pore fluids, and pore pressure can affect the feasibility of seismic monitoring of hydrocarbon recovery. First, I show that a stiff rock frame might significantly reduce the feasibility of seismic monitoring of primary oil production. Next, I show how combinations of gas, oil, and brine affect the AVO signature of a Gulf Coast sand. I investigate both uniform and patchy saturation for a gas sand and show how a patchy mixture of gas and brine and a uniform mixture of live oil and brine might have similar AVO signatures. Finally, I show how reflectivity and AVO response of a gas sand could change as pore pressure decreases from 30 MPa to 15 MPa.

4.2 Fluid Substitution

Since pore fluids are a primary consideration in any reservoir recovery monitoring effort, we have to consider how they can affect seismic wave velocities. This section briefly

describes uniform fluid and patchy fluid distribution models used for fluid substitution. See Chapter 2 for a more detailed discussion of these models.

4.2.1 Uniform Fluid

In the uniform fluid distribution model, increments in pore pressure induced by seismic wave propagation diffuse so that pore pressure equilibrates during a seismic period. In this case, the pore fluids (e.g. oil, gas, and water) are under the same stress, and this iso-stress condition allows us to replace the three phases with an equivalent or "effective" fluid (Domenico, 1976). The effective bulk modulus of the fluid mixture, K_f, is described by the Reuss (1929) average of the individual constituents' bulk moduli, K_{f_i} as follows:

$$K_f = \left(\sum_{i=1}^{N} \frac{f_i}{K_{f_i}} \right)^{-1} . \tag{4.1}$$

I then estimate the bulk modulus of the saturated rock, K_{Sat}, from the Gassmann (1951) relationship, using the rock mineral bulk modulus, K_o, dry rock bulk modulus, K_{Dry}, rock porosity, ϕ, and the fluid bulk modulus from Equation 4.1:

$$\frac{K_{Sat}}{K_o - K_{Sat}} = \frac{K_{Dry}}{K_o - K_{Dry}} + \frac{K_f}{\phi \left(K_o - K_f \right)} , \tag{4.2}$$

$$\mu_{Sat} = \mu_{Dry} . \tag{4.3}$$

The shear modulus, μ, remains unchanged with saturation in the Gassmann model, and I carry this uniform shear modulus assumption through all modeling exercises.

4.2.2 Patchy Fluid

In the patchy model, increments in pore pressure induced by seismic wave propagation do not diffuse during a seismic period. Fluid flow resulting from the pore pressure gradients between patches will result in attenuation and dispersion of seismic waves. Within each patch, pore pressure equilibrates, and the single fluid or multi-phase mix of pore fluids acts locally as an effective fluid. I use Equation 4.1 to compute the effective bulk modulus of the pore fluid in each patch, and I calculate the bulk modulus of each patch using the Gassmann relationship in Equation 4.2. The effective medium is, then, a mixture of the reservoir rock

with different states of saturation. In keeping with the low frequency Gassmann theory, I assume that the rock shear modulus is uniform, independent of the saturation condition. Hill (1963) demonstrated that for a composite with a uniform shear modulus, the following relationship holds:

$$\frac{1}{K_{eff}+\frac{4}{3}\mu} = \sum_{i=1}^{n}\left(\frac{f_i}{K_{sat_i}+\frac{4}{3}\mu}\right). \tag{4.4}$$

This tells us that the effective bulk modulus, K_{eff}, depends only on the volume fraction, f_i, and bulk modulus of each patch. It is independent of the patch shape. I use K_{eff} from Equation 4.4 and the uniform shear modulus to calculate the P-wave modulus, $K+4/3\mu$, of the effective medium.

4.3 Effect of Frame Stiffness

A key parameter that controls the amplitude of variations in reservoir elastic properties is the stiffness of the rock frame. In this section, I investigate the importance of this parameter for three high-porosity sandstones. I find that for a compliant reservoir rock, coning of gas during primary oil production is seismically visible even with a significant noise level. However, if a rock is stiff (e.g., due to efficient grain cementation), such changes may be masked by noise, even for high-porosity reservoirs.

4.3.1 Introduction

In order to use seismic methods to monitor the injection and withdrawal of fluids in a hydrocarbon reservoir, it is necessary to know how the seismic characteristics of the reservoir rock change with temperature, pressure, and fluid saturation. Lumley et al. (1994) investigated the feasibility of monitoring primary oil production in the Troll Field. Using flow simulation results, the authors modeled the seismic wave velocities with changes in reservoir saturation. Then, through elastic forward modeling, they determined that the expansion of a gas cone could be detected by subtracting a baseline seismic survey from a repeated (monitoring) survey.

The principle is that the signatures of the lithological background do not change between the two surveys, so the changes associated with pore fluid replacement and pore

pressure changes should stand out. However, random noise may obscure the picture if impedance changes are small between the surveys. In the Troll study, the reservoir porosity ranged from 13 to 35%. Dvorkin and Nur (1996) show that cementation at grain boundaries can significantly increase the rock stiffness with only a small reduction in porosity. It is conceivable, then, that a similar production scenario could be observed for varying rock types. This is why I undertake this sensitivity analysis.

Specifically, I investigate the effect of rock frame stiffness (or cementation) on the seismic visibility of a developing gas cone. I use three high porosity sandstones, representing a range of stiffnesses, as inputs to my velocity models: 1) Troll reservoir rock, 2) an outcrop sandstone, and 3) Oseberg reservoir rock. The bulk and shear moduli of outcrop sandstone are about 1.8 and 1.3 times those of the Troll sandstone. The Oseberg rock is about 2.1 times stiffer than Troll in bulk modulus and 1.9 times stiffer in shear modulus. I model the changes in velocity for each rock type at 30 MPa effective pressure. Then, using a propagator matrix method with zero offset, I model the seismic response for each case.

For the compliant Troll rock, I find the development of a gas cone is seismically visible. The seismic response to the gas cone in the outcrop sandstone is still visible, but the anomaly magnitude is smaller. For the Oseberg rock, noise begins to obscure the seismic visibility of the gas cone.

4.3.2 Model Description

In this study, I consider three cases of rocks with varying degrees of cementation. For the first case, I use very soft unconsolidated North Sea sands (Blangy, 1992). For the second case, I use stiffer quartz-cemented outcrop rock from the Stanford Rock Physics database. For the third case, I use clean quartz sandstone from the Oseberg field (Strandenes, 1991), which are the stiffest among the three groups. Figure 4.1 shows how the dry-rock bulk and shear moduli vary with porosity for these three rock types. I use these properties along with porosity, pressure, and fluid distribution from reservoir simulation to calculate the spatial distribution of compressional wave velocity and compressional impedance at the beginning and end of simulation. I then use the output from rock physics modeling to investigate the seismic response in each case.

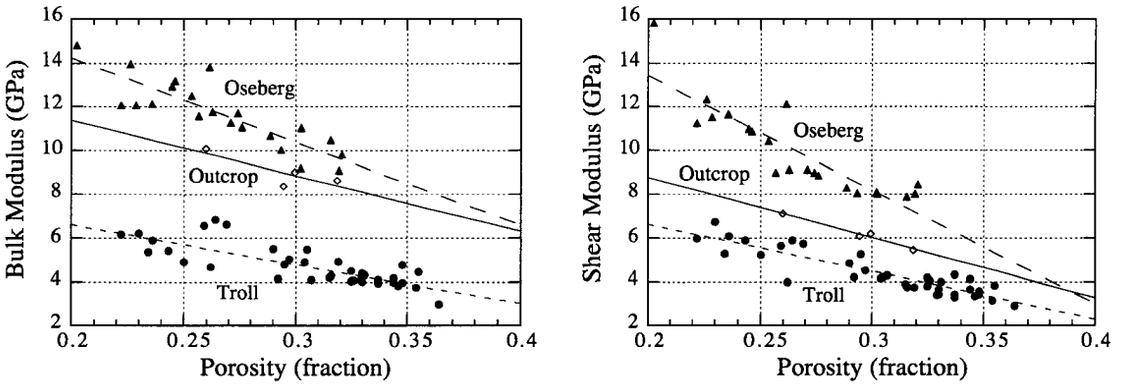

Figure 4.1: Dry bulk and shear moduli versus porosity for three cases.

4.3.3 Rock Physics Model

To model the saturated rock velocities, I first determine the dry rock moduli in each reservoir simulation cell. Each cell had assigned values of porosity, and I used the regression lines shown in Figure 4.1 to determine the dry rock moduli for each rock type. Changes in pore pressure are small enough in the flow simulation ($<$0.25 MPa) that they can be ignored here. Also, I assume the fluid phases (water, oil, and gas) in each reservoir simulation cell are uniformly distributed within the pore space. Variations in pore fluid distribution are small enough that they do not affect seismic wave propagation. I use the uniform fluid model described in Section 4.2.1 to calculate the effective fluid bulk modulus in each reservoir simulation cell, which I then use along with the dry rock elastic moduli to calculate the saturated moduli.

I use the results of reservoir simulation of primary production from a thin oil zone as input to the rock physics model. The simulation output gave the spatial and temporal distribution of pore fluids and pore pressure, which I keep the same for the three cases. Using this information, I calculate the seismic velocities in the reservoir at the beginning and at the end of simulation. These velocity models are the input for the seismic modeling.

4.3.4 Seismic Model

To simulate a CDP stacked section, I use zero source-receiver offset at 50 meter intervals across the reservoir, and I assume horizontal layers with velocities and densities that correspond to the vertical velocity and density profile at each location. I model the seismic response for plane wave, normal incidence propagation in 1-D layered media using the propagator matrix method (Aki and Richards, 1980; Claerbout,1985). An advantage of this method is that it is relatively fast. However, the model does not yield any information about amplitude variation with offset (AVO), which might be crucial in some monitoring projects. This zero-offset method appears to accurately model the shape and location of the seismic anomaly: the results compare well to those of Lumley et al. (1994), where they used a more rigorous generalized Kirchhoff method for elastic modeling.

4.3.5 Rock Physics Modeling Results

The feasibility of recovery monitoring depends on changes in velocity and impedance in the reservoir. An effective technique of viewing the variations is to subtract the initial velocity and impedance from the values at a later time. By doing so, the spatial variations between the surveys can be seen.

Velocity Changes

The results of the rock physics modeling show that there are significant changes in V_P during simulated production (Figure 4.2). This figure shows the difference in V_P obtained by subtracting the initial V_P distribution from the values at the end of fluid flow simulation. Looking at the Troll case (top), the main feature evident is in the central region of the reservoir at a depth of around 1550 meters. This is the region where gas is coning down into the oil zone, and it thickens from left to right across the reservoir. The maximum decrease in V_P here is 8.2%. Below this, at a depth of around 1570 meters, water coning causes an increase in V_P, with the maximum being 4.8%. The results for the outcrop case (middle), are similar in pattern, but the percentage change is smaller than Troll. The maximum decrease in V_P is 3.7% at the lower tip of the gas cone, while the maximum increase is 3.6%. The effect of stiffening the rock frame is most evident in the Oseberg case (bottom).

Here, the large change in V_P is not seen over the entire gas cone region. Only the tip of the gas cone shows a significant decrease in V_P, with the maximum decrease of 2.5%. The maximum increase in velocity of 3.8% occurs in the region at the top of the gas cone. A closer inspection reveals that V_P increases in this same region for all 3 cases. The reason for this increase in velocity is that the change in density is large enough to offset the change in bulk modulus that results from fluid substitution. Recall that compressional wave velocity is calculated as follows:

$$V_P = \sqrt{\frac{K_{Sat} + \frac{4}{3}\mu}{\rho}}, \tag{4.5}$$

where K_{Sat} is the saturated bulk modulus from the Gassmann relationship, μ is the shear modulus, and ρ is the saturated rock density. In each case, the density decreases in this region by 7.9%. For Oseberg rock, K_{Sat} decreases by 1.5%, resulting in a 3.8% increase in V_P. For Troll rock, increase in V_P. For Troll, K_{Sat} decreases by 5.0%, and the resulting increase in V_P is 3.0%.

An inspection of the changes in the velocity field indicates that there may be significant variations in the seismic visibility of the developing gas cone.

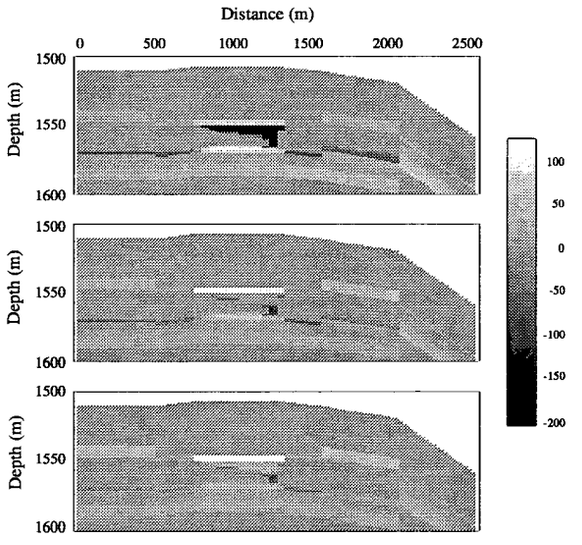

Figure 4.2: Changes in compressional wave velocity (Final V_P - Initial V_P), (m/s), for Troll (top), outcrop sandstone (middle), and Oseberg (bottom).

Impedance Changes

Observed changes in the compressional impedance, I_P, are another means of assessing the feasibility of detecting changes in the reservoir with seismic surveys. The compressional impedance is the product of the rock density and V_P (ρV_P), and changes in I_P may give an indication of expected changes in reflectivity. A comparison of changes in I_P for the 3 cases (Figure 4.3) shows the same spatial pattern with some variation in the magnitude of change. In all 3 cases, the entire gas cone shows a decrease in I_P even in the region where V_P increased. For Troll (top), the change in impedance was the greatest, with a maximum decrease of 16.5% in the gas cone and a maximum increase in I_P of 6.8%. For the outcrop case (middle), the magnitude of impedance change is smaller than in Troll, with the maximum decrease of 11.1% and the maximum increase of 3.9%. For Oseberg (bottom), the same pattern emerges in the map of impedance change as seen in the other 2 cases, even though the velocity change is small in most of the gas cone. The maximum decrease in I_P here is 10.1%, and the maximum increase is 3.1%.

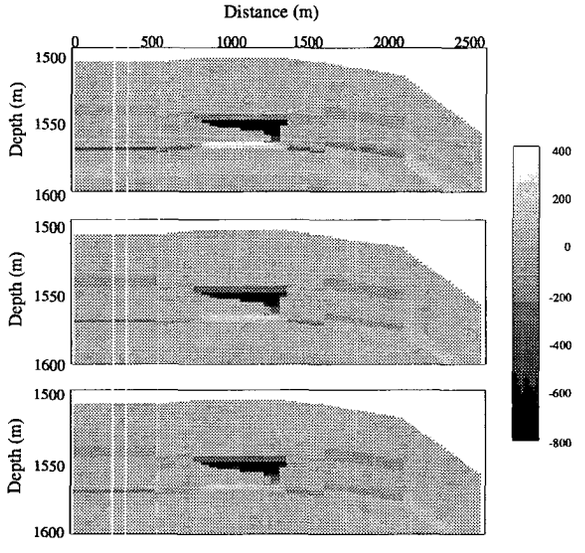

Figure 4.3: Changes in compressional impedance (Final I_P - Initial I_P), (m/s)(g/cm^3), for Troll (top), outcrop sandstone (middle), and Oseberg (bottom).

The impedance maps show less variation between the cases than the velocity maps. The density change is the factor that makes them more similar among these high porosity rocks. For the region where V_P increased at the top of the gas cone, I_P decreased by 5.2% in the Troll case, while it decreased by 4.4% in the Oseberg case. The 7.9% decrease in density causes the impedance to decrease in this region.

4.3.6 Seismic Modeling Results

After calculating the velocity and impedance distribution before and after production, I model the seismic response of the reservoir at both times. The results from Troll are shown in Figure 4.4, which has three parts: 1) The seismic image at the onset of production (top), 2) The seismic image after 113 days of production (middle), and 3) A subtraction of the base line image from the final image (bottom). Random noise is added to the seismic traces at a signal-to-noise ratio of 10:1. As in Lumley et al. (1994), the gas cone is evident in the seismogram after 113 days, and the difference section highlights the region of change in the reservoir. Note that the anomaly strengthens from left to right, corresponding to the thickening of the gas cone in that direction.

Stiffening the rock frame did alter the results of the seismic visibility of the gas cone. For the outcrop case, the subtraction of the baseline from the monitor survey (Figure 4.5) shows that the anomaly magnitude is about 54% as strong as in the Troll case, but it is still visible. The strengthening of the anomaly from left to right is not as evident here. In the Oseberg case (Figure 4.6), the magnitude of the anomaly is about 45% of that in the Troll case, and the noise begins to obscure the visibility of the anomaly.

4.3.7 Summary

In summary, I investigated 3 cases of rock frame properties to determine the effect of frame stiffness on the seismic detection of a developing gas cone. For the Troll rock, a loosely-consolidated sand, the maximum decrease in compressional wave velocity was 8.2%, and the maximum decrease in impedance was 16.5%. Seismic modeling showed strong evidence of the gas cone on the simulated monitor survey, and subtracting the baseline image from the final image showed a strong anomaly. For the outcrop sandstone, which has a

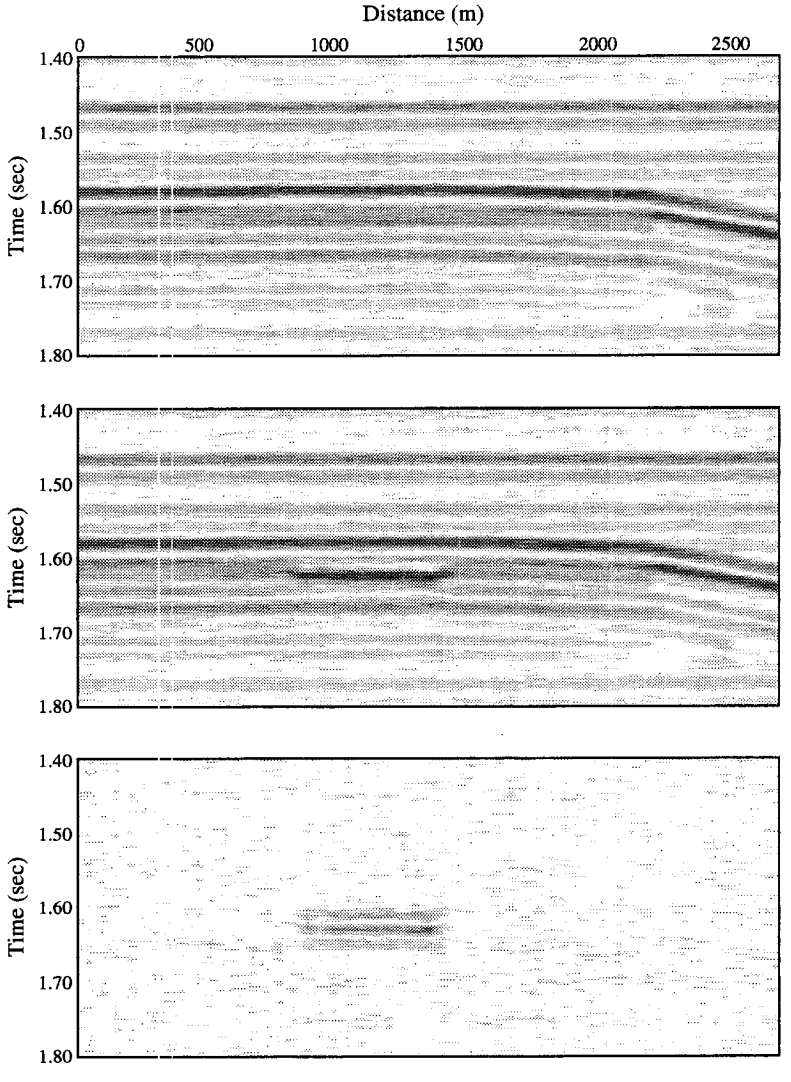

Figure 4.4: Seismic images for Troll case. The top image is the baseline survey, the middle image is the monitor survey, and the bottom image is the monitor - baseline.

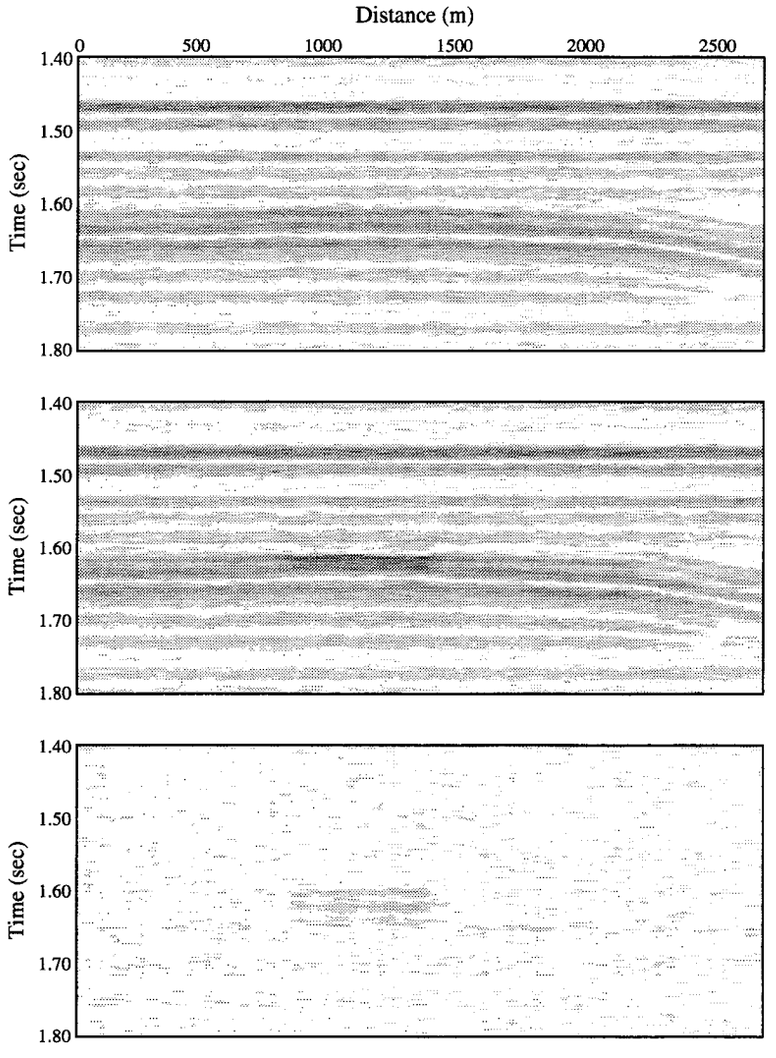

Figure 4.5: Seismic images for outcrop case. The top image is the baseline survey, the middle image is the monitor survey, and the bottom image is the monitor - baseline.

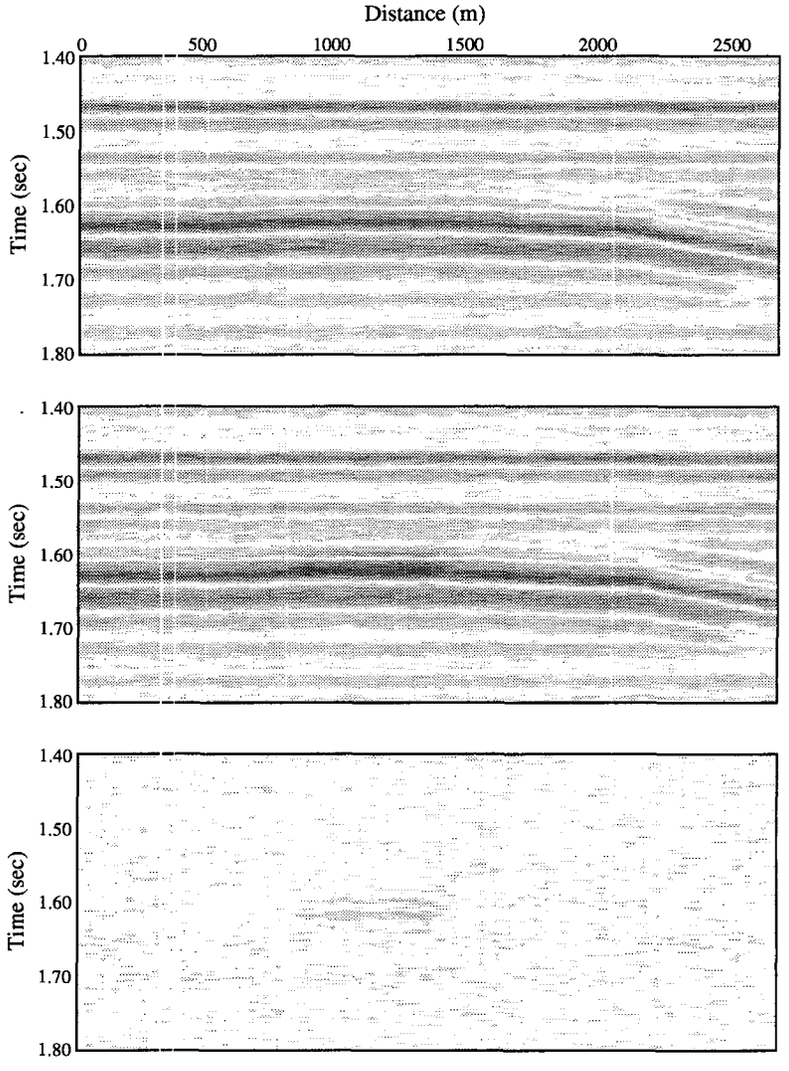

Figure 4.6: Seismic images for Oseberg case. The top image is the baseline survey, the middle image is the monitor survey, and the bottom image is the monitor - baseline.

frame that was about 1.8 times more stiff than Troll, the maximum decrease in compressional wave velocity was 3.7%, and the maximum decrease in compressional impedance was 11.1%. Seismic modeling showed an anomaly that was not as strong as in the Troll case. For Oseberg rock, a weak velocity decrease in the region of the gas cone was observed. The strongest region of change in compressional wave velocity was an increase of 3.8% at the top of the gas cone, but the velocity did decrease slightly through the rest of the cone, with a maximum decrease of 2.5%. The compressional impedance decreased in the entire gas cone region, with a maximum of 10.1%. Seismic modeling showed a weak anomaly by subtracting the baseline image from the final image.

This study demonstrated the feasibility of monitoring the development of a gas cone with repeated seismic surveys. As the rock frame stiffness increases, the seismic anomaly decreases in magnitude, but it is still visible. Noise began to obscure the anomaly in Oseberg rock, which had the highest degree of cementation. Other seismic attributes, such as AVO or attenuation, may be important in monitoring recovery processes. This is an area for further investigation.

4.4 Effect of Pore Fluids

Another key parameter that affects reservoir elastic properties is the compressibility of the pore fluid. In this section, I show the effects of different states of saturation on the velocity and reflectivity of a Gulf Coast sand. Starting with a well log, I invert the log to get the dry rock elastic properties. Then I calculate the velocities in the rock saturated with brine, oil, and gas. Using this information, I model CDP gathers in order to compare the seismic response. Such exercises are helpful in understanding changes in the seismic response of a reservoir during production, such as a flood front moving through the reservoir.

4.4.1 Background and Methodology

Beginning with a log from a Gulf Coast well, I picked a sand interval that had indications of hydrocarbon saturation. I shifted the log depths from their original values, and I extracted a single gas sand approximately 25 m thick bounded by two shale layers, both with higher V_P than the gas sand. With brine saturations calculated from the deep resistivity log, I use

the following relationships, derived from Equations 4.2- 4.3, to invert the velocity logs to get the dry rock bulk modulus, K_{Dry}, and shear modulus, μ_{Dry}, modulus:

$$K_{Dry} = K_{Sat}\frac{\phi K_o + (1-\phi)K_f - K_f K_o/K_{Sat}}{\phi K_o - (1+\phi)K_f + K_f K_{Sat}/K_o}, \tag{4.6}$$

$$\mu_{Dry} = \mu_{Sat}, \tag{4.7}$$

where K_{Sat} is the bulk modulus of the saturated rock, K_o is the rock mineral bulk modulus, ϕ is the rock porosity, K_f is the fluid bulk modulus, and μ_{Sat} is the saturated shear modulus.

Having the dry rock properties, I then calculated the saturated bulk modulus for various states of fluid saturation using Equation 4.6. The saturating fluids I present here are a gas with a specific gravity of 0.8 compared to air at standard temperature and pressure, a gas-free 35°API oil, a live 35°API oil with a gas-oil ratio (GOR) of 200, and a brine with salinity of 85,000 ppm. I used a pore pressure of 24.8 MPa and a temperature of 55°C for the reservoir conditions, and I used the relationships given by Batzle and Wang (1992) to calculate the fluid densities and bulk moduli. The original brine saturation in the reservoir was around 20%, so I used this value in most of the calculations except for the 100% brine saturation case. In each case with more than one fluid in the pore space, I assumed the fluids were uniformly distributed.

In the second modeling exercise, I assumed that gas and brine in the pore space were distributed in two ways: uniform and in patchy. Using these fluid distribution models (see Sections 4.2.1- 4.2.2), I compare the velocities and reflectivities for rock that is 80% gas-saturated and 65% gas-saturated, both having brine filling the remainder of the pore space. In the patchy model, I assume that each patch of rock is either 100% gas saturated or 100% brine saturated. I calculate the bulk modulus of each patch using the Gassmann relationship in Equation 4.6, then I use K_{eff} from Equation 4.4 and the uniform shear modulus to calculate the P-wave modulus of the effective medium.

For the calculation of the P-wave reflection coefficient, R_{PP}, I use the following approximation of the Zoeppritz equations given by Shuey (1985):

$$R_{PP}(\Theta_1) \approx R_P + \left(A_0 R_P + \frac{\Delta\nu}{(1-\nu)^2}\right) sin^2\Theta_1 + \frac{1}{2}\frac{\Delta V_P}{V_{Pa}}\left(tan^2\Theta_1 - sin^2\Theta_1\right), \tag{4.8}$$

where RP is the normal incidence reflection coefficient,Θ_1 is the incident P-wave angle,ν

is Poisson's ratio, and A_0 is given by

$$A_0 = B_0 - 2(1+B_0)\left(\frac{1-2\nu}{1-\nu}\right), \tag{4.9}$$

and

$$B_0 = \left(\frac{\frac{\Delta V_P}{V_{Pa}}}{\frac{\Delta V_P}{V_{Pa}} - \frac{\Delta\rho}{\rho_a}}\right). \tag{4.10}$$

V_{Pa} is the average P-wave velocity at the interface, ρ_a is the average density, ΔV_P is the change in P-wave velocity across the interface and $\Delta\rho$ is the change in density.

The final step in the study was to model CDP gathers for each scenario. I accomplished this by using the Hampson-Russell AVO modeling software. The inputs for the modeling were V_P, V_S, density and Poisson's ratio logs, which were computed using the methods previously discussed.

4.4.2 Velocity and Reflectivity Results

The results of the fluid substitution in the sand interval are shown in Figures 4.7-4.8. The top portion of each figure shows the calculated P-wave velocity in well log format along with the gamma ray log, while the bottom of each figure shows the reflection coefficient, R_{PP}, versus incident angle. For the first exercise, shown in Figure 4.7, we see that the velocity in the sand ranges from about 1550 to 1800 m/s in the original log, while the brine-saturated velocities are around 2300 m/s, comparable to the bounding shale layer velocities. As expected, the reflection coefficients at the top of the sand vary significantly for the various fluids. For the log velocities, R_{PP} ranges from -0.23 at 0° incident angle to -0.32 at 40° incident angle. For the live oil, the pattern is similar, but the magnitude of the R_{PP} is less, ranging from -0.17 to -0.25. For the brine-saturated rock, R_{PP} starts out near zero and slightly negative, and it becomes slightly positive at large incident angles.

For the second exercise, the results are presented in Figure 4.8. The velocity logs show little difference between the uniform saturation distribution cases, and there is little difference in the reflection coefficients for these two cases. R_{PP} ranges from around -0.25 to -0.34 for both 80% and 65% gas saturation. For the patchy saturation with 80% gas and 20% brine, the R_{PP} ranges from -0.23 to -0.31. These values are not too different from the uniform saturation. However, for the second case with 65% gas and 35% brine,

the values of R_{PP} for the patchy saturation are slightly lower than for uniform saturation. These values range from -0.19 to -0.28. The velocities and reflection coefficients for the patchy saturation for this second case look similar to the live oil shown in Figure 4.7.

4.4.3 Synthetic Seismic Results

For each case previously described, I created synthetic CDP gathers that are NMO corrected. I computed the CDP's to an offset of 2500 m. These results are shown in Figure 4.9. The four synthetic CDP gathers at the top of Figure 4.9 show the results from the first exercise. The live oil case shows characteristics that are similar to the synthetics based on the log velocities. The main distinction is that the amplitudes are smaller for the live oil case. The gas-free oil case and the brine case are more distinct. For the gas-free oil case, the doublet seen at the base of the sand at the near offsets merges into a single peak. For the brine case, we see the effect of the reflection coefficient becoming positive at the far offsets. Both the trough at around 1575 ms and the peak below it reverse polarity at the far offsets.

The results of the second exercise, comparing uniform to patchy saturation distributions, are shown in the bottom four CDP gathers in Figure 4.9. The differences in these synthetic CDP gathers are subtle. The main difference is that the amplitudes are slightly reduced for the patchy distributions. Also, the trough at around 1590 ms is less distinct in the patchy cases when compared to the uniform fluid cases. Note how similar the patchy case with 65% gas and the live oil case appear. As mentioned in the previous section, the velocities and reflectivities for these two cases are similar.

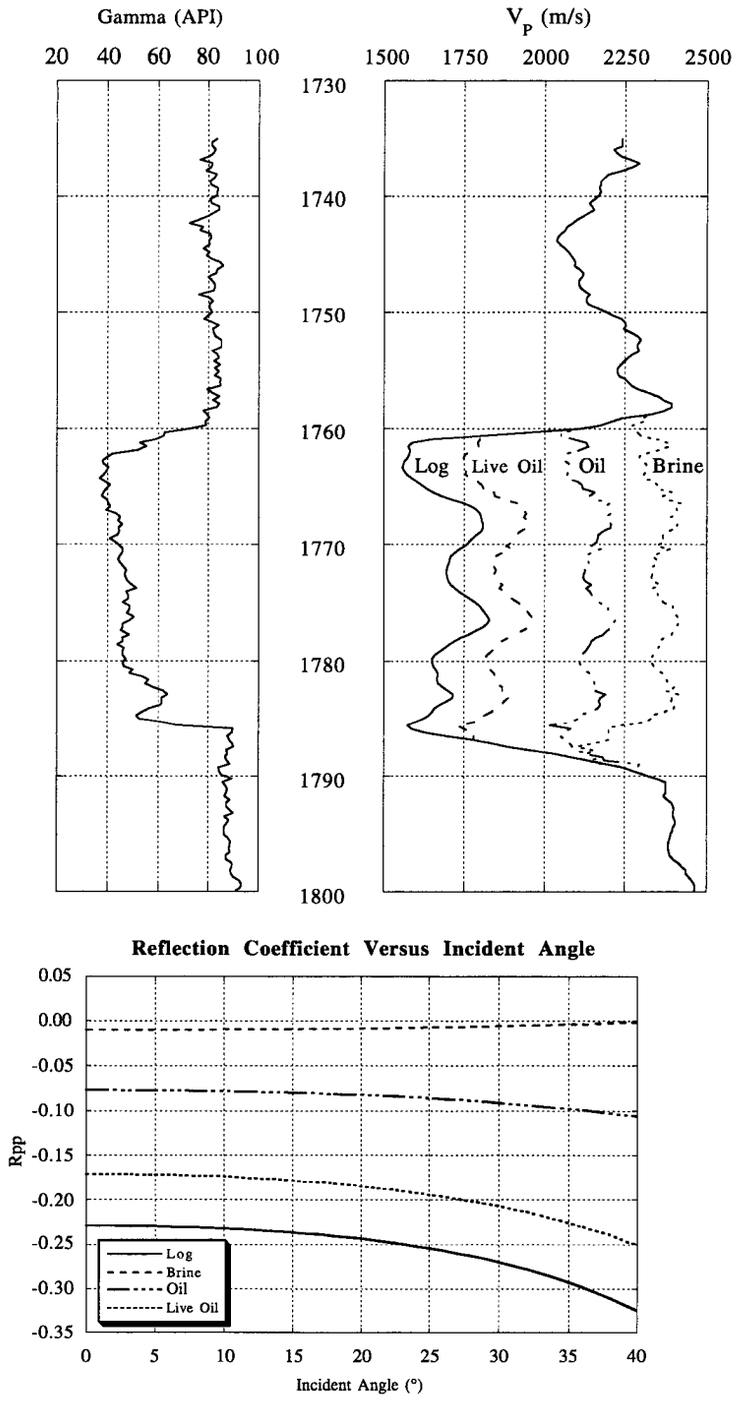

Figure 4.7: Top - Gamma ray and velocity logs (depth in m) showing results of fluid substitution in the sand. Bottom - Reflection coefficient at top of sand using the Shuey approximation.

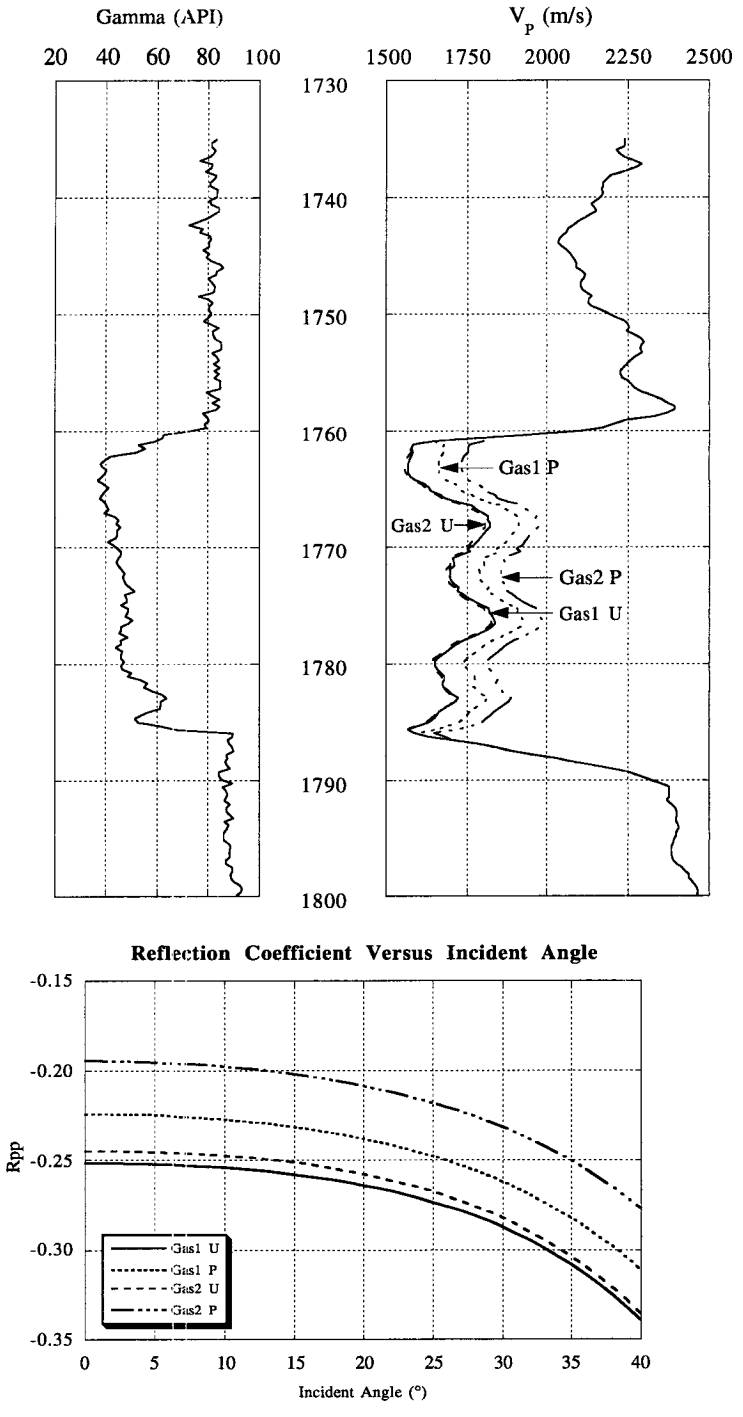

Figure 4.8: Top - Gamma ray and velocity logs (depth in m) showing results for uniform (U) and patchy (P) fluid distributions. Bottom - Reflection coefficient at top of sand using the Shuey approximation.

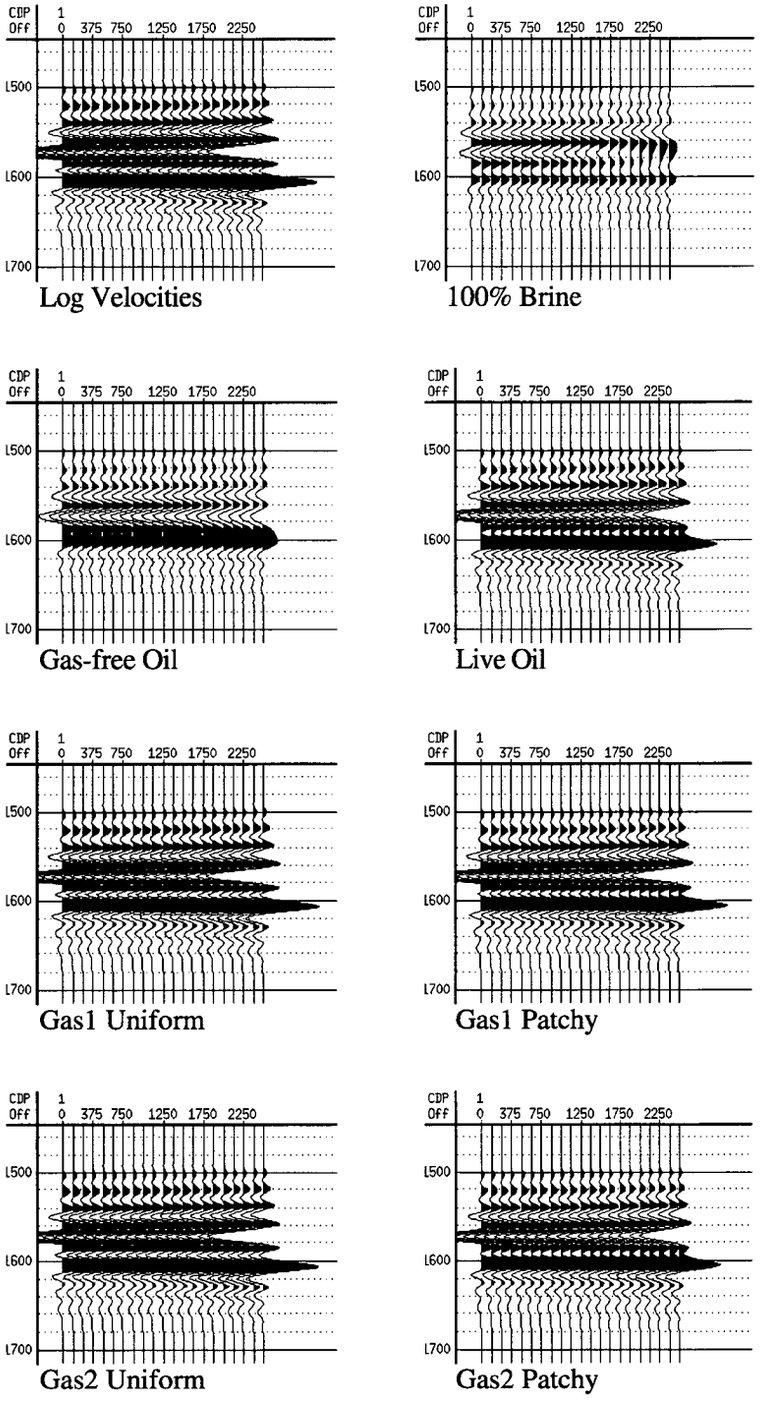

Figure 4.9: Synthetic CDP gathers showing offset (m) versus time (ms) over a Gulf Coast sand for various states of fluid saturation. Both cases with oil saturation include 20% brine. Gas1 refers to 80% gas saturation, and Gas2 refers to 65% gas saturation. The seismic response for both uniform and patchy fluid distributions are shown.

4.5 Effect of Pore Pressure

A third parameter that can affect reservoir elastic properties is pore pressure, which affects both pore fluid and rock frame properties. In this section, I show how changes in pore pressure can change the seismic signatures of a gas sand.

4.5.1 Effects of Pressure on Pore Fluids

Fluid properties relevant to the propagation of seismic waves are compressibility, density, and viscosity. Changes in pressure and temperature affect all three of these physical properties. Pore pressure changes during the productive life of a reservoir can result in significant changes in pore fluid properties. For example, changes in pore fluid bulk modulus with pressure can be easily computed if you know gas gravity, oil density (or API number), gas-oil ratio (GOR), and brine salinity. To illustrate how the density and bulk modulus of pore fluids can change with pressure, I give the following example. Using the relationships given by Batzle and Wang (1992), I calculated the density and bulk modulus of a gas with 0.55 specific gravity and a 35°API oil with a GOR of 50 (l/l) at a temperature of 60°C. The results are shown in Figure 4.10. Changes in these fluid properties with changing pore pressure affect the bulk density and bulk modulus of a fluid saturated rock. For example, a decrease in pore pressure from 30 MPa to 15 MPa would decrease the gas density 47% and decrease the gas bulk modulus 59%. These changes in gas properties will affect the seismic velocity by decreasing both the saturated bulk modulus and the saturated density.

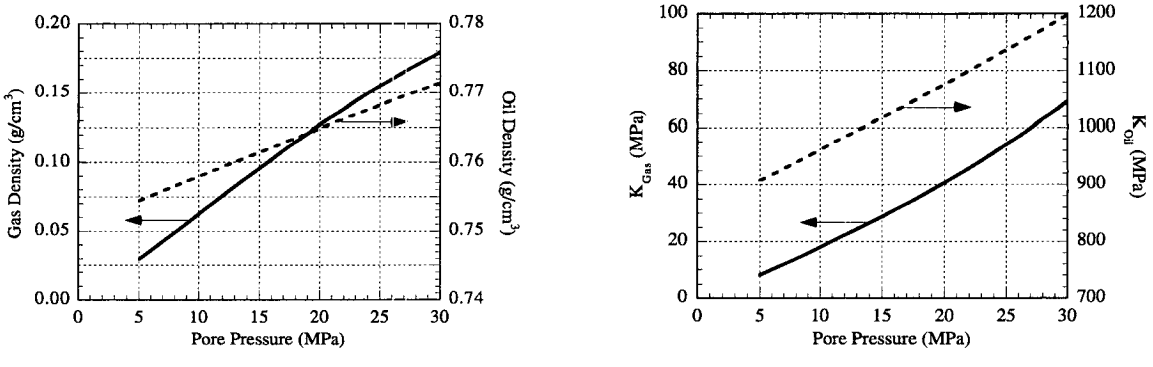

Figure 4.10: Density (left) and bulk modulus (right) of a 0.55 specific gravity gas and a 35°API oil with a gas-oil ratio of 50 (l/l) as a function of pore pressure.

4.5.2 Effects of Pressure on Rock Frame

Recovery processes can alter the stiffness of rock through changes in pore pressure, thereby changing the seismic wave velocities. During primary reservoir depletion, the pore pressure decreases, thus increasing the net effective stress on the formation. Figure 4.11 shows dry velocities (V_P and V_S) and elastic moduli (K_{Dry} and μ_{Dry}) versus effective pressure for an Ottawa sand sample from Domenico (1977). V_P increases by 29 percent and V_S increases by 31 percent when the effective confining pressure increases from 5 MPa to 15 MPa. Note the rate of velocity increase diminishes with increasing net stress. For this sample, an increase of confining pressure from 15 MPa to 30 MPa results in an increase in V_P of 19 percent. This stiffening of the rock with increasing effective pressure results from the closing of cracks and the consolidation of grains. Another way to look at the effect of pore pressure is to consider a secondary recovery process where the pore pressure is increased through injection. Increasing the pore pressure decreases the effective stress, resulting in a decrease in the elastic moduli of the rock frame.

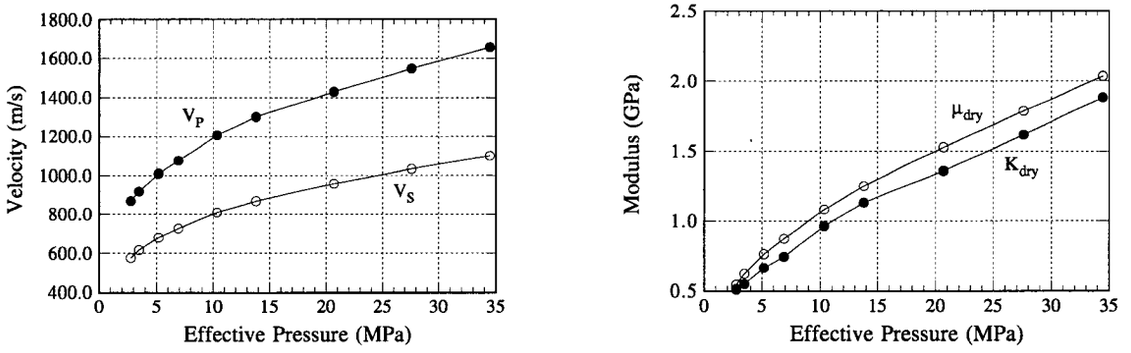

Figure 4.11: Compressional and shear wave velocities (left) and dry bulk and shear moduli (right) in dry Ottawa sand (from Domenico, 1977).

I will look at a pore pressure decrease in a gas sand that results in an increase in effective pressure from 15 MPa to 30 MPa. The corresponding increases in K_{Dry} and μ_{Dry} are 41% and 45%, respectively. Although I did not have actual measurements of dry rock properties for the sand in this study, I assume that it responds to effective pressure in a similar manner as the Ottawa sand shown here.

4.5.3 Velocity and Reflectivity Changes in a Gas Sand

Using the Gulf Coast sand from Section 4.4, I modeled the velocities and reflectivities at the top of sand saturated with 80% gas and 20% brine at 2 pore pressures. Assuming the sand starts out overpressured at 30 MPa, I model the velocity and reflectivity for fluids that are uniformly distributed. I then repeat the exercise at 15 MPa pore pressure to simulate how velocity and reflectivity could change as the reservoir is depleted. The results are presented in Figure 4.12. At the higher pore pressure, R_{PP} ranges from around -0.26 at zero offset to -0.34 at 40° offset. At 15 MPa, R_{PP} ranges from around -0.20 to -0.31.

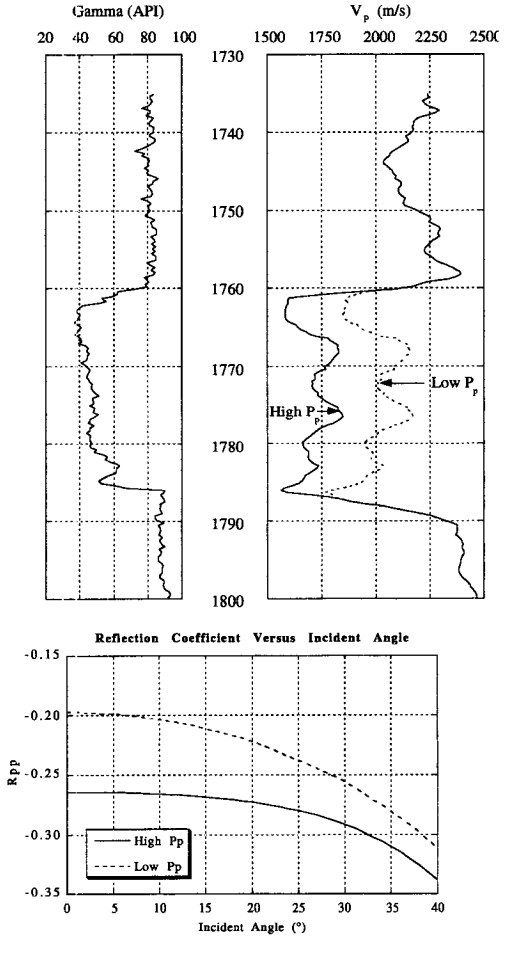

Figure 4.12: Top - Gamma ray and velocity logs (depth in m) showing results of decreasing pore pressure from 30 MPa (High P_p) to 15 MPa (Low P_p). Bottom - Reflection coefficient at top of sand using the Shuey approximation.

4.5.4 Effects of Pressure on Seismic Response

For each case of pore pressure, I created a synthetic CDP gather, computed to 2500 m offset and NMO corrected. These results are shown in Figure 4.13. As expected from the results shown in Section 4.5.3, the amplitudes at the top and base of the sand are larger at 30 MPa than at 15 MPa pore pressure. The other notable difference between the two is the pull-up of the peak at the base of the gas sand at the lower pore pressure. This peak occurs 4 ms earlier (at 1600 ms) at 15 MPa pore pressure. The decreased amplitudes and velocity pull-up both result from the pore pressure depletion.

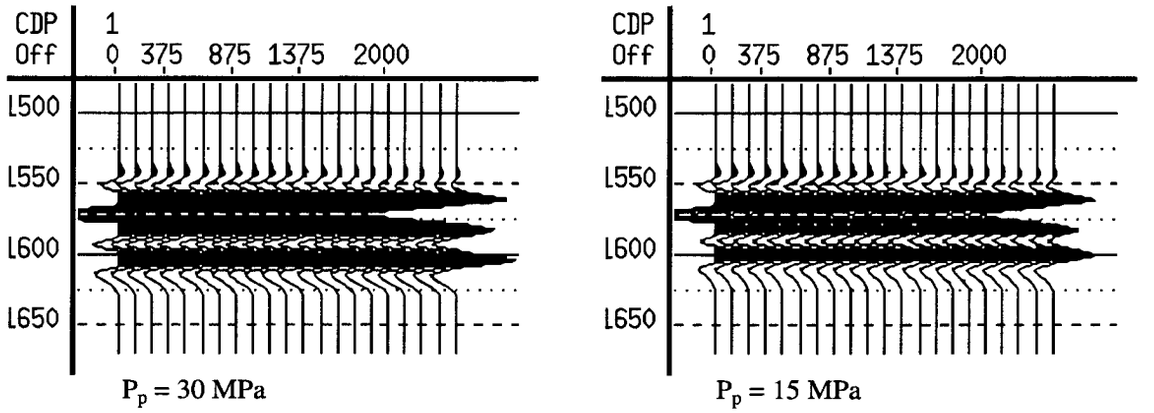

Figure 4.13: Synthetic CDP gathers showing offset (m) versus time (ms) over a Gulf Coast sand for pore pressures of 30 MPa (left) and 15 MPa (right). Both cases have 80% gas saturation and 20% brine saturation.

4.6 Summary and Conclusions

In the first part of this chapter, I demonstrated how the feasibility of monitoring hydrocarbon recovery can depend on the stiffness of the rock frame, even for high porosity sandstones. Rocks that are cemented at grain contacts can be twice as stiff as rocks that are poorly-cemented. Noise can obscure changes in the seismic signature when reservoir rocks exhibit this increased stiffness. In the second part of the chapter, I looked at how the velocity and reflectivity change in a Gulf Coast sand saturated with several fluids. When the sand is saturated with a stiff fluid, such as brine or gas-free oil, the amplitudes of the seismic reflection are smaller than for live oil or gas saturated rocks. I also show that the

AVO signature for live oil saturated sand is quite similar to the same sand having a patchy distribution of 65% gas and 35% brine. However, AVO analysis does provide a means to distinguish between highly compressible fluids, like gas and live oil, and fluids with low compressibility, like brine. In the last section of the chapter, I demonstrated how pore pressure depletion can alter the velocity and reflectivity in a gas sand. In this case, lowering the pore pressure of an uncemented sand increased V_P by 11% to 18%. The velocity increase resulted in diminished amplitudes at the top and base of the gas sand, and the reflection at the base of the sand occurred 4 ms earlier.

The results presented in this chapter demonstrate the data needs for performing feasibility and AVO studies. It is important to understand not only the rock frame stiffness, but also the response of the rock frame to changing effective pressure. The stiffness can be derived from laboratory measurements or inversion of well logs, but the pressure response requires laboratory measurements on core samples. Knowledge of the fluid properties is also important. If no measurements on fluid compressibities and densities are available, they can be calculated using the relationships provided by Batzle and Wang (1992) if you know the fluid types (e.g. gas gravity, oil gravity, gas-oil ratio, and brine salinity) and the temperature and pressure. These rock and fluid properties provide a basis to investigate how fluid substitution and pore pressure changes alter the seismic signature of a reservoir.

4.7 Acknowledgments

I would like to thank Norsk Hydro for providing the reservoir data used as a basis for the investigation of rock frame stiffness. Additional thanks go to Amos Nur for some of the ideas I investigated and to Jack Dvorkin for useful discussions. This work was supported by NSF Grant No. OCE-9401010 and the Stanford Rock Physics and Borehole Geophysics Project.

4.8 References

Aki, K., and Richards, P.G., 1980, Quantitative seismology, theory and methods: W.H. Freeman and Co.

Batzle, M. and Wang, Z., 1992, Seismic properties of pore fluids: Geophysics, **57**, 1396–1408.

Blangy, J.P., 1992, Integrated seismic lithologic interpretation: The petrophysical basis, Ph.D. Dissertation, Stanford University.

Claerbout, J.F., 1985, Fundamentals of geophysical data processing: Blackwell Scientific Publications.

Domenico, S. N., 1976, Effect of brine-gas mixture on velocity in an unconsolidated sand reservoir: Geophysics, **41**, 882–894.

Domenico, S. N., 1977, Elastic properties of unconsolidated porous sand reservoirs: Geophysics, **42**, 1339–1368.

Dvorkin, J. and Nur, A., 1996, Elasticity of high-porosity sandstones: Theory for two North Sea datasets: Geophysics, **61**, 1363–1370.

Gassmann, F., 1951, Elastic waves through a packing of spheres: Geophysics, **16**, 673–685.

Hill, R., 1963, Elastic properties of reinforced solids: Some theoretical principles: Journal of the Mechanics and Physics of Solids, **11**, 357–372.

Lumley, D., Nur, A., Strandenes, S., Dvorkin, J., and Packwood, J., 1994, Seismic monitoring of oil production: A feasibility study: SEG Annual Meeting Expanded Technical Program Abstracts with Biographies, **64**, 319–322.

Reuss, A., 1929, Berechnung der fleissgrense von mischkristallen auf grund der plastizitatsbedinggung fur einkristalle: Zeitschrift fur Angewandte Mathematik und Mechanik, **9**, 49–58.

Shuey, R.T., 1985, A simplification of the Zoeppritz equations: Geophysics, **50**, 609-614.

Strandenes, S., 1991, Rock physics analysis of the Brent Group Reservoir in the Oseberg Field: Stanford Rock Physics and Borehole Geophysics Project.

Chapter 5

Identifying Patchy Saturation from Well Logs

5.1 Abstract

We examine two saturation patterns in a volume of partially saturated rock. The first one is the homogeneous pattern where the pore-fluid phases are mixed uniformly at the pore scale so that saturation is the same at any location in the volume. The second one is the patchy pattern with fully-saturated patches located next to dry patches and the global saturation in the volume remaining the same as in the first case. The scale of a patch greatly exceeds the pore scale. These two cases may be viewed as the end members of a general scenario where some patches are partially saturated.

At the same partial saturation, the effective bulk modulus of the volume may strongly depend on the saturation pattern. Therefore, determining this pattern is important for pore fluid identification from sonic and seismic, and for forward modeling (fluid substitution). Patchy saturation has been observed in the lab. A question remains whether it exists in situ.

We show that by analyzing the dynamic Poisson's ratio, it is possible to identify the saturation pattern in soft rocks whose acoustic properties are very sensitive to the way fluid is distributed in the pore space. By applying this method to a well log where both compressional- and shear-wave velocities are available, we show that patchy saturation is likely to exist in situ.

5.2 Introduction and Problem Formulation

5.2.1 Fluid Substitution

Theoretical pore-fluid substitution is a means of predicting the sonic and seismic signatures of a reservoir as a function of saturation and pore-fluid properties. Typically, the in-situ (log) measured elastic properties of a rock are used to calculate the elastic moduli of the dry frame. Then this dry frame is theoretically re-saturated with pore fluids of different properties (changed, for example, by pressure and temperature variations) and/or at different saturations.

Consider a region of rock where both P- and S-wave velocities (V_P and V_S, respectively) are available. If this region is sufficiently smaller than the wavelength, it can be treated as an effective medium where wave velocities are related to the effective bulk (K_{Sat}) and shear (μ_{Sat}) moduli as:

$$\begin{aligned} K_{Sat} &= \rho(V_P^2 - \tfrac{4}{3}V_S^2)\,, \\ \mu_{Sat} &= \rho V_S^2\,, \end{aligned} \tag{5.1}$$

where ρ is the bulk density. According to Gassmann (1951), the dry-frame bulk and shear elastic moduli (K_{Dry} and μ_{Dry}, respectively) are

$$K_{Dry} = K_{Sat}\frac{\phi K_o + (1-\phi)K_f - K_f K_o/K_{Sat}}{\phi K_o - (1+\phi)K_f + K_f K_{Sat}/K_o}\,, \tag{5.2}$$

$$\mu_{Dry} = \mu_{Sat} = \mu\,, \tag{5.3}$$

where ϕ is porosity, and K_o and K_f are the bulk moduli of the mineral phase and pore fluid, respectively.

The inverse of Equation 5.2 is

$$K_{Sat} = K_{Dry}\frac{\phi K_o - (1+\phi)K_f + K_f K_o/K_{Dry}}{\phi K_o + (1-\phi)K_f - K_f K_{Dry}/K_o}\,. \tag{5.4}$$

Approximate fluid substitution equations for the case where only P -wave velocity is available (Mavko et al., 1995) are given in the Appendix.

An implicit assumption contained in Equations 5.2-5.4 is that pore fluid's effect on the rock's elasticity can be represented by a single parameter which is the bulk modulus

of the pore fluid. Pore fluid acts on the rock frame via pore pressure. Therefore, the above assumption is satisfied if, at a given time moment, the wave-induced fluctuations of pore pressure are the same throughout the entire volume of rock under consideration. This condition makes the applicability of Gassmann's fluid substitution equations scale- and frequency-dependent. Specifically, at ultrasonic frequencies where oscillation period is very small, fluctuations of pore pressure do not have time to equilibrate even within a single pore (e.g., Mavko and Jizba, 1991). This local-flow (or squirt-flow) effect is negligible at sonic and seismic frequencies, unless pore fluid is very viscous (Dvorkin et al., 1995) or the permeability is extremely low (as in low-porosity shales, Liu et al., 1994). The same is true for the Biot (1956) mechanism.

If Gassmann's equations are applicable and rock contains more than one pore-fluid phase, the condition of the equilibration of pore pressure fluctuations leads to using the isostress Reuss (1929) average to obtain the effective bulk modulus of the pore fluid. For example, if liquid-phase saturation is S and the rest of the pore space is filled with gas, the effective bulk modulus is

$$K_f^{-1} = SK_l^{-1} + (1-S)K_g^{-1}\,, \tag{5.5}$$

where K_l and K_g are the bulk moduli of the liquid and gas, respectively.

5.2.2 Homogeneous and Patchy Saturation

The characteristic length l of equilibration of pore-pressure fluctuations (length of diffusion) is related to diffusivity D and frequency f as

$$l = \sqrt{D/f}\,, \tag{5.6}$$

where

$$D = \frac{\kappa F}{\eta\phi}, \quad \frac{1}{F} = \frac{1}{K_f} + \frac{1-\phi-K_{Dry}/K_o}{\phi K_o}\,, \tag{5.7}$$

κ is rock permeability, and is η fluid viscosity (Dvorkin and Nur, 1993).

Consider a pure quartz Fontainebleau sandstone sample of 13.6% porosity, 670 mD permeability, and the dry-frame bulk modulus of 23.7 GPa (Lucet, 1989), filled with water.

Its diffusivity, according to Equation 5.7, is 11 m^2/s. Then the characteristic length of diffusion is 3.3 cm at 10 kHz. It is clear now that at logging frequencies, the wave-induced pore pressure fluctuations will equilibrate within a single pore.

Consider next a homogeneous volume of partially-saturated rock whose size exceeds the characteristic length of diffusion at logging frequencies. Then, if liquid and gas in this volume are distributed homogeneously (i.e., at saturation S , every pore-size volume contains S volumetric parts of liquid and $(1-S)$ volumetric parts of gas), the isostress Equation 5.5 is still applicable to finding K_f in Equations 5.2-5.4.

The other extreme in pore-fluid distribution is the patchy arrangement where liquid is located in fully-saturated patches larger than the characteristic length of diffusion, and is surrounded by dry patches (Figure 5.1). Now pore pressure fluctuations will not equilibrate between the dry and saturated regions (except in a boundary layer between them); the patches will be "sealed" from each other. Therefore, Equation 5.4 gives the upper-bound estimate for the effective bulk modulus of a fully-saturated patch (with $K_f = K_l$) if we use the assumption that the patch is hydrodynamically disconnected from the dry region. The same equation, but with $K_f = K_g$, can be used to estimate the effective bulk modulus of a dry patch.

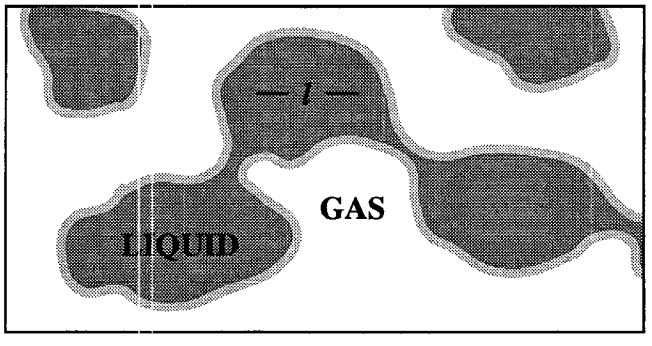

Figure 5.1: Schematic view of patchy saturation.

Because the shear modulus of rock is not affected by pore fluid, it is the same for dry and saturated patches. Also, the volumetric fraction of the saturated patches in the volume of rock under consideration is S and that of the dry patches is $(1-S)$. We take advantage of these two facts and use Hill's (1963) equation to find the effective bulk modulus K_{SatP}

of the volume, independent of the shape of the patches:

$$(K_{SatP}+\frac{4}{3}\mu)^{-1} = S(K_1+\frac{4}{3}\mu)^{-1} + (1-S)(K_2+\frac{4}{3}\mu)^{-1}\,, \tag{5.8}$$

where K_1 and K_2 are the bulk moduli of the liquid- and gas-saturated rock, respectively:

$$\begin{aligned} K_1 &= K_o\frac{\phi K_{Dry}-(1+\phi)K_l K_{Dry}/K_o+K_l}{(1-\phi)K_l+\phi K_o-K_l K_{Dry}/K_o}\,, \\ K_2 &= K_o\frac{\phi K_{Dry}-(1+\phi)K_g K_{Dry}/K_o+K_g}{(1-\phi)K_g+\phi K_o-K_g K_{Dry}/K_o}\,. \end{aligned} \tag{5.9}$$

If V_P and V_S are available at saturation S , K_{Dry} can be found from Equations 5.8 and 5.9 as:

$$K_{Dry} = (-B+\sqrt{B^2-4AC})/2A\,, \tag{5.10}$$

where

$A = cq+M(bq+cf)$, $B = pc+dq-M(aq-bp-df+ce)$, $C = dp-M(ap+de)$;

$a = S[(1-\phi)K_l+\phi K_o]$, $b = SK_l/K_o$, $c = \phi K_o-(1+\phi)K_l-K_l\mu/K_o$,

$d = K_lK_o+(1-\phi)\mu K_l+\phi\mu K_o$, $e = (1-S)[(1-\phi)K_g+\phi K_o]$, $f = (1-S)K_g/K_o$,

$p = K_gK_o+(1-\phi)\mu K_g+\phi\mu K_o$, $q = \phi K_o-(1+\phi)K_g-K_g\mu/K_o$;

$M = \rho V_P^2$, $\mu = \rho V_S^2$.

μ is the (independent of saturation) shear modulus of the rock, and M is the M-modulus defined as the product of the bulk density and P-wave velocity squared. Approximate "patchy" fluid substitution equations for the case where only P-wave velocity is available are given in the Appendix.

5.2.3 Existence of Patches

Consider a volume of rock that consists of several sand patches with clay content varying slightly among them. These clay-content variations may have a small effect on the dry-frame elastic moduli but dramatically affect permeability (such set of samples has been experimentally investigated by Yin, 1993) and, therefore, capillary pressure curves. Knight et al. (1997) show that in a state of capillary equilibrium, this elastically (almost) homogeneous volume may have heterogeneous (patchy) saturation pattern.

Chatenever and Calhoun (1952) present a visual proof that patches do form in an oil-water system during a laboratory flooding experiments in a glass bead pack. Cadoret (1993) shows X-ray tomographic images of liquid patches.

It is important to mention that the velocity-saturation behavior in a patchy system dramatically differs from that in a homogeneous system. Knight et al. (1997) theoretically estimate this difference by calculating velocity first in the system with the patchy distribution of clay content and then in the same system where all the patches are homogeneously mixed (Figure 5.2a). This theoretical velocity behavior is qualitatively similar to the experimental results in Figure 5.2b (Cadoret, 1993). Knight and Nolen-Hoeksema (1990) experimentally observed "patchy" velocity-saturation behavior thus indirectly confirming the existence of saturation patches. Therefore, patchy saturation does exist in laboratory conditions. A question remains whether it exists in situ.

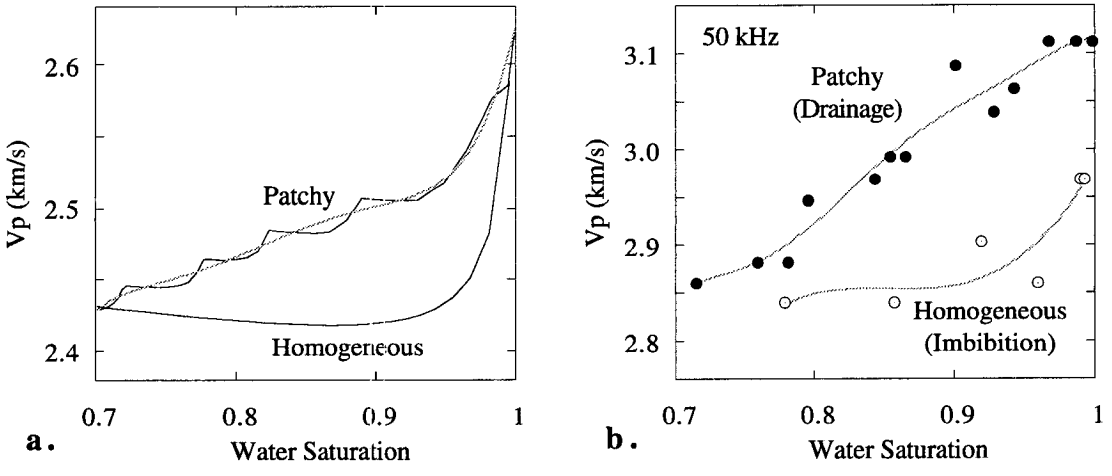

Figure 5.2: Velocity versus water saturation for homogeneous and patchy patterns. a. Theoretical results (Knight et al., 1997) for a sand-clay system. Patchy curve is not smooth due to the finite number of patches. It is smoothed by a polynomial fit. b. Experiments of Cadoret (1993) at 50 kHz on a carbonate sample of 30% porosity. The lines are polynomial fits.

5.2.4 Importance of Saturation Pattern Identification

The nature of oil/gas distribution in a pay zone affects the estimates of recoverable reserves, relative permeability, and dry-frame elastic properties. The latter are needed for the "fluid substitution" procedure where the velocities in a rock with a new, hypothetical, fluid are

calculated from those measured in the rock with the known fluid.

The patchy arrangement of ground water is probably common in undersaturated aquifer zones. To determine the details of such patchy arrangements is important for ground water flow calculations and watertable monitoring.

Industrial groundwater contaminants in the shallow subsurface may occur in patches, or may be evenly dispersed in the pore space. Determining the arrangement type will help select the remediation technique.

5.2.5 Problem Formulation

To this end we pose a problem to identify the saturation pattern from well logs. The input at every depth includes: *P*- and *S*-wave velocity, bulk density, porosity, and saturation. We also require the bulk modulus of the mineral phase of the rock, as well as the bulk moduli of the liquid and gas phases.

5.3 Saturation Pattern, Velocity and Poisson's Ratio

Consider a dry Ottawa sand sample whose bulk and shear moduli at 10 MPa effective pressure are 1.75 and 1.72 GPa, respectively (Han, 1986). Porosity is 33%, and the bulk modulus of the pure-quartz solid phase is 38 GPa (Carmichael, 1990). The sample is saturated with brine and gas whose bulk moduli are 2.55 and 0.018 GPa, respectively. These numbers correspond to brine of salinity 30,000 ppm and methane at 10 MPa pore pressure and 50°C temperature (Batzle and Wang, 1992).

We use Equations 5.4, and 5.8-5.9 to calculate *P*- and *S*-wave velocities for the homogeneous and patchy saturation patterns at varying saturation (Figure 5.3a). Poisson's ratio (ν) is related to the bulk (K) and shear (μ) moduli as

$$\nu = \frac{1}{2}\frac{3K/\mu - 2}{3K/\mu + 1}. \tag{5.11}$$

It is plotted versus saturation (according to the saturation pattern) in Figure 5.3b.

If saturation is homogeneous, the compressibility of the brine-gas mixture is very close to that of gas for almost all saturations. Only when water saturation approaches unity does

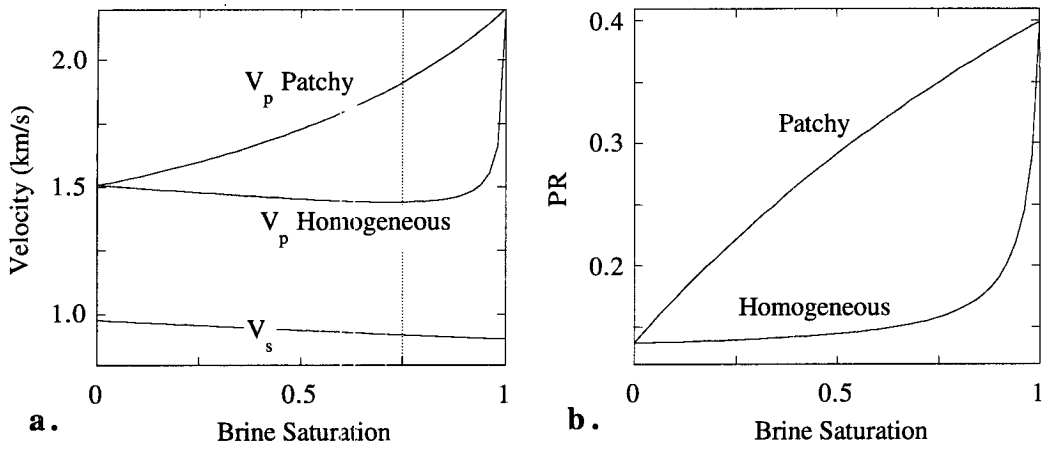

Figure 5.3: Ottawa sand. Compressional-wave velocity (a) and Poisson's ratio (b) versus brine saturation for homogeneous and patchy patterns. Shear-wave velocity is pattern-independent.

the compressibility of the mixture sharply decrease and approach that of brine. In this case, the bulk modulus of the rock is approximately constant for almost all saturations and sharply increases as the rock becomes fully saturated. At the same time, the density of the rock steadily increases with increasing saturation resulting in a slight velocity decrease with increasing saturation. Only at a very high saturation does the velocity approach its value in the fully saturated rock. The situation is completely different if saturation is patchy. In this case the compressional-wave velocity steadily increases with increasing saturation. The difference between the "homogeneous" and "patchy" Poisson's ratios is even more drastic than that for the velocity.

We intend to take advantage of these differences in identifying the saturation pattern from measurements. Let us assume, for example, that the Ottawa sand sample has patchy saturation and, therefore, the measured compressional- and shear-wave velocities are 1.91 and 0.92 km/s at 75% saturation (Figure 5.3a). Also, the measurements at other saturations are not available, and neither are the dry-frame elastic moduli of the rock. Given the above measurements and the properties of the mineral and pore-fluid phases, we can calculate the dry-frame elastic properties and velocities using Equation 5.2 for the homogeneous saturation inversion or Equation 5.10 for the patchy saturation inversion.

The appropriate inversion technique (patchy in this case) gives the correct dry-frame

velocity of 1.51 km/s at 75% saturation. The inappropriate (homogeneous) inversion technique gives 1.89 km/s at the same saturation (Figure 5.4a). We know, from the velocity and porosity measurements, that we are dealing with high-porosity soft rock. Therefore, we conclude, based on existing data for such rocks (Figure 5.5a), that both dry-frame velocity values are possible within the given porosity and effective pressure range. Clearly, compressional-wave velocity alone cannot be a reliable indicator of whether the chosen inversion technique is appropriate or not.

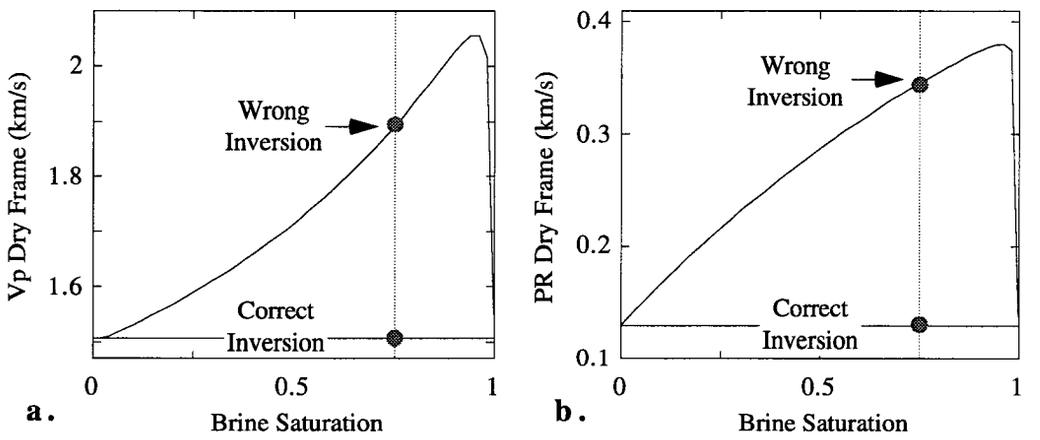

Figure 5.4: Ottawa sand. Dry-frame velocity (a) and Poisson's ratio (b) versus brine saturation as obtained from measurements at partial saturation using "homogeneous" and "patchy" inversions.

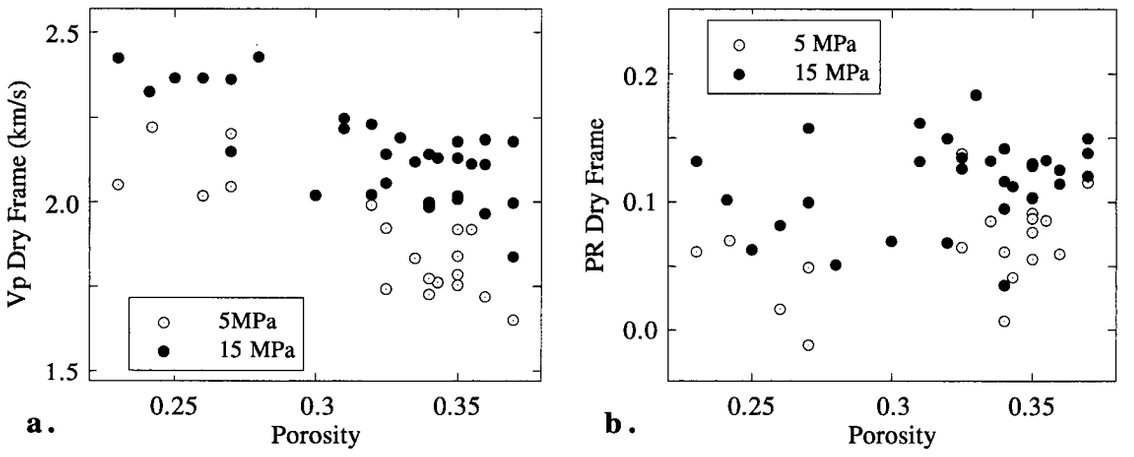

Figure 5.5: Dry-rock velocity (a) and Poisson's ratio (b) versus porosity in unconsolidated North Sea sands at the effective pressure of 5 MPa and 15 MPa (Blangy, 1992).

Let us add the (saturation pattern-independent) shear-velocity, which is 0.92 km/s at 75% saturation. From this datapoint, and using Equation 5.3, we find that the dry-frame value of this velocity is 0.98 km/s. Next we calculate the dry-frame Poisson's ratio and arrive at 0.13 for "patchy" inversion and 0.35 for "homogeneous" inversion. Now our conclusion can be very definite. Spencer et al. (1994) report that many unconsolidated sands from the Gulf of Mexico have dry-rock Poisson's ratios near 0.18, while other Gulf Coast reservoirs have these values as low as 0.115. Only on several occasions (among a large number of rock samples) does the dry-rock Poisson's ratio exceed 0.2, with the maximum value 0.237. To facilitate this point, we plot dry-rock Poisson's ratios versus porosity (Figure 5.5b) for a suite of unconsolidated North Sea sands (Blangy, 1992) at effective pressure values which bracket 10 MPa. Again, these values do not exceed 0.2.

The conclusion is clear: the saturation pattern in the Ottawa sand under consideration is patchy because the "homogeneous" inversion failed to give a reasonable value for the dry-frame Poisson's ratio.

5.4 Saturation Pattern from Well Logs

5.4.1 Method

To this end we propose to use the dry-frame Poisson's ratio calculated from well-log curves as an indicator of the saturation pattern. The routine follows. At every depth where the required data are available (see the problem formulation above):

1. Find the dry-frame Poisson's ratio from Equation 5.11 where the velocities are obtained from the "patchy" inversion according to Equation 5.10.

2. If this inversion gives unreasonable values for the Poisson's ratio, the assumption that saturation is patchy is wrong, and, therefore, saturation is homogeneous.

3. Find the dry-frame Poisson's ratio from Equation 5.11 where the velocities are obtained from the "homogeneous" inversion according to Equations 5.2-5.3.

4. If this inversion gives unreasonable values for the Poisson's ratio, the assumption that saturation is homogeneous is wrong, and, therefore, saturation is patchy.

Of course, it may happen that both inversion techniques give reasonable, or both unreasonable, Poisson's ratio values. The first result means that the proposed method failed to identify the saturation pattern (see example below). In the second case additional analysis or data quality check are required.

5.4.2 Synthetic Well Logs

We test this method on synthetic well logs. The first log was created based on laboratory measurements of acoustic velocities and porosity in a suite of soft dry rocks from the Troll Field in the North Sea (Blangy, 1992). The effective pressure is 10 MPa. The liquid and gas properties are the same as in the example above. We assumed saturation values and saturation patterns versus depth (Figure 5.6a) and calculated the "measured" velocities accordingly (Figure 5.6b).

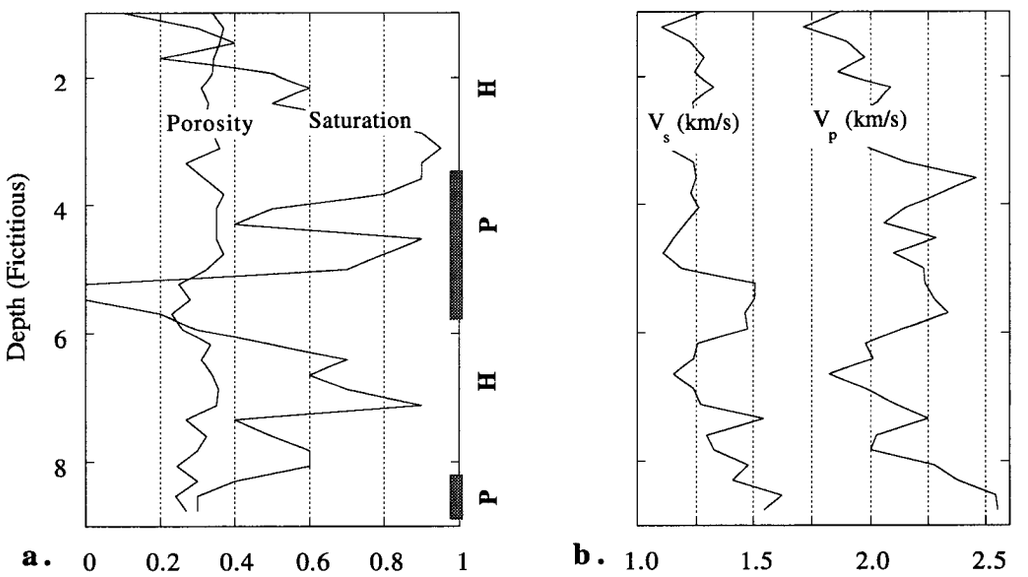

Figure 5.6: Synthetic well log. a. Porosity and saturation versus depth. Bold vertical lines show depth intervals with patchy (P) saturation. The rest of the interval has homogeneous (H) saturation. b. Velocities calculated from dry-rock velocities and the assumed saturation values and patterns.

We calculate the dry-frame Poisson's ratio using the assumption that saturation is patchy in the whole depth interval (Figure 5.7a). Obviously, the calculated Poisson's ratio may be quite unrealistic at some depth intervals. In order to identify saturation patterns, we

clip the calculated Poisson's ratio curve leaving out unreasonable negative values (Figure 5.7b). What is left most likely corresponds to the patchy saturation pattern since the patchy inversion technique was used here. The rest of the depth interval corresponds to the homogeneous pattern. The intervals of different saturation patterns thus identified exactly correspond to those in the original log, except for two points at the depth of about 1.7.

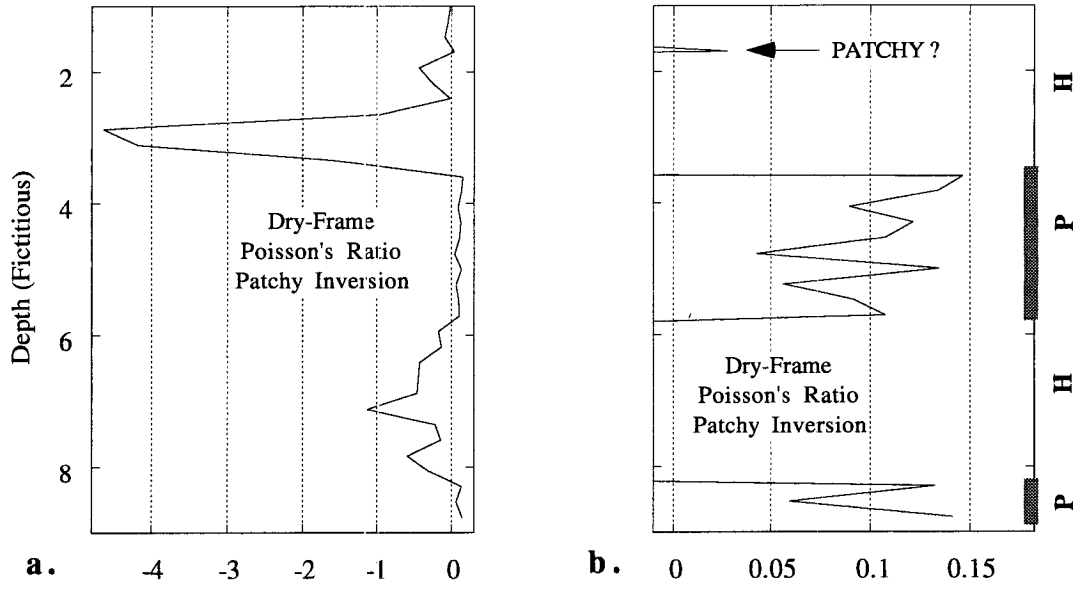

Figure 5.7: Synthetic well log: patchy inversion for the dry-frame Poisson's ratio. a. The whole range of the Poisson's ratio variation. b. Unreasonable Poisson's ratio values clipped. Bold vertical lines show depth intervals with patchy saturation.

If the saturation pattern is not identified, errors in calculating the dry-frame bulk modulus and P -wave velocity may be large (Figure 5.8). As a result, fluid substitution may give wrong seismic velocities and Poisson's ratios in gas-saturated intervals.

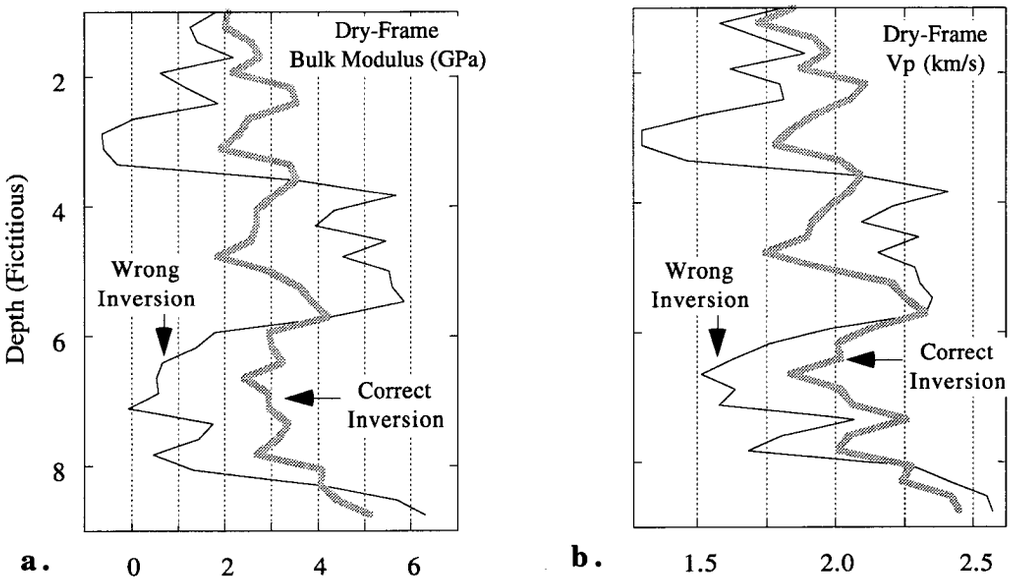

Figure 5.8: Synthetic well log. a. Dry-frame bulk modulus. b. Dry-frame velocity.

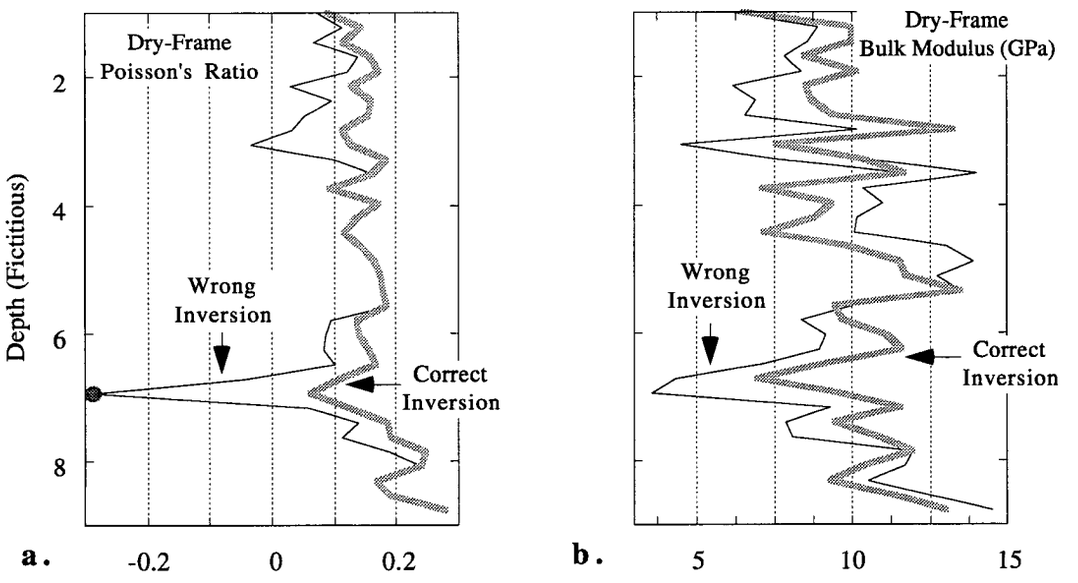

Figure 5.9: Synthetic well log for fast rocks. a. Dry-frame Poisson's ratio. One unreasonably negative value is shown as filled symbol. b. Dry-rock bulk modulus.

The proposed method works well in soft formations because their elastic coefficients are extremely sensitive to the compressibility of the pore fluid. This may not be the case in a faster formation. Consider, for example, high-porosity samples from the Oseberg Field in the North Sea (Strandenes, 1991). These rocks are quartz- and clay-cemented at the grain contacts, which results in high acoustic velocities at high porosity. As in the previous example, we create a synthetic well log based on the laboratory measurements and repeat the inversion process. However, in this case the wrong inversion for the dry-frame Poisson's ratio gives an unreasonably negative value only at one point (Figure 5.9a). Otherwise, it is impossible to determine the saturation pattern from the Poisson's ratio inversion. Still, the calculated dry-rock bulk modulus strongly depends on the saturation pattern assumed for inversion (Figure 5.9b), but the errors are not as large as in the soft-formation case.

5.4.3 Field Example

We examine open-hole logs obtained in a vertical well that penetrates unconsolidated and very soft (Figure 5.10a) gas sands. The frequency of the *P*-wave tool was low which ensured the depth of penetration consistent with that of the *S*-wave, deep resistivity, and density tools. We choose a relatively clean gas interval. The volumetric clay content, as estimated from the gamma-ray curve (Figure 5.10c) by linearly interpolating between the clean sand level and the shale level (e.g., Dewan, 1983), is less than 10% and is consistent with that measured on a few selected cores. Porosity (Figure 5.10e) and brine saturation (Figure 5.10f) were calculated by simultaneously solving the bulk density equation

$$\rho = (1-\phi)\rho_s + \phi[S\rho_l + (1-S)\rho_g]\,, \tag{5.12}$$

and Archie's equation with the Humble formation factor formula for sands (Schlumberger, 1989):

$$S = \sqrt{\frac{0.81}{\phi^2}\frac{R_w}{R_t}}\,, \tag{5.13}$$

where ρ_s is the mineral-phase density; ρ_l and ρ_g are the densities of the brine and gas, respectively; R_w is the resistivity of the formation water; and R_t is the measured formation

(deep) resistivity. The density of the mineral phase was calculated from the clay content C by assuming that the rest of the mineral phase is pure quartz:

$$\rho_s = (1-C)\rho_q + C\rho_c\,, \tag{5.14}$$

where ρ_q and ρ_c are the densities of quartz and clay, respectively. The resulting porosity curve is consistent with the core values.

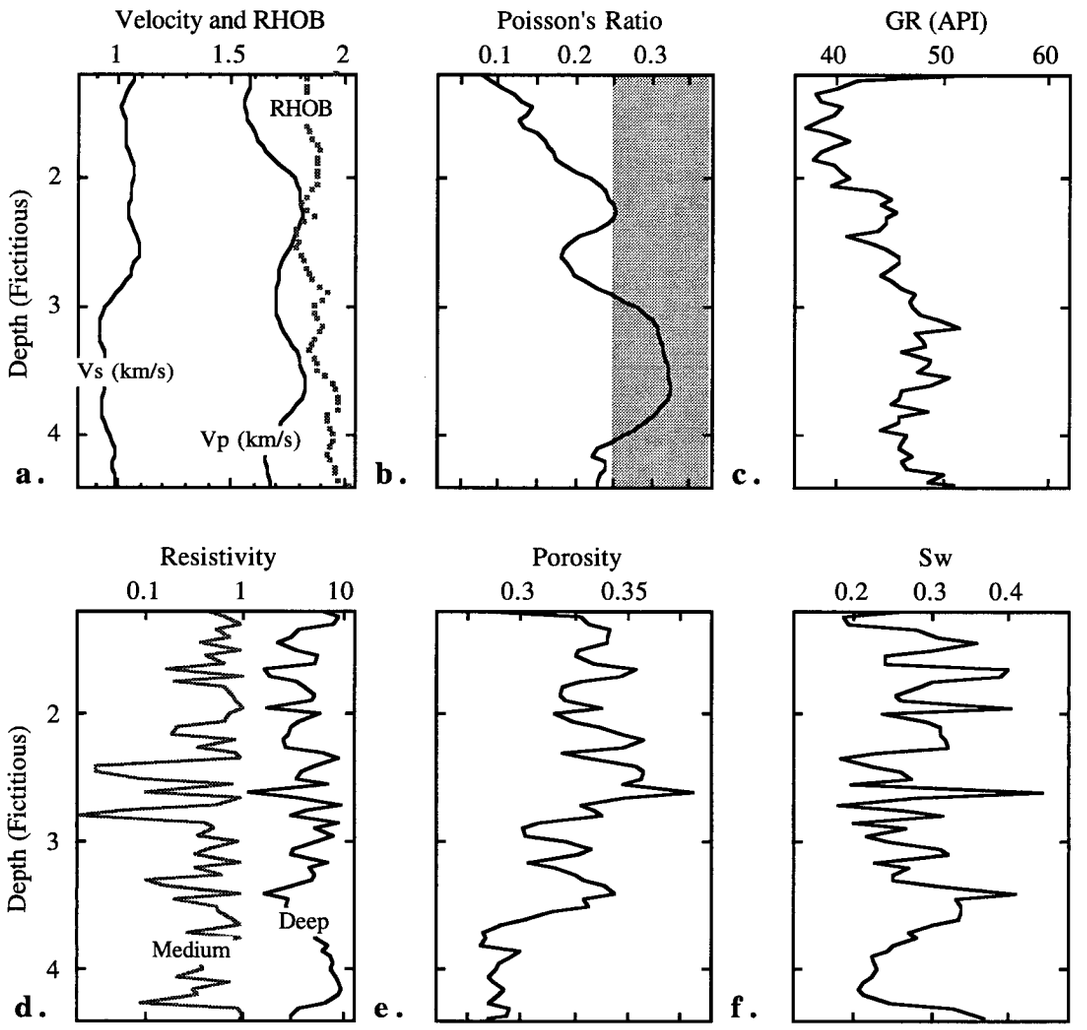

Figure 5.10: Open-hole logs. Compressional- and shear-wave velocities (a); Poisson's ratio from the velocities (b); gamma-ray (c); clay content from gamma-ray (d); porosity (e); and brine saturation (f). In the "b" graph the shaded area corresponds to unreasonably high (at partial saturation) Poisson's ratio values. Symbols in "d" and "e" indicate core data.

The bulk modulus of the solid phase (needed for fluid substitution) was calculated from those of quartz and clay using Hill's (1952) average:

$$K_o = 0.5(1-C)K_q + CK_c + [(1-C)/K_q + C/K_c]^{-1}\,, \tag{5.15}$$

where K_q and K_c are the bulk moduli of quartz and clay, respectively. The bulk modulus and density of quartz are chosen as 38 GPa and 2.65 g/cm^3, respectively (Carmichael, 1990). The bulk modulus and density of clay are chosen as 21 GPa and 2.58 g/cm^3, respectively. These clay moduli are calculated from the velocity values derived by extrapolating the experimental linear velocity-porosity-clay relations obtained by Tosaya (1982) for clay-bearing Gulf sandstones. The density was calculated from the measured density of samples with high clay content, and known porosity and mineralogy. The brine and gas bulk moduli (2.88 and 0.0365 GPa, respectively) and densities (1.053 and 0.122 g/cm^3, respectively) were calculated using equations of Batzle and Wang (1992), according to the in situ salinity, pressure and temperature.

A question remains whether Equation 5.13 is applicable to estimating saturation from resistivity not only for the homogeneous but also for patchy saturation. We are not aware of any experimental data to refute or support this statement. Still, we justify the use of Archie's equation in both saturation regimes based on the following speculation. Equation 5.13 can be rewritten as

$$R_t = \frac{0.81R_w}{(S\phi)^2}\,, \tag{5.16}$$

which means that the resistivity is a function of $S\phi$ – the volumetric fraction of conductor (brine) in the total rock volume. Then Archie's equation is justified for the patchy saturation if we assume that the function in Equation 5.16 is independent of how the conductor is distributed in the volume.

To calculate the dry-frame Poisson's ratio, we sequentially use the "homogeneous" and "patchy" inversions. Both curves are given in Figure 5.11a. A clear indirect indication of patchy saturation between the depths of 3 and 4 (fictitious units) is the unreasonably high dry-frame Poisson's ratio obtained from the "homogeneous" inversion. These values exceed 0.25 which is an extreme even for "dirty" unconsolidated sands (Spencer et al.,

1994). At the same time, the "patchy" dry-frame Poisson ratio only slightly exceeds the threshold of 0.25 and remains, generally, within reasonable limits. Its values, although high, appear to be more realistic than those given by the homogeneous inversion. A possible reason for these high values is that "dry" patches in the patchy saturation domain are likely to be not completely dry (Knight et al., 1997). Our inversion technique can be easily changed to take this fact into account. However, this will introduce non-measurable free parameters which should be avoided in any practical application.

Another candidate for patchy saturation is the section between the depths of 2 and 2.5. In this case we lower the reasonable-value threshold for the dry-frame Poisson's ratio from 0.25 to 0.2. The latter value seems to be appropriate in this interval (where the gamma-ray readings are smaller than in the deeper "patchy" interval, as shown in Figure 5.11b) because Poisson's ratio in sands, in general, decreases with the decreasing clay content. The latter effect has been established, based on laboratory core measurements, by Spencer et al. (1994). It also follows from the earlier laboratory experiments by Han (1986) and in-situ data analyzed by Castagna et al. (1993).

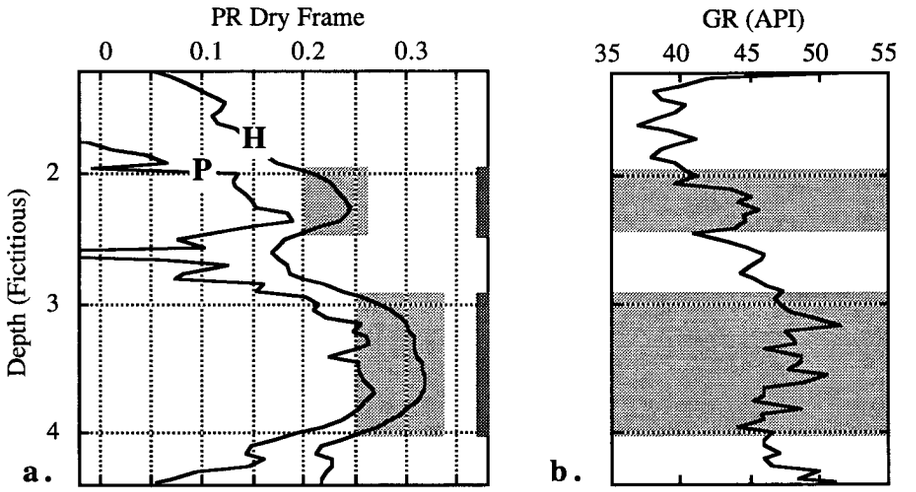

Figure 5.11: a. Dry-frame Poisson's ratio versus depth from the homogeneous ("H") and patchy ("P") inversion. Vertical bars indicate patchy saturation zones. b. gamma ray versus depth. One fictitious depth unit corresponds to 20 ft.

Notice that it is possible to delineate patchy-saturation zones directly from the measured Poisson's ratio versus depth plot (Figure 5.10b) without calculating the dry-frame Poisson's ratio. Indeed, brine saturation in the interval under consideration does not exceed

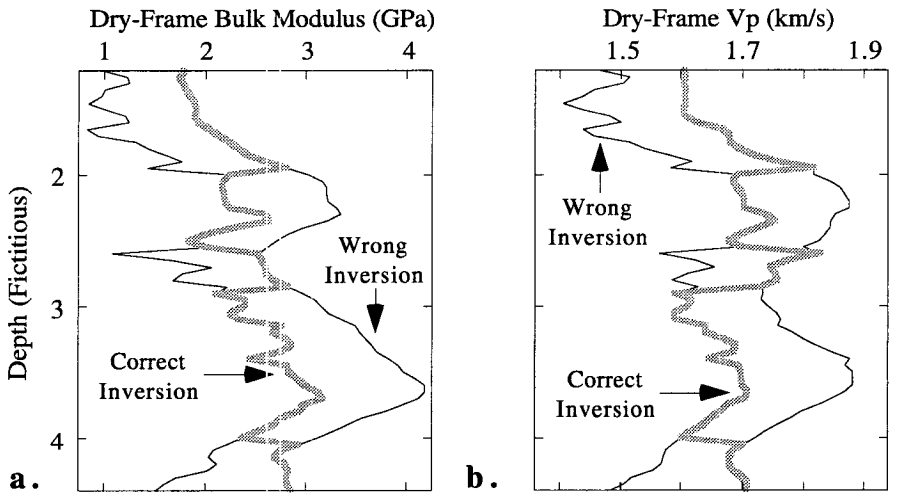

Figure 5.12: Dry-frame bulk modulus (a) and compressional-wave velocity (b) versus depth (the field example). Thin lines are from wrong inversion ("homogeneous" in the patchy region and "patchy" in the homogeneous region). Bold lines are from correct inversion. One fictitious depth unit corresponds to 20 ft.

40%. If saturation is homogeneous, the Poisson's ratio cannot exceed 0.25 for saturations below 90% (Figure 5.3b). Therefore, by selecting 0.25 as a threshold, we conclude that the interval between the depths of 3 and 4 (Figure 5.10b) has patchy saturation. In other words, if the measured Poisson's ratio in partially-saturated sands exceeds a certain threshold, saturation cannot be homogeneous. This threshold may vary depending on clay content but should be no larger than 0.25.

5.5 Discussion

5.5.1 Implications

If the saturation pattern is assumed to be homogeneous (common fluid-substitution approach), the errors in dry-frame bulk modulus calculated from well logs may be very large, especially in soft formations. The errors (the field example above) may exceed 50% (Figure 5.12a). The errors in the dry-frame compressional-wave velocity will be great as well (Figure 5.12b). Such errors have to be taken into account, as they may definitely affect seismic interpretation for direct hydrocarbon indication.

The existence of patchy saturation opens an avenue for accurately estimating gas saturation in situ. Consider, for example, Figure 5.3. If saturation is homogeneous, the velocity is practically insensitive to gas saturation. On the other hand, if it is patchy, we have a clear velocity-saturation trend.

5.5.2 Patch Size

We use Equation 5.6 and take average porosity and permeability as 0.32 and 500 mD, respectively, and brine's viscosity as 1 cPs (the field example). Then at 2 kHz we arrive at 5 cm as the lower bound for the patch size.

Hill's relationship (Equation 5.8) is a static effective-medium equation. Therefore, a patch has to be sufficiently smaller than the wavelength to make this equation applicable. The wavelength in this example is about 1 m. Therefore, the upper limit for the patch size, if taken as a quarter of the wavelength, is 25 cm.

5.5.3 Idealized End Members

Finally, we emphasize that both homogeneous and patchy saturation models, as presented here, have to be treated as idealized end members (or bounds) for a realistic situation. The fact is that where one of these two fluid substitution methods fails to give reasonable elastic moduli values for the dry frame, the other may do so.

To this end we suggest that in unconsolidated partially-saturated sands two fluid substitution techniques – homogeneous and patchy – be used to calculate the dry-rock elastic moduli from well logs. If the homogeneous inversion gives dry-rock Poisson's ratios which exceed 0.2 - 0.25, and at the same time the patchy inversion gives lower and more reasonable values, the interval is likely to be patchy-saturated. Then the dry-rock bulk moduli have to be calculated accordingly.

We recommend to use both techniques for bounding the possible dry-rock Poisson ratio and bulk modulus values.

5.6 Conclusions

- At a fixed partial saturation, two saturation patterns may exist in a rock volume: the homogeneous pattern where saturation is the same at any location in the volume, and the patchy pattern where a fully-saturated patch may be surrounded by a dry region.
- It is important to identify the saturation pattern in order to correctly compute the dry-rock elastic moduli from well logs.
- A synthetic example and a case study show that the identification method where the dry-rock Poisson's ratio is computed sequentially based on the assumptions that the pattern is patchy, and that it is homogeneous, works in unconsolidated sands.
- We recommend the routine use of this method to bound the dry-rock elastic moduli.

5.7 Acknowledgement

The idea of quantifying the patchy saturation pattern belongs to Gary Mavko. This work was supported by DOE (Office of Basic Energy Sciences) and by the Stanford Rock Physics and Borehole Geophysics Consortium.

5.8 References

Batzle, M., and Wang, Z., 1992, Seismic properties of pore fluids: Geophysics, **57**, 1396-1408.

Blangy, J.P., 1992, Integrated seismic lithologic interpretation: The petrophysical basis: Ph.D. thesis, Stanford University.

Biot, M. A.,1956, Theory of propagation of elastic waves in fluid saturated porous solid. I. Low frequency range: J. Acoust. Soc. Am., **28**,168-191.

Cadoret, T., 1993, Effet de la saturation eau/gaz sur les proprits acoustiques des roches: Ph.D. thesis, University of Paris.

Carmichael, R.S., 1990, Practical handbook of physical properties of rocks and minerals: CRC Press.

Castagna, J.P., Batzle, M.L., and Kan, T.K., 1993, Rock physics – the link between rock properties and AVO response, in Offset-dependent reflectivity - theory and practice of AVO analysis, Castagna J.P., and Backus, M.M., eds.: SEG Investigations in Geophysics 8, 135–171.

Chatenever, A., and Calhoun, J.C., 1952, Visual examinations of fluid behavior in porous media – Part 1: AIME Petroleum Transactions, **195**, 149–195.

Dewan, J.T., 1983, Essentials of modern open-hole log interpretation: PennWell Books, Tulsa.

Dvorkin, J., Mavko, G, and Nur A., 1995, Squirt flow in fully saturated rocks: Geophysics, **60**, 97-107.

Dvorkin, J., and Nur A., 1993, Dynamic poroelasticity: A unified model with the squirt and Biot mechanisms: Geophysics, **58**, 524–533.

Gassmann, F., 1951, Elasticity of porous media: Uber die elastizitat poroser medien: Vierteljahrsschrift der Naturforschenden Gesselschaft, **96**, 1–23.

Han, D.-H., 1986, Effects of porosity and clay content on acoustic properties of sandstones and unconsolidated sediments: Ph.D. thesis, Stanford University.

Hill, R., 1952, The elastic behavior of crystalline aggregate: Proc. Phys. Soc. London, **A65**, 349–354.

Hill, R., 1963, Elastic properties of reinforced solids: Some theoretical principles, J. Mech. Phys. Solids, **11**, 357–372.

Knight, R., Dvorkin, J., and Nur, A., 1997, Seismic signatures of partial saturation: Geophysics, in press.

Knight, R. J. and Nolen-Hoeksema, R., 1990, A laboratory study of the dependence of elastic wave velocities on pore scale fluid distribution: GRL, **17**, 1529–1532.

Liu, X., Vernik, L., and Nur, A., 1994, Effects of saturating fluids on seismic velocities in shales: SEG Annual Meeting Expanded Technical Program Abstracts with Biographies, **64**, 1121–1124.

Lucet, N., 1989, Vitesse et attenuation des ondes elastiques soniques et ultrasoniques dans les roches sous pression de confinement: Ph.D. thesis, The University of Paris.

Mavko, G., Chan, C., and Mukerji, T., 1995, Fluid substitution: Estimating changes in V_P without knowing V_S: Geophysics, **60**, 1750–1755.

Mavko, G., and Jizba, D., 1991, Estimating grain-scale fluid effects on velocity dispersion in rocks: Geophysics, **56**,1940–1949.

Reuss, A., 1929, Berechnung der fliessgrense von mischkristallen auf grund der plastizitatbedinggung fur einkristalle: Zeitschrift fur Angewandte Mathematik und Mechanik, **9**, 49–58.

Schlumberger, 1989, Log interpretation principles/applications: Schlumberger Wireline & Testing, Houston.

Spencer, J.W., Cates, M.E., and Thompson, D.D., 1994, Frame moduli of unconsolidated sands and sandstones: Geophysics, **59**, 1352–1361.

Strandenes, S., 1991, Rock physics analysis of the Brent Group Reservoir in the Oseberg Field: Stanford Rock Physics and Borehole Geophysics Project, Stanford University.

Yin, H., 1993, Acoustic velocity and attenuation of rocks: Isotropy, intrinsic anisotropy, and stress-induced anisotropy: Ph.D. thesis, Stanford University.

Appendix Fluid Substitution Based on Compressional-Wave Velocity

A.1 Homogeneous Saturation

Mavko et al. (1995) show that instead of Equations 5.2-5.4 one can use approximate but highly accurate equations

$$M_{Dry} = M_o \frac{1-(1-\phi)M_{Sat}/M_o - \phi M_{Sat}/K_f}{1+\phi-\phi M_o/K_f - M_{Sat}/M_o}\,,$$
$$M_{Sat} = M_o \frac{\phi M_{Dry} - (1+\phi)K_f M_{Dry}/M_o + K_f}{(1-\phi)K_f + \phi M_o - K_f M_{Dry}/M_o}\,, \tag{5.17}$$

where M_{Dry}, M_{Sat}, and M_o are the M-moduli of the dry frame, partially saturated rock, and mineral phase, respectively. The M-modulus is defined as the product of the density and compressional-wave velocity squared and is related to the bulk and shear moduli as

$$M = \rho V_P^2 = K + \frac{4}{3}\mu\,. \tag{5.18}$$

A.2 Patchy Saturation

Based on Equation 5.18, Equation 5.8 can be rewritten as

$$M_{SatP}^{-1} = S M_1^{-1} + (1-S)M_2^{-1}\,, \tag{5.19}$$

where M_{SatP} is the effective M-modulus of the volume with patchy saturation, and M_1 and M_2 are the M-moduli of the liquid- and gas-saturated rock, respectively. Also, based on Equation 5.17, Equations 5.9 can be approximated by

$$M_1 = M_o \frac{\phi M_{Dry} - (1+\phi)K_l M_{Dry}/M_o + K_l}{(1-\phi)K_l + \phi M_o - K_l M_{Dry}/M_o}\,,$$
$$M_2 = M_o \frac{\phi M_{Dry} - (1+\phi)K_g M_{Dry}/M_o + K_g}{(1-\phi)K_g + \phi M_o - K_g M_{Dry}/M_o}\,. \tag{5.20}$$

By solving Equations 5.19 and 5.20 together, we find:

$$M_{Dry} = 0.5(-B + \sqrt{B^2 - 4AC})/2A\,, \tag{5.21}$$

where

$$A = cq + m(bq + cf), \quad B = pc + dq - m(aq - bp - df + ce), \quad C = dp - m(ap + de);$$
$$m = M_{Sat}/M_o, \quad a = S[(1 - \phi)K_l + \phi M_o], \quad b = SK_l/M_o,$$
$$c = \phi - (1 + \phi)K_l/M_o, \quad d = K_l, \quad e = (1 - S)[(1 - \phi)K_g + \phi M_o],$$
$$f = (1 - S)K_g/M_o, \quad p = K_g, \quad q = \phi - (1 + \phi)K_g/M_o.$$

Chapter 6

Conclusion

6.1 Summary

This thesis investigates how several rock physics principals apply to hydrocarbon recovery monitoring. I summarize these principals and the results presented in each chapter. I also provide a brief discussion of attenuation, which is not addressed in this thesis. A theme that ties all the chapters together is the role of fluid distribution on seismic wave velocities. I develop two conceptual models for fluid distribution in Chapter 2 that I carry through the other chapters.

6.1.1 Fluid Distribution Models

In Chapter 2, I presented two distinct models for fluid distribution, and I demonstrated how fluid distribution can have a significant effect on compressional wave velocity (V_P) and compressional impedance (I_P) in rocks with two or more fluid phases. The uniform fluid model is commonly used to estimate the effect of pore fluids on seismic wave velocities. In this model, I assume that the pore pressure increments induced by a passing seismic wave diffuse during a seismic period. The pore fluids are, then, relaxed, and all fluid phases experience the same stress. The iso-stress condition allows us to use the Reuss (1929) average of the bulk moduli of the pore fluid phases to calculate the bulk modulus of the fluids occupying the pore space of a given reservoir rock. The fluid modulus, the dry frame bulk modulus of the rock, the bulk modulus of the minerals making up the rock

frame, and the rock porosity are used in Gassmann's (1951) theory to model the effective saturated bulk modulus of the rock. The second model is for patchy fluid distribution. In this model, the seismically-induced pore pressure increments equilibrate within each patch, but between patches, there is not enough time for equilibration within a seismic period. The unrelaxed condition results in velocity dispersion. The effective bulk modulus of the rock with patchy saturation is computed using a relationship provided by Hill (1963) for a medium with uniform shear modulus. One important characteristic of the patchy model is that its application is independent of patch shape.

The distinction between patchy and uniform fluid behavior is one of scale. If the patches are small enough, the pore pressure increments will diffuse, and the uniform fluid model should apply. The characteristic diffusion length, l, can be estimated from:

$$l = \sqrt{\frac{\kappa K_f}{\eta f}}, \tag{6.1}$$

where κ is the permeability, K_f is the fluid bulk modulus, η is the fluid viscosity, and f is the frequency. So, if the patches are larger than l and smaller than the seismic resolution, the patchy model applies.

The results presented in this chapter show that fluid distribution can have a large impact on V_P. Knowledge of which model is appropriate in a given situation could be crucial to interpreting velocity logs, cross-well seismic, and surface seismic data. The question of when the patchy and uniform fluid models are appropriate remains unanswered. One key may be in some experimental results, such as those reported by Cadoret et al. (1992). These show that saturation history plays an important role in determining the fluid distribution. In these experiments, a more uniform distribution of fluids was achieved during imbibition processes, where the wetting phase saturation is increasing. X-ray tomography revealed that a drainage process (i.e. decreasing wetting phase saturation) resulted in a more patchy fluid distribution. The authors measured V_P at incremental steps of water saturation during both imbibition and drainage processes. The resulting values of V_P were higher during drainage than during imbibition, especially at high values water saturation. Similar velocity results were reported by Knight and Nolen-Hoeksema (1990) for drainage and imbibition processes.

Although it is commonly understood that multi-phase fluid distribution in reservoir

rocks is heterogeneous, the question remains whether these heterogeneities are on a scale large enough to affect seismic wave propagation. An area for further study is to determine whether this patchy saturation persists on a seismic scale. One way to predict this is to carry out detailed fluid flow modeling to see if fluid distributions on the scale of the diffusion length are likely.

6.1.2 Monitoring Oil Production

In Chapter 3, I use the uniform and patchy fluid distribution models along with results from reservoir simulation to study the feasibility of monitoring primary oil production. I begin with flow simulation from an oil zone that lies between a water zone and a gas cap. The simulation output included the spatial and temporal distributions of pore pressure and three phase fluid saturation. I used the results of laboratory measurements on core samples from the reservoir to model the dry frame elastic moduli, and I applied both uniform and patchy models to compute velocities in the reservoir. The uniform and patchy models provide the range of seismic response to a localized depression of the oil-gas contact (i.e. gas coning) associated with oil withdrawal. Through zero-offset synthetic seismic modeling, I show that for small changes in gas saturation (from S_g =0), changes in seismic response with patchy fluids are masked by noise. However, for uniform fluids, the changes in the seismic response are evident, even for small increases in S_g. Where S_g increases from 0 to 0.4 or more, the seismic response should change enough to detect the movement of the fluid contact with either fluid distribution model. I also estimate the effect of seismic resolution by laterally smoothing the velocity and density at each point in the reservoir before modeling the seismic response. Increasing the lateral resolution resulted in a wider seismic anomaly with a lower amplitude.

6.1.3 Frame Stiffness, Pore Fluid, and Pore Pressure Effects

In Chapter 4, I consider separately how the stiffness of the rock frame, pore fluids, and pore pressure affect the seismic response of sandstones. To demonstrate the effect of rock frame stiffness, I took the reservoir simulation results used in Chapter 3, and I modeled the velocities and seismic response for 3 high porosity sandstones with different elastic

moduli. The stiffest rock frame was approximately twice as stiff in bulk and shear modulus as the weakest rock frame. I showed that increasing stiffness reduces the seismic response to a gas cone developing over a thin oil zone. Here I used only the uniform fluid model to compute the reservoir velocities.

To illustrate the effects of pore fluid, I selected a Gulf Coast sand bounded by shale. I inverted the velocity logs using the uniform fluid model to get the dry frame properties of the gas sand. I then used the uniform fluid model to calculate the velocity for the sand saturated with 100% brine and mixtures of 20% brine with 80% gas-free oil, 80% live oil, and 80% gas. I also used the uniform and patchy fluid models to compare the seismic response for the sand with 80% gas and 65% gas (with brine as the other pore fluid). I computed the reflection coefficient as a function of incident angle at the top of the sand for each case using the Shuey (1985) approximation, and I generated synthetic CDP gathers. The brine saturated rock had the highest velocity and the smallest (in absolute value) reflection coefficient, and the polarity of the reflection changed from negative to positive at far offsets. All other fluids had negative reflection coefficients that became increasingly negative at far offsets. The cases of 80% and 65% gas with uniform distribution of gas and brine were indistinguishable. An interesting result here was that the sand with patchy mixture of 65% gas and 35% brine had velocities and reflectivities similar to the same sand with 80% live oil and 20% brine. The seismic signatures seen in the synthetic CDP gathers were also very similar.

I used the same Gulf Coast sand to illustrate the effect of pore pressure on the seismic response. I assumed that the sand was initially over pressured, and I used laboratory measurements of velocity versus confining pressure for Ottawa sand to model the change in elastic moduli of the sand with a decrease in pore pressure. I then generate synthetic CDP gathers for both cases, and I show that the pore pressure drop results in diminished seismic amplitudes and in velocity pull-up at the base of the gas sand. This demonstrates that repeated seismic surveys could be used to monitor pore pressure changes in poorly-cemented sands.

The effects of pore pressure must be considered for other types or rock as well. Results presented by Wang et al. (1996) indicate that changes in pore pressure can be seen in carbonates with cross-well seismic surveys. In this case, CO_2 injection into a carbonate oil

reservoir increased the pore pressure and resulted in decreases in V_P and V_S that exceeded expected changes based on fluid substitution alone. The authors simulated the CO_2 flood both at constant effective pressure and at pre- and post-flood in-situ conditions. Laboratory measurements of V_P and V_S at the two effective pressures verified the sensitivity of the carbonate to changes in pore pressure and to fluid substitution.

The main purpose of this chapter was to demonstrate how rock and fluid properties both impact feasibility of monitoring hydrocarbon recovery using repeated seismic surveys. I have shown how knowledge of the rock frame stiffness and its response to pressure changes are essential to interpreting or modeling the seismic response to fluid and pressure changes. Along with this, I have shown that fluid distribution should also be considered.

6.1.4 Patchy Saturation from Well Logs

Identification of patchy saturation on velocity logs is perhaps the first step to demonstrating the applicability of the patchy model at seismic frequencies. Results from Chapter 5 are promising in this regard. In this chapter, I present a study to identify patchy saturation from the analysis of logs from a Gulf Coast well. Using both uniform fluid and patchy fluid inversion techniques, I show that patchy saturation is likely to occur in this well. The basis for this claim is that the dry frame Poisson's ratio for an unconsolidated sand rarely exceeds a value of 0.2 in laboratory experiments (Spencer et al., 1994). Where the uniform fluid inversion yielded values greater than 0.25 and the patchy inversion yielded values that were in the expected range (e.g. 0.1-0.2), the patchy inversion was assumed to be correct.

This technique seemed to work for the well used in this study. It should be tested on other logs to see if it works for other wells. The need for using a model other than the uniform fluid model for mixing fluids in the pore space of a rock has been documented by other authors. One study in particular by Brie et al. (1995) reported the need for an empirical law for mixing pore fluids in order to match log data. They did not consider a patchy model, but their data could be explained by considering a patchy mixture of gas and brine. As reported in Chapter 5, the minimum patch size at sonic log frequencies can easily be 5 cm or less.

6.2 Data Needs for Monitoring

This thesis has demonstrated how to apply several rock physics principles to reservoir monitoring problems. The basic rock physics needs for recovery monitoring include the pressure dependence of dry rock moduli. Dry rock moduli at reservoir conditions can be obtained from inversion of sonic well logs, but the results from Chapter 5 and from Brie et al. (1995) indicate that the model used for inversion must be correct. However, even if the correct model for inversion is applied, no information about the pressure dependence of the moduli is obtained. This is where laboratory measurements on core samples are necessary. Figure 6.1 shows the normalized bulk and shear moduli of 3 samples as a function of effective pressure. These are from the data reported by Han (1986), and they span the range of pressure response exhibited by the sandstone samples. For example, the unconsolidated Ottawa sand ($\phi = 0.33$), designated by "A" in the plots, exhibits the largest pressure effect, with the bulk and shear moduli at 50 MPa effective pressure being 2.5 to 3 times the values at 5 MPa. The sample designated as "C" ($\phi = 0.057$, 6% clay) exhibits much less sensitivity to confining pressure, with the maximum change of 15% over the range of effective pressure. I chose one additional sample "B" ($\phi = 0.17$, 16% clay) to show a response between these two extremes in the Han data. The wide range of pressure responses exhibited by these samples illustrates the need to collect representative data from a reservoir being studied. The results by Wang et al. (1996) underscore the importance of understanding the pressure response of the reservoir rock when predicting or interpreting changes in a reservoir caused by recovery processes.

Also, temperature and pressure dependent fluid properties are needed. These properties are density, compressibility (inverse of the bulk modulus), and viscosity. Laboratory studies on the actual reservoir fluids would yield these properties. In the absence of such tests, we can use the relationships presented in Batzle and Wang (1992) to predict pore fluid properties at various temperature and pressure conditions. The needed inputs are brine salinity, oil API gravity, gas-oil ratio, and gas gravity (with respect to air). These inputs can then be used to compute the pore fluid properties at relevant temperature and pressure conditions.

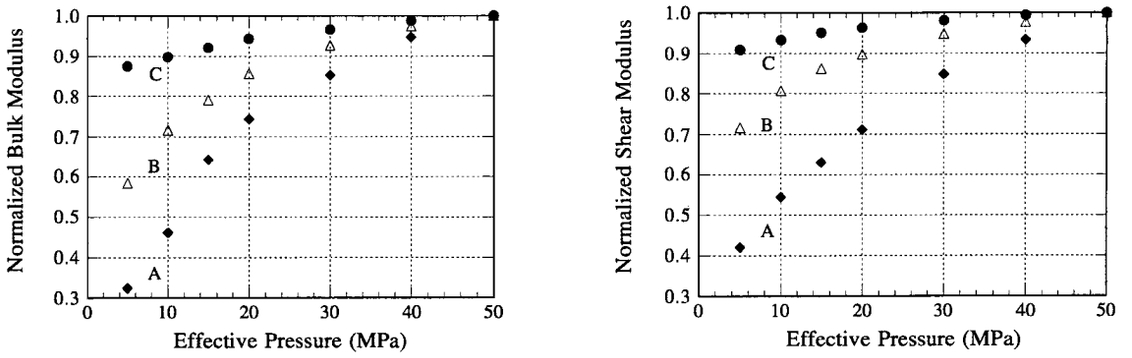

Figure 6.1: Normalized bulk modulus (left) and shear modulus (right) as a function of effective pressure for three rock samples (from Han, 1986). The rocks are: A) Ottawa sand with $\phi = 0.33$, B) sandstone with 16% clay and $\phi = 0.17$, C) quarry sandstone with 6% clay and $\phi = 0.057$.

6.3 Additional Considerations

One issue I have not investigated in this thesis is the role of attenuation in recovery monitoring. Laboratory measurements, like those presented by Toksöz et al. (1978), have established that pore fluids and effective pressure both affect attenuation of *P*- ans *S*-waves in rocks. The general conclusions are that attenuation is higher in brine-saturated rocks than in gas-saturated rocks, and attenuation decreases with increasing effective pressure for all cases of saturation.

There have been a few field case studies showing attenuation on cross-well and surface seismic data. For example, Eastwood et al. (1994) showed results from time lapse 3D surveys collected during cyclical steam injection, where steam is first injected into a well, then the injection stops, and the well is produced. During the production cycle, there was evidence of attenuation of high frequencies in the data below the reservoir zone, while the frequency content of the data above the reservoir was reproduced quite well.

In a cross-well seismic experiment, Harris et al. (1996) show how *P*-wave attenuation can be used to monitor injection of CO_2 in a carbonate. They observed a 25% decrease in the centroid frequency of direct *P*-waves passing through the CO_2 injection zone. *P*-wave attenuation increased from 15-20% in the injection zone.

These studies demonstrate that attenuation can play a role in interpretation time-lapse seismic surveys. Both showed measurable attenuation caused by enhanced oil recovery processes. Attenuation may be more sensitive to rock and fluid properties than velocity

according to Best et al. (1994). This may be important for interpreting seismic results that show little velocity change during the course of hydrocarbon production.

6.4 References

Batzle, M. and Wang, Z., 1992, Seismic properties of pore fluids: Geophysics, **57**, 1396–1408.

Best, A.I., McCann, C., and Sothcott, J., 1994, The relationships between velocities, attenuations, ande petrophysical properties of reservoir sedimentary rocks: Geophysical Prospecting, **42**, 151–178.

Brie, A., Pampuri, F., Marsala, A.F., and Meazza, O., 1995, Shear sonic interpretaion in gas-bearing sands: SPE Paper No. 30595, Proceedings - SPE Annual Technical Conference and Exhibition, Omega, **70**, 701–710.

Cadoret, T., Marion, D., and Zinszner, B., 1992, 1 kHz elastic wave velocities in partially saturated limestones; evidence of fluid distribution effect: SEG Annual Meeting Expanded Technical Program Abstracts with Biographies, **62**, 658–661.

Eastwood, J. Lebel, L. Dilay, A. and Blakeslee, S., 1994, Seismic monitoring of steam-based recovery of bitumen: The Leading Edge, **13**, 242-251.

Harris, J.M., Yin, F, and Quan, Y., 1996, Enhanced oil recovery monitoring using P-wave attenuation: SEG Annual Meeting Expanded Technical Program Abstracts with Biographies, **66**, 1882–1885.

Hill, R., 1963, Elastic properties of reinforced solids: Some theoretical principles: Journal of the Mechanics and Physics of Solids, **11**, 357–372.

Knight, R., and Nolen-Hoeksema, R., 1990, A laboratory study of the dependence of elastic wave velocities on pore scale fluid distribution: Geophisical Research Letters, **17**, 1529–1532.

Spencer, J.W., Cates, M.E., and Thompson, D.D., 1994, Frame moduli of unconsolidated sands and sandstones: Geophysics, **59**, 1352–1361.

Toksöz, M.N., Johnston, D.H., and Timur, A., 1979, Attenuation of seismic waves in dry and saturated rocks: I. laboratory measurements: Geophysics, **44**, 681–690.

Wang, Z., Cates, M.E., and Langan, R.T., 1996, Seismic monitoring of CO_2 flooding in a carbonate reservoir: rock physics study: SEG Annual Meeting Expanded Technical Program Abstracts with Biographies, **66**, 1886–1889.